Annual Report to

Development of Non-Contaminating Cryogenic Fracturing Technology for Shale and Tight Gas Reservoirs
Project Number: 10122-20

Aug. 20, 2013

PI: Dr. Yu-Shu Wu (ywu@mines.edu)

Completed by Yu-Shu Wu, Xiaolong Yin, Timothy Kneafsey, Jennifer Miskimins, Minsu Cha, Taylor Patterson, Bowen Yao, Naif Bandar Alqahtani

221 Marquez Hall, 1600 Arapahoe St.
Golden, CO 80401

Tel: 303-384-2093

http://petroleum.mines.edu/research/emg/

LEGAL NOTICE

This report was prepared by Yu-Shu Wu et al as an account of work sponsored by the Research Partnership to Secure Energy for America (RPSEA). Neither RPSEA, members of RPSEA, the National Energy Technology Laboratory, the U.S. Department of Energy, nor any person acting on behalf of any of these entities:

a. MAKES ANY WARRANTY OR REPRESENTATION, EXPRESS OR IMPLIED WITH RESPECT TO ACCURACY, COMPLETENESS, OR USEFULNESS OF THE INFORMATION CONTAINED IN THIS DOCUMENT, OR THAT THE USE OF ANY INFORMATION, APPARATUS, METHOD, OR PROCESS DISCLOSED IN THIS DOCUMENT MAY NOT INFRINGE PRIVATELY OWNED RIGHTS, OR

b. ASSUMES ANY LIABILITY WITH RESPECT TO THE USE OF, OR FOR ANY AND ALL DAMAGES RESULTING FROM THE USE OF, ANY INFORMATION, APPARATUS, METHOD, OR PROCESS DISCLOSED IN THIS DOCUMENT.

THIS IS A FINAL REPORT. THE DATA, CALCULATIONS, INFORMATION, CONCLUSIONS, AND/OR RECOMMENDATIONS REPORTED HEREIN ARE THE PROPERTY OF THE U.S. DEPARTMENT OF ENERGY.

REFERENCE TO TRADE NAMES OR SPECIFIC COMMERCIAL PRODUCTS, COMMODITIES, OR SERVICES IN THIS REPORT DOES NOT REPRESENT OR CONSTIITUTE AND ENDORSEMENT, RECOMMENDATION, OR FAVORING BY RPSEA OR ITS CONTRACTORS OF THE SPECIFIC COMMERCIAL PRODUCT, COMMODITY, OR SERVICE.

ABSTRACT

While hydraulic fracturing has revolutionized hydrocarbon production from unconventional resources, heavy dependence upon water presents shortcomings such as formation damage and public concerns over water usage and chemicals used in the fracturing fluids. Thus, waterless or reduced-water technologies have been actively sought after. Hydraulic fracturing stimulates hydrocarbon production by creating fractures that significantly increase the accessible contact area between the reservoir and the borehole. Fractures can also be created by sudden temperature change in materials, most often by subjecting a warmer material to a cold fluid, which creates thermal contraction of the surface and local tensile stress. Cracks form when the tensile stress exceeds the material's tensile strength. This mechanism has not been exploited in the context of stimulation, and may be used to weaken or fracture reservoir rocks to reduce or eliminate water usage.

We have developed experimental setups and procedures that are specifically designed to conduct cryogenic fracturing tests with and without confining stress, with integrated cryogen transport, measurements, and fracture characterization. A tri-axial loading system is built to simulate reservoir confining stress condition. The system uses two hydraulic cylinders and a press to apply stresses up to 6500 psi vertically and 4500 psi horizontally on 8"×8"×8" blocks. Borehole pressure, liquid nitrogen, and temperature can be monitored continuously. Acoustic signals are used to characterize fractures before and after the experiments.

The cryogenic stimulations conducted in our study were able to create cracks in the experimental blocks and deteriorate rock properties. We observed that fractures were created along a line of the strongest thermal gradient in a concrete block half-submerged in LN_2. Increasing the number of cryogenic stimulations enhances the level of fracture by both creating new cracks as well as widening the existing cracks. On the other hand, by comparing the cryogenic fracturing results from weak cement concrete and sandstone specimens, it is found that the generation of fractures is dependent on material properties. For the weak cement concrete specimen used in our cryogenic fracturing study, more cracks were created near the surface than internally. Experiments with transparent specimens provide insight regarding the expected fracture propagation when sufficient thermal contraction/stress is achieved. It allows for key observations in crack developments at the borehole geometry, such as exclusion distance, crack morphologies driven by both longitudinal and circumferential thermal contraction. It is found that water in the formation plays a competing role during cryogenic cooling with contraction of the rock, thus an unfavorable factor. A fast cooling rate is desired to achieve high thermal gradient and should be sought for by necessary means.

From the experimental study done by far, the foci of future studies are identified. We will observe whether fractures are created at reservoir stress levels by thermal shock, and how borehole pressurization improves fracturing. The effect of stress level and stress anisotropy on the characteristics of cryogenic fracturing will be investigated by taking advantage of our triaxial loading (TX) system. We will also need to investigate how various material properties affect cryogenic fracturing behavior. Full dimensional analysis will be performed considering all the relevant parameters, as a frame of understanding and a guide for designing field-scale study.

TABLE OF CONTENTS

LIST OF FIGURES

1. Literature Review on Cryogenic Fracturing

Cryogenic fracturing is a concept that looks to expand and improve on traditional hydraulic fracturing technology. The concept of cryogenic fracturing rests on the idea that a frigid liquid can induce fractures when brought into contact with a much warmer rock under downhole conditions. The cold liquid that effectuates such a fracture is known as the cryogenic fluid, or cryogen. When liquid nitrogen is injected into a rock whose temperature is drastically different, the heat from the rock will quickly transfer to the liquid nitrogen. This rapid heat transfer, better known as a thermal shock, will cause the surface of the rock to contract and fail in tension, thus inducing fractures orthogonal to the contact plane of the cryogen and rock. To further develop these newly induced fractures, liquid nitrogen has a liquid to gas expansion rate of 1:694 which creates a high pressure environment helping to propagate the fractures.

Just as hydraulic fracturing changed the resource development landscape, cryogenic fracturing offers much promise as a new technology in the petroleum industry's quest to improve both the pace and efficiency of resource recovery. This new technology could potentially increase the effects of fracturing while decreasing the cost of fracturing resulting in more formations becoming economically recoverable. Cryogenic fracturing has the potential to drastically increase our oil and gas reserves. In addition, the continued exploitation of hydrocarbon resources within the United States will promote American jobs and economic growth.

Traditional hydraulic fracturing in low permeability formations uses a highly pressurized fracturing fluid to create and prop open a complex network of fractures. These conductive fractures increase the permeability of the reservoir allowing for reservoir fluids to flow into the wellbore and be extracted. Hydraulic fracturing and the advancements associated with this technology have drastically changed the United States' producing abilities in the oil and gas industry. Without a doubt hydraulic fracturing has revolutionized the exploitation of hydrocarbons in the United States and has helped sparked an energy boom.

The modern hydraulic fracturing industry relies on water-based fluids, due to the general availability and low cost of water; however, a dependence upon water presents several major shortcomings. First, water can cause significant formation damage, which can occur as clay swelling and relative permeability effects stemming from capillary fluid retention (Mazza 1997). Formation damage mechanisms inhibit hydrocarbon flow and thus impair production rates and recovery efficiency. Second, water use in large quantities may place significant stresses upon the local environments where fracturing activities occur. For example, diversion of water away from other uses, transportation of

water to well sites on road infrastructure that was not designed for high traffic volumes, or construction activities associated with pipeline development can all have great impacts on the surrounding community. Finally, the downhole injection of chemicals needed in water-based fracturing programs, including slickwater and gel-based fracturing treatments, can lead to a contentious political climate. In contrast to hydraulic fracturing, cryogenic fracturing offers potentially greater fracturing capabilities without the issues associated with water based fracturing fluids.

Although not much research into cryogenic fracturing has been conducted, some early work suggests promising results. King (1983) examined the use of gelled liquid carbon dioxide, instead of water, to stimulate tight gas sand formations. His primary motivation for finding an alternative to water as the fracturing fluid was to prevent formation damage. After performing the cryogenic fracturing, the carbon dioxide would evaporate and not cause swelling near the wellbore in water sensitive formations. He also lists other benefits of liquid carbon dioxide use, including that carbon dioxide's recovery rate does not depend on reservoir pressure thus cleanup proceeds at a faster pace, and carbon dioxide's high solubility in oil serves to lower oil viscosity and enhance oil production. Since the gelled carbon dioxide that King used was capable of carrying proppant due to its higher viscosity than pure cryogen, the fractures were able to stay open. Accordingly, all the wells for which he published results experienced increased production rates (King 1983). Unfortunately, post fracturing production data over a long period of time was not available so the data is inconclusive determining if the cryogenic fracturing increases production past a few days.

Although successful results were produced in King's research, his researched only included theory and fieldwork but did not include laboratory experiments. Without a control group to compare the results to it is impossible to determine if the increased well production data is from thermal stresses creating fractures or from fluid pressure creating the fractures.

In a separate cryogenic fracturing study, Grundmann et al. (1998) treated a Devonian shale well with cryogenic nitrogen and observed an initial production rate 8% higher than the rate in a nearby offset well that had undergone traditional fracturing with nitrogen gas. Unfortunately, subsequent production information was unavailable because the well had to be shut in for logistical reasons. Although the increased initial production rate in this research suggests the efficacy of cryogenic fracturing, there could be a number of reasons why an offset well in a shale formation might produce differentially including anisotropic stress conditions and heterogeneous reservoir conditions over short distances. And similar to King's research, nothing in the Grundmann et al. study points to cryogenic fracturing, as opposed to hydraulic fracturing, as the stimulation mechanism.

To further advance the study of cryogen fluids on hydrocarbon producing formations, McDaniel et al. (1997) conducted simple laboratory studies where coal samples were immersed in cryogenic nitrogen. The coal samples experienced significant shrinkage and fracturing into smaller cubicle units, with the creation of microfractures orthogonal to the surface exposed to the cold fluid. The researchers found that repeated exposure cycles to the cryogen caused the coal to break into smaller and smaller pieces, or become rubblized. After 3 cycles of exposing the coal to liquid nitrogen and allowing the coal to ambient temperatures again, the coal was reduced to grain size particles. If the creation of fractures due to thermal stresses can occur in coal bed formations, it has the potential to occur in other types of rock as well. McDaniel et al. also conducted field experiments with cryogenic nitrogen, and published before and after production rate data for five wells. The results were mixed: three wells showed increased production, one well showed equivalent production, and one well showed decreased production. From the three wells that showed an increase in production, two of them were long term increases in production (McDaniel et al. 1997).

The prior research therefore suggests some promising benefits are associated with cryogenic fracturing fluid, but does not identify the specific fracturing mechanisms at work in downhole conditions. There are also many obstacles to overcome in the field such as equipment rated for cryogenic temperatures and figuring out how to transport proppant in the cryogen to prop open the newly formed fractures. Cryogenic nitrogen and carbon dioxide lack significant viscosity (see e.g. Rudenko et al. 1968, Fenghour et al. 1998) and may therefore inadequately carry proppant if viscosity serves as the primary transport mechanism. Gupta et al. (1998) concluded that cryogenic carbon dioxide's low viscosity could not enable adequate proppant transport; however, it is possible to create a high Reynolds number by increasing the velocity of the fluid allowing for adequate transportation of the proppant. The accompanying turbulence permits good transport of the proppant, at least through the wellbore to the perforations, if not through the fracture as well (Gupta, 1988).

Some research has even shown that cryogenic fracturing may not rely as extensively upon proppant as does traditional hydraulic fracturing. The McDaniel et al. (1997) research, which demonstrated coal rubblization in laboratory experiments, suggests a self-propping mechanism. If rock undergoes sufficient breakage into small pieces at the fracture/rock interface, the formation's inability to close on this rubblized rock may enable the fracture to stay open against in-situ compressive stresses after cessation of treatment pressure.

If neither traditional proppants nor a self-propping mechanism can effectively keep the created fracture open, ultra-light weight proppants (ULWPs) may fill the gap. ULWPs are manufactured proppants that consists of a chemically hardened walnut hull core with multiple layers of epoxy resin coating acting as the outer shell (Kendrick et al. 1995). Kendrick's research observed improved post-stimulation production in Devonian Shale wells treated with hydraulic fracturing methods using nitrogen foam fluid and ULWPs. The research shows that the majority of the wells with the ULWPs performed as good if not better than wells with traditional proppant. If the low viscosity nitrogen foam could successfully transport ULWPs, cryogenic fluid may be able to do so as well.

Although cryogenic fracturing brings with it substantial technical challenges, we have made much progress in understanding its physical mechanisms. Preliminary results suggest potentially huge rewards in unlocking new oil and gas reserves. Further research is required to better understand what cryogenic fracturing has to offer and how we can integrate it into our current fracturing technology.

2. Numerical Simulation

2.1 Introduction

The objective of the numerical simulation is to develop a numerical simulating tool based on analytical or numerical approach to model the influence of the cryogenic fracturing process on the artificial fractures distribution of the stimulated rock. The fracturing mechanisms will be more clearly understood by developing and applying this tool. The results of the simulation can also be used as a guide to future field test design.

The simulating tool to be developed will be able to handle multiple types of rocks based on different rock properties, such as Young's Modulus, Poisson's Ratio, Biot number, thermal conductivity, etc. Furthermore, the simulating tool could be coupled into some simulators to simulate the multi-phase flow flowing through the stimulated medium to evaluate the result of the cryogenic fracturing treatment. The simulating tool will be used to evaluate the general effect and the distribution of the artificial fractures after the cryogenic fracturing procedures instead of the dimension and actual distribution of the artificial fractures.

2.2 Assumptions

In this simulation tool, the fracturing process is assumed due to stress change induced by temperature drop caused by applying liquid nitrogen and pressure increase by the evaporation of the liquid nitrogen and injection pressure. For heat transfer, only the heat conduction and convection is considered, which means the radiation term is neglected.

The small natural fractures which are not connected to the artificial fractures are neglected for they are not contributing to the fluid flow. And the huge natural fractures like faults are also neglected for the reason of scale. All the other part of the rock is assumed to be isotropic, though the properties of rock in different grid blocks may vary.

Since the stimulation process happens in a relatively short time, the flow of the fluids inside the reservoir is not considered.

2.3 Theoretical Analysis

The basic geometry of the simulated well is the same as the experiment scheme: the cryogenic fluid will flow through the bore hole and cool the surface of it. The surface heat flow is assumed to satisfy

$$\nabla \cdot (kT) = -h\left(T_{cryogen} - T_{rock}\right)$$

where k is the thermal conductivity of the rock, h the coefficient of heat transfer, $T_{cryogen}$ the temperature of the cryogenic fluid (i.e. liquid nitrogen) and T_{rock} the temperature of the reservoir rock, which is a function of time and distance from the surface of the bore hole.

The strain state is given by

$$\varepsilon_{xx} = \frac{1}{E_x}\sigma_{xx} - \frac{\nu_{xy}}{E_y}\sigma_{yy} - \frac{\nu_{xz}}{E_z}\sigma_{zz} + \alpha_x(T - T_i)$$

$$\varepsilon_{yy} = \frac{1}{E_y}\sigma_{yy} - \frac{\nu_{xy}}{E_y}\sigma_{xx} - \frac{\nu_{yz}}{E_z}\sigma_{zz} + \alpha_y(T - T_i)$$

$$\varepsilon_{zz} = \frac{1}{E_z}\sigma_{xx} - \frac{\nu_{yz}}{E_z}\sigma_{yy} - \frac{\nu_{xz}}{E_z}\sigma_{xx} + \alpha_z(T - T_i)$$

where $\left(E_x, E_y, E_z\right)$ are elastic moduli in the (x, y, z) direction, $\left(\nu_{xy}, \nu_{xz}, \nu_{yz}\right)$ the Poisson's ratios, and $\left(\alpha_x, \alpha_y, \alpha_z\right)$ the coefficient of thermal expansion.

And the transient thermally-induced stress σ_{xx} associated with the temperature distribution T_{rock} is

$$\sigma_{xx} = -\bar{E}\bar{\alpha}\left(T - T_i\right) + \frac{\bar{E}\bar{\alpha}}{D}\int\left(T - T_i\right)dx$$

where $\bar{E} = \frac{1}{E_x} - \frac{\nu_{xy}^2}{E_y}$ and $\bar{\alpha} = a_x + \nu_{xy}\alpha_y$. The stresses in other directions have the same expression respectively.

The more generalized form of the Strain-Stress relation for rock considering temperature change is

$$\sigma_h - Bi \times p_{pore} = \frac{\upsilon}{1-\upsilon}\left(\sigma_v - Bi \times p_{pore}\right) + \frac{E}{1-\upsilon^2}\left(\varepsilon_h + \nu\varepsilon_H\right) + \frac{E}{1-\upsilon}\left(\alpha\left(T - T_0\right)\right)$$

where σ_h, σ_H and σ_v are the minimum, maximum horizontal and vertical stresses, ε_h, ε_H and ε_v the strains in the minimum, maximum horizontal and vertical directions, Bi Biot number of the rock, α linear thermal expansion, υ Poisson's ratio, and p_{pore} pore pressure.

For temperature distribution, the system is governed by

$$\nabla^2 T = \frac{1}{\kappa_r}\frac{\partial T}{\partial t}$$

where κ_r is the thermal diffusivity of the rock in radial direction, t the time.

The maximum surface stress in cold shock by cryogenic fluid is adequately described by the relation

$$\bar{\sigma}_{\max} = \left\{1.5 + \frac{3.25}{Bi} - 0.5e^{-16/Bi}\right\}^{-1}$$

With these equations, the simulation of the fractures can be done by comparing the total stress with thermal shock induced stress and the failing criteria of the rock. Once the total stress reaches the critical value of the breaking point according to the failing criteria, the rock can be treated as fractured. This process can be done both in analytical and numerical approaches. The aperture of fractures is related with the magnitude of the total stress and can be calibrated with experiment data.

2.4 Reservoir Fracture Model

Generally, the hybrid-fracture modeling approach, which combines the explicit-fracture method (discrete fracture model), multiple-interacting continua method (MINC) and single-porosity model, is preferred for this simulating tool. The explicit-fracture method can handle the artificial fractures more accurately. The modeling of artificial fractures is the focus of the simulating tool. The MINC method (Figure 2.1) can deal with the extensive natural fractures, if any, which may exist in the rock before the cryogenic treatment.

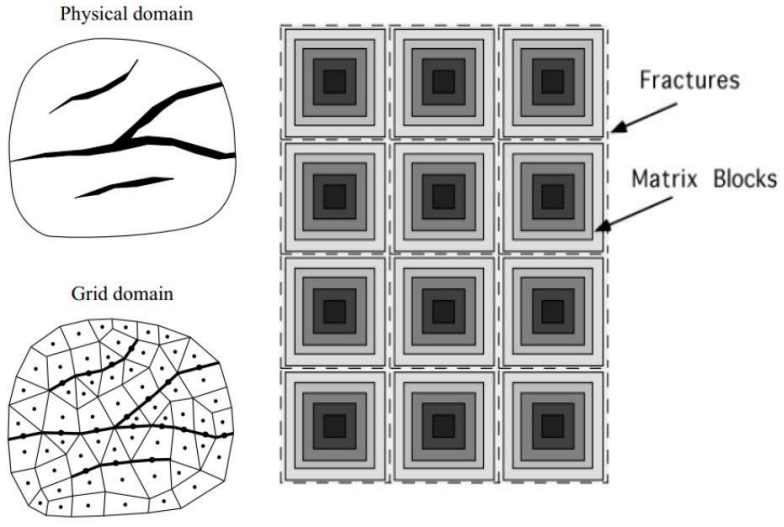

Figure 2.1 Conceptual Models of Explicit-Fracture Method (Left) and MINC (Right)

The distribution of artificial fractures will be obtained from the CT scan or other measurement of the cryogen treated rock sample. The stimulated reservoir volume (SRV) will be evaluated accordingly. Based on these data, a model of one fracturing stage can be built with modeling the artificial fracture with explicit-fracture method and the natural fractures around the artificial one with MINC. And single-porosity method is applied to the area outside the SRV, which is assumed to be isotropic or heterogeneous. This procedure can be used multiple times for multi-stage fracturing wells.

3. Equipment Design and Building

We consider two cryogenic stimulation plans: thermal shock and thermal shock combined by borehole pressurization. Fracturing by thermal shock depends on pure thermal gradient and resulting thermal tensile fracturing. In fracturing by thermal shock and pressurization, borehole pressurization may open up or propagate the fractures generated by thermal shock. A triaxial loading system is designed for loading the specimen to reservoir stress conditions.

3.1 Test Setup for Thermal Shock

In this test setup, we are mainly concerned about cooling the borehole as rapidly as possible to maximize thermal gradient. This is done by flowing LN_2 continuously through the borehole. The basic scheme is illustrated in Figure 3.1. In this lab-scale experiment, LN_2 is pumped from the Dewar by pressure difference using a liquid nitrogen withdrawal device. Liquid nitrogen is transported by a vacuum-jacketed hose to the specimen, and injected into the borehole and then directed to an outlet. A pressure transducer is attached to monitor the borehole pressure. In this thermal shock setup, pressure inside the borehole is basically the same as the pressure inside the Dewar. Because this scheme does not generate much pressure, the experiment can be applied to both confined and unconfined specimens. The experimental equipment employs cryogenic-rated transport, control, and measurement systems. We have set up real-time monitoring and logging of various parameters including pressure inside the borehole, LN_2 consumption, temperature, and acoustic signals. A structure that confines a packer in place is built to prevent leakage through the packer and sustain higher pressure in the borehole.

3.2 Test Setup for Thermal Shock Combined by Borehole Pressurization

This test plan is to enhance the fractures created by thermal shock by applying a level of pressure to the borehole during and/or after the thermal shock. One scheme of pressurization can be performed by letting existing LN_2 in the borehole to evaporate, while shutting off all of the inlet and outlet valves. Another scheme is by forcing pressure into a borehole by applying nitrogen gas (Figure 3.2). High borehole pressurization is possible for confined specimens loaded by the triaxial loading equipment. However, unconfined specimens cannot sustain much borehole pressure (rock splitting observed in weak concrete due to pressurization at pressure lower than ~100psi).

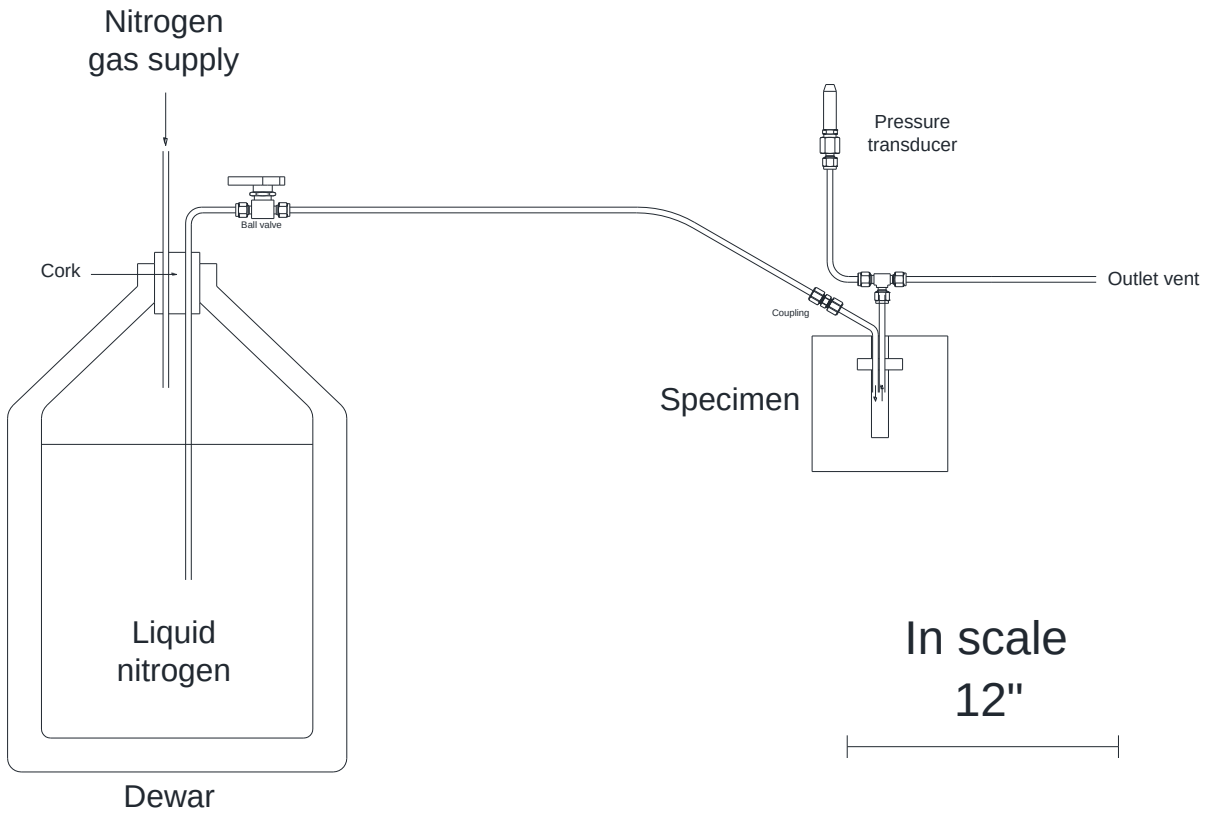

Figure 3.1 Overall schematic drawing for cryogenic thermal shock experiments without borehole pressurization.

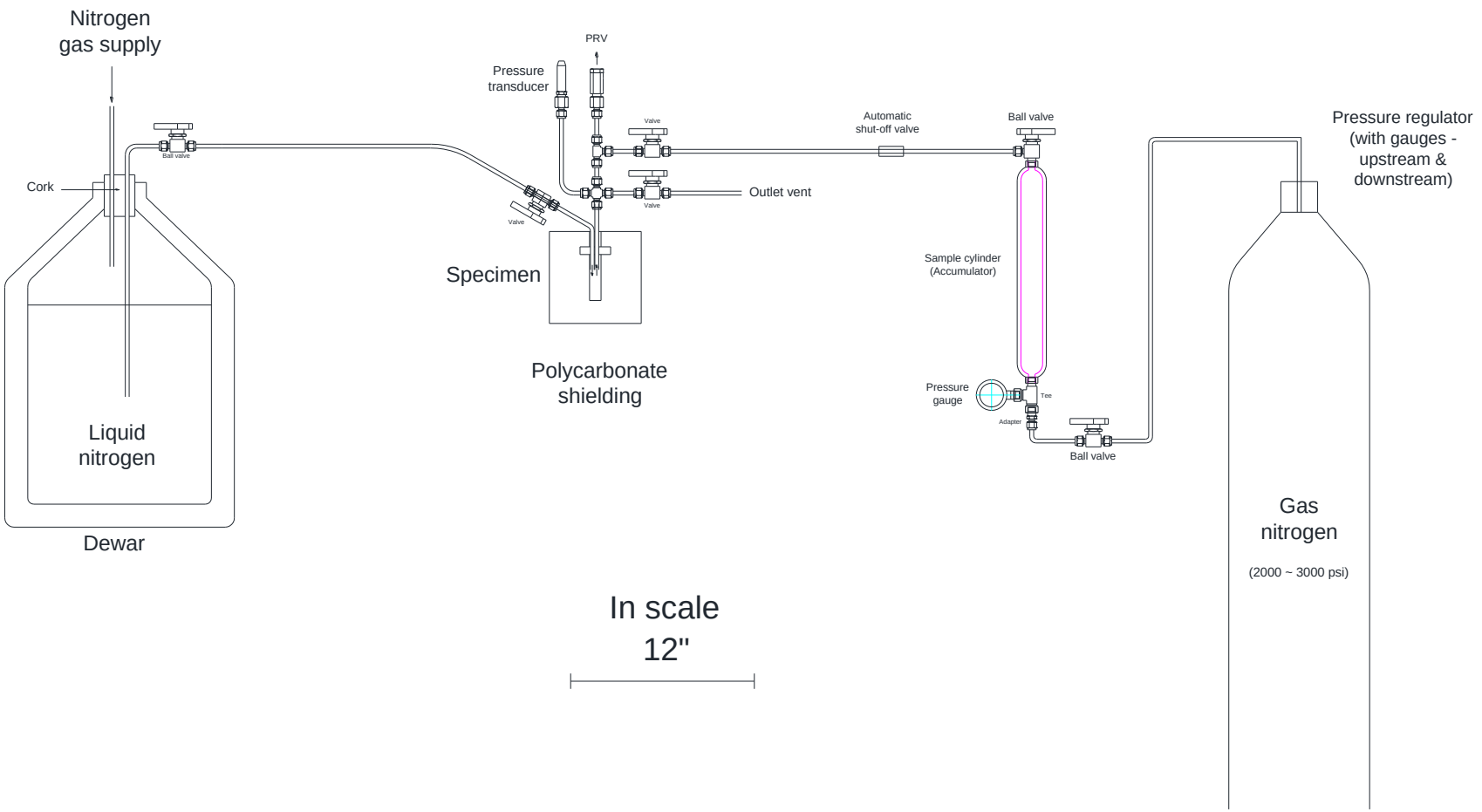

Figure 3.2 Overall schematic drawing for cryogenic stimulation experiments with borehole pressurization.

3.3 Triaxial Loading Equipment

A triaxial loading system is established to simulate reservoir confining stress conditions. The system operates two hydraulic cylinders and a press to load up to 6500 psi vertically and 4500 psi horizontally in 8”×8”×8” blocks, and is able to keep quasi-constant force using its hydraulic control system (Figure 3.3). We employ a hydraulic press whose loading column can travel horizontally, better known as a “roll-frame loader”. This feature makes the experimental work easier, because the heavy containment ring does not have to be moved.

Most other commercially available triaxial loading equipment use membrane packs that are connected to the hydraulic power system, and is a close system where the confining structure and loading pad, or piston, encloses the specimen. Our equipment is a straightforward open system where all three loading drivers and the specimen blocks are exposed and assembled inside the containment ring. This open system is versatile because it is easier to observe internal processes during the experiment and we can act immediately upon an accidental internal problem (e.g. cryogen spill). This also makes the system much more inexpensive than hydraulic power system contained by flexible membrane bladder. The simple, yet flexible design can also easily be converted for hydraulic fracturing experiments.

The only expected disadvantage of this system is that it is not ideal for specimens with uneven surfaces or tilted surfaces, although the pistons can accommodate small tilt. Uneven surfaces or significantly tilted surfaces will create uneven stress distribution. At high stress, this may fracture the rock. While we are trying to prepare even and untitled specimens as much as possible, the effect of uneven and/or tilted surfaces can be alleviated by inserting flexible rubber pads to evenly distribute stresses.

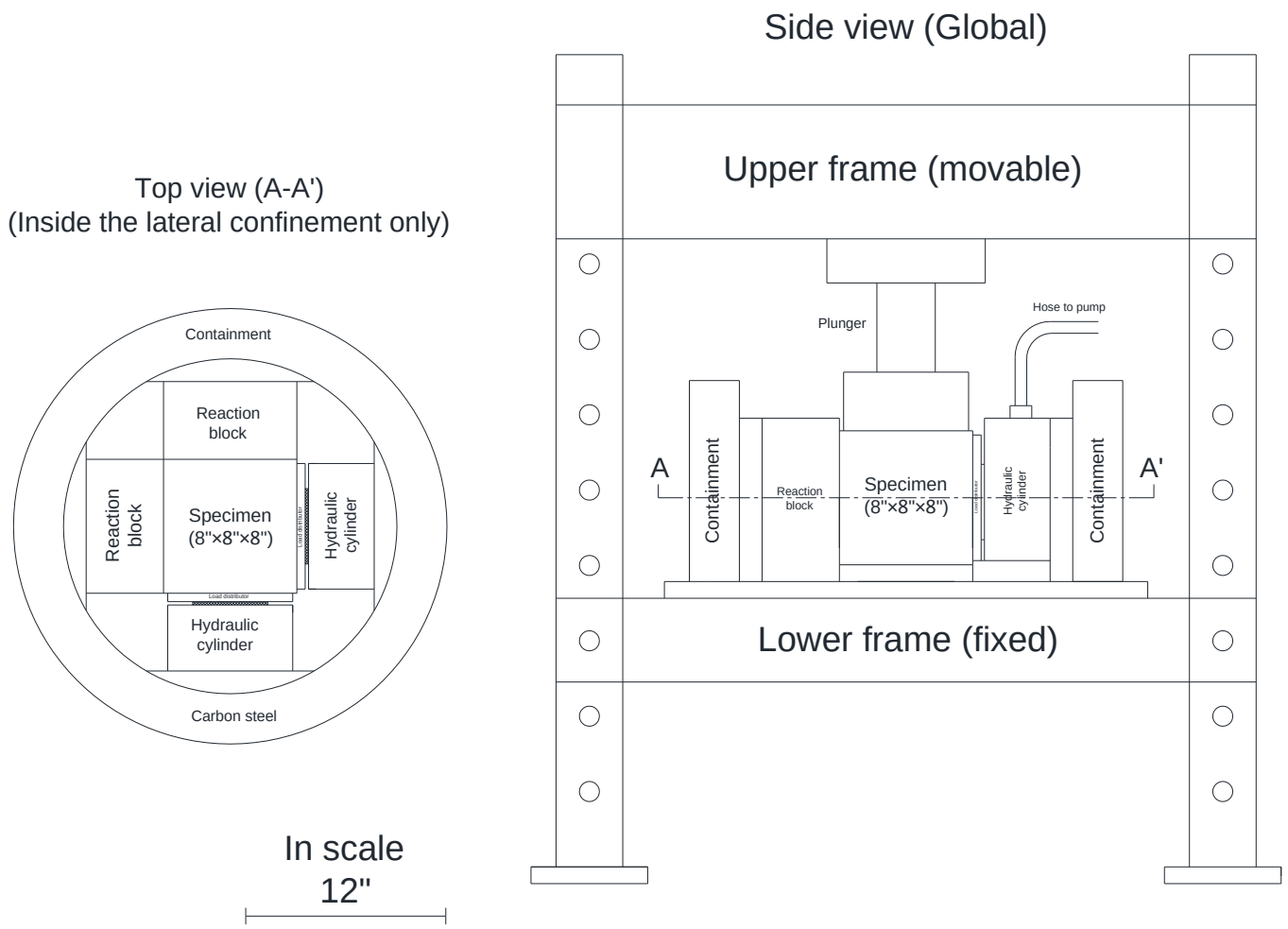

Figure 3.3 Triaxial loading system designed for cryogenic fracturing experiment.

3.4 Packer Placement

Packers are used to accommodate inlet and outlet tubings and seal the borehole from the outside. Keeping a packer in place is of important interest in our fracturing experiment. At low borehole pressure conditions in unconfined specimens, a packer-confining structure can be readily applicable (Figure 3.4). A packer can be attached to the top of a borehole with epoxy and then slight loading can be applied by the confining device. The degree of confining depends on the expected level of pressure inside the borehole. This device has been used for unconfined specimens and has been controllable and repeatable.

Placing a packer using wax was thought of as an alternative. An advantage of this plan is that the packer can be located inside the specimen, removing the need for an external rig like the confining structure (Figure 3.5). However, this plan needs practice and time to efficiently employ it. However, we may try it with the triaxial loading system where the existence of an external rig is undesirable due to loading drivers.

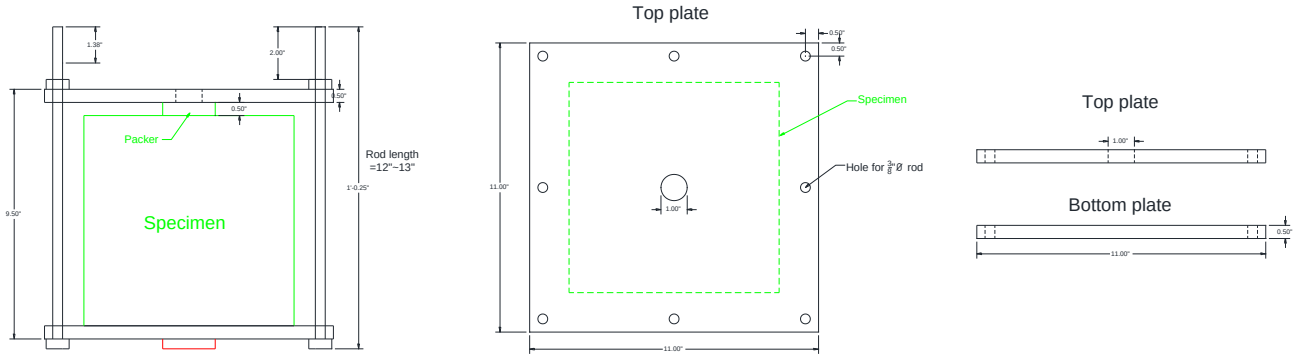

Figure 3.4 Packer installation by using a confining structure.

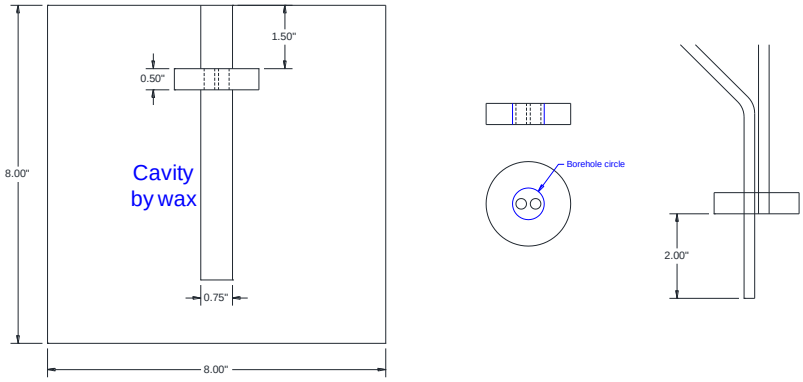

Figure 3.5 Packer installation and making cylindrical cavity by using wax.

4. Cryogenic Stimulation of Unconfined Specimen

4.1 Pouring LN_2 into Open Borehole of Concrete Cube

As a first-step experiment, a cement concrete specimen with 6"×6"×6" dimension are made and a borehole is drilled at the center of the top surface. Then liquid nitrogen is poured into the open borehole using a portable liquid nitrogen bottle. We observed rapid leidenfrost vaporization.

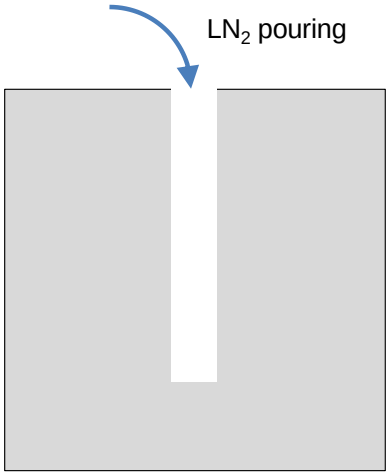

Figure 4.1 Schematic of pouring LN2 into the borehole of concrete block

The concrete block was imaged using X-ray computed tomography scanning (CT) after being tested by injection of liquid nitrogen in the well to look for fractures resulting from the cryogen application. Scanning was performed using a modified Siemens Somatom HiQ medical X-ray CT scanner. The block was scanned in two orientations to provide orthogonal views of the inside of the block. Figure 4.2 shows a vertical cross section of the block through the well in the center of the block. Fracture density would be expected to be highest near the well where temperature gradients would be highest. The CT scan shows density. The lighter shades indicate higher density and the darker shades indicate lower density. Fractures, if seen, would show up as darker features most likely emanating from the well. A number of features are visible in Figure 4.2 (and later in Figure 4.5 to a lesser extent). One is an "X"-shaped pattern across the block. This is an artifact of scanning a rectangular block. The second feature is a series of concentric circles in the upper third of the image. This is an artifact of non-uniform response of a series X-ray detector. The third feature is dark lines extending from the bottom of the well. These too

are X-ray scanning artifacts as they are not seen in the perpendicular scan. Numerous voids are visible (dark patches) from air entrained in the block formation process. No fractures are observed in the set of scans. This is consistent with visual observations as well.

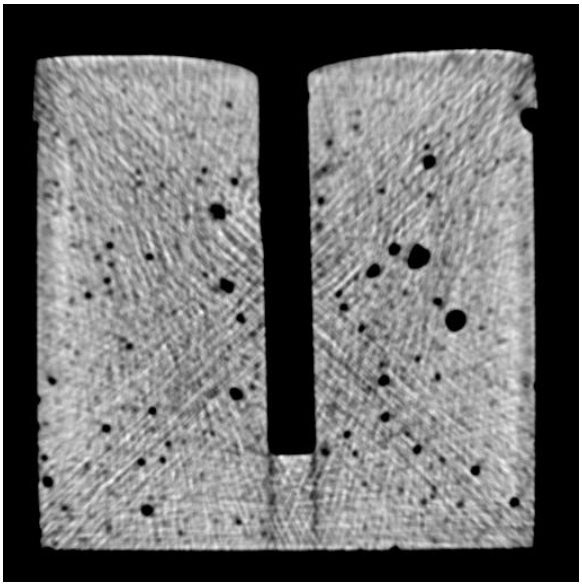

Figure 4.2 X-ray CT scan vertical cross section of the concrete block.

4.2 Semi-Submersion Experiment

To apply a strong constant temperature gradient across a concrete block, an 8 inch cubic concrete block was set on supports in an open-top insulating enclosure. The enclosure was filled with liquid nitrogen up to the midline of the concrete block. The liquid nitrogen level was maintained for 30 minutes and then allowed to boil off. The block was not removed until it equilibrated thermally with ambient temperature. Each side was labeled and photographed at high resolution before and after the test. The images were carefully aligned and digitally subtracted from one another to highlight the differences (Figure 4.4).

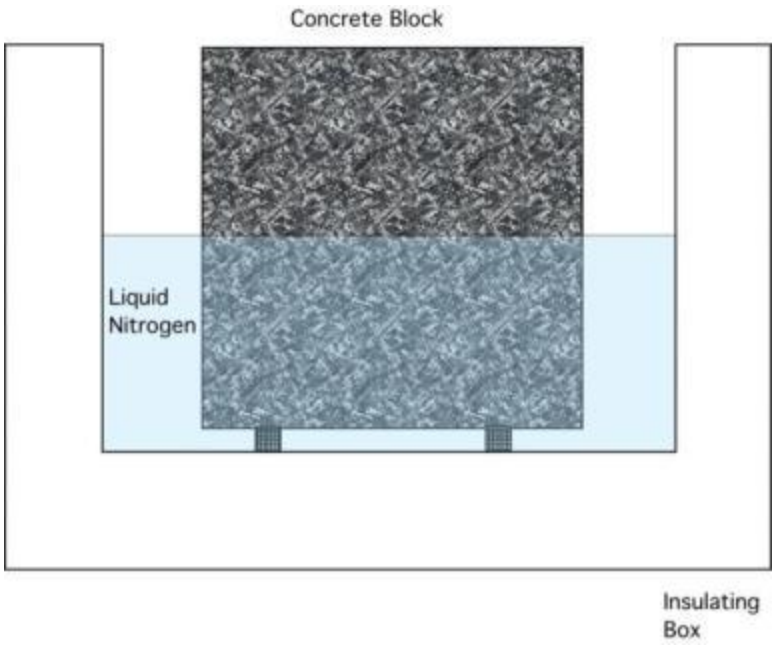

Figure 4.3 Setup for semi-submersion test.

Figure 4.4 shows the results of subtracting the before and after images (difference images). The differences for the top and bottom (shown at the top and bottom) do not show any fractures. The four vertical faces that were semi-submerged show a fracture along the center all the way around the block (light shaded crack). This indicates that the block was fractured due to the application of the thermal gradient. No obvious indication of block fracturing was observed during the 30+ minute test and no obvious cracking sound was heard.

Following the test, the block was CT scanned using a modified G.E. Lightspeed 16 medical CT scanner. Figure 4.5 shows a vertical cross section indicating the presence of a fracture (darker) emanating from both sides and progressing towards the center of the block.

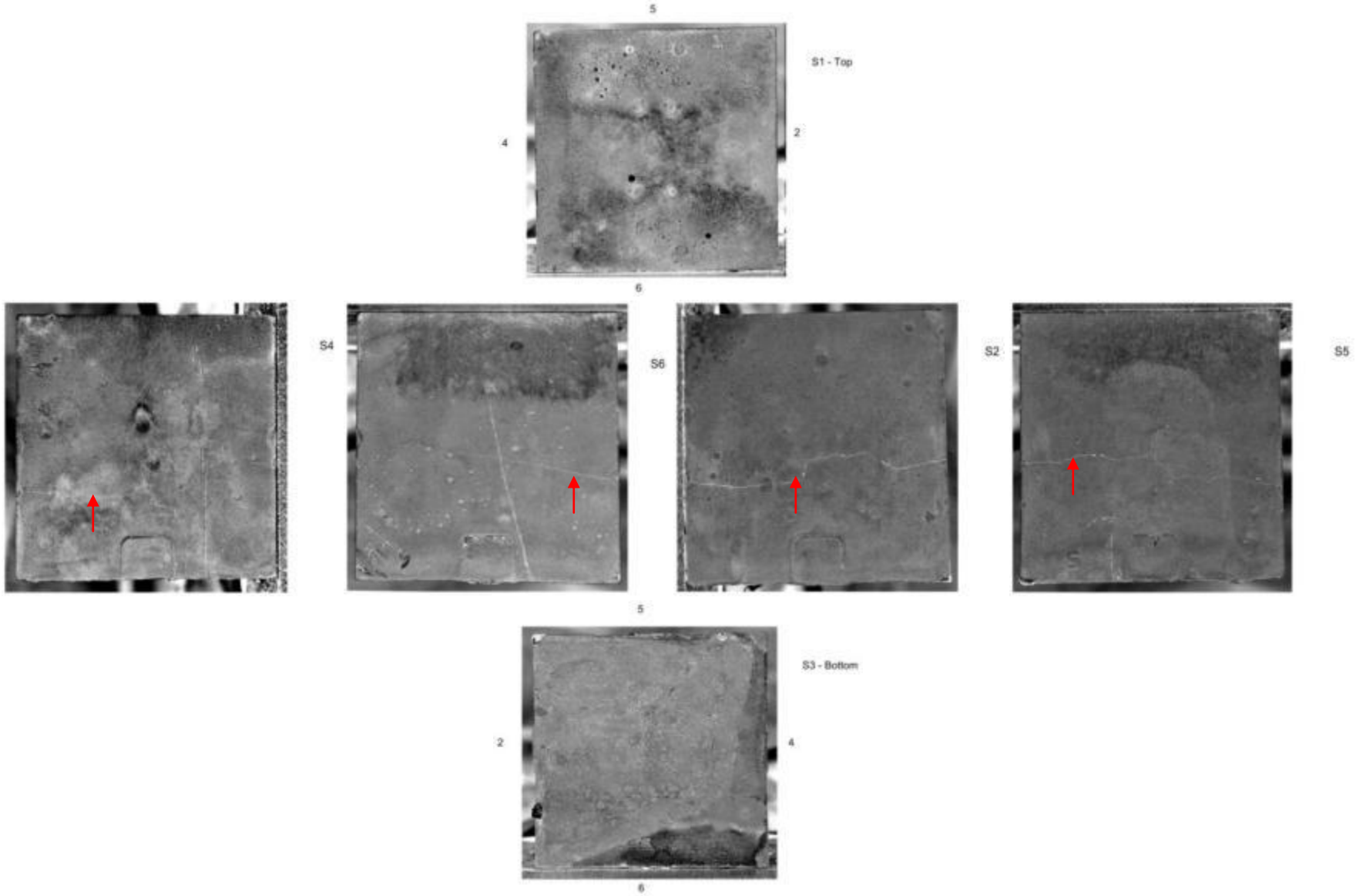

Figure 4.4 Subtracted before and after images of block sides in semi-submersion test. Side numbers are labeled S# where # is the side number. Top row – Top side; Middle row – vertical faces 4, 6, 2, and 5; Bottom row – Bottom side. On the top and bottom images, the location of each of the sides are shown. Note the light colored fracture along the midline of faces 4, 6, 2, and 5.

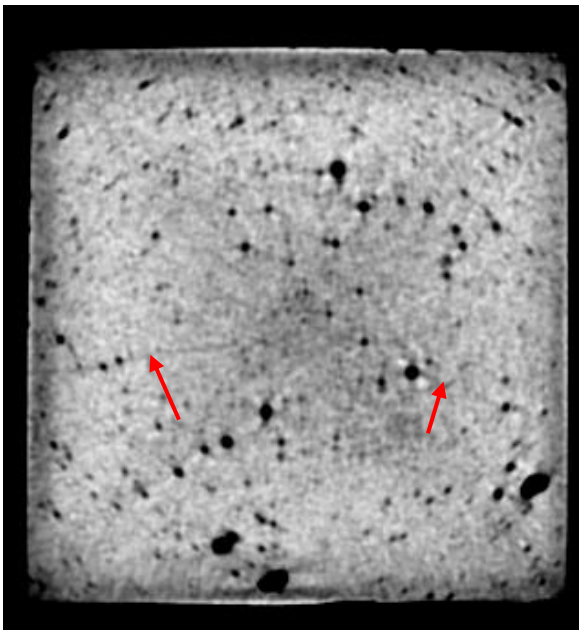

Figure 4.5 CT scan showing a vertical slice of the block from the semi-submersion test. Arrows point to fractures in the block resulting from cryogenic fracturing.

4.3 Thermal Shock on Unconfined Concrete Specimen

In this section, we present thermal shock experiments on a concrete specimen without forced pressurization of the borehole. The 100% cement concrete block was air-cured for 5 weeks after contained in the mold for 24 hours, resulting in relatively low strength (both compressive and tensile).

4.3.1 Testing with an Unconfined Packer

Figure 4.6 shows the experimental setup that was used for the thermal shock experiment on concrete by flowing liquid nitrogen in the borehole. A spray-type insulation is applied for heat insulation as well as packer sealing. The packer is loosely sitting on top of the borehole. Pressure about 5~10 psi was generated due to rapid vaporization of liquid nitrogen inside the borehole and along the transport lines. Thus leakage was observed at the packer/block interface and out of the insulation.

LN_2 is released from the Dewar tank and flows to the specimen borehole through the vacuum jacketed tube and insulated stainless steel tubes. The borehole is open to the air through a vent and warmed N_2 flows out to the atmosphere. Overall, there is no significant pressure buildup inside the borehole because N_2 flows freely into the atmosphere.

A set of S-wave acoustic sensors are mounted at a location on the Face 2 and 4 to monitor the wave signatures. An oscilloscope and a pulser are used to generate and record signals.

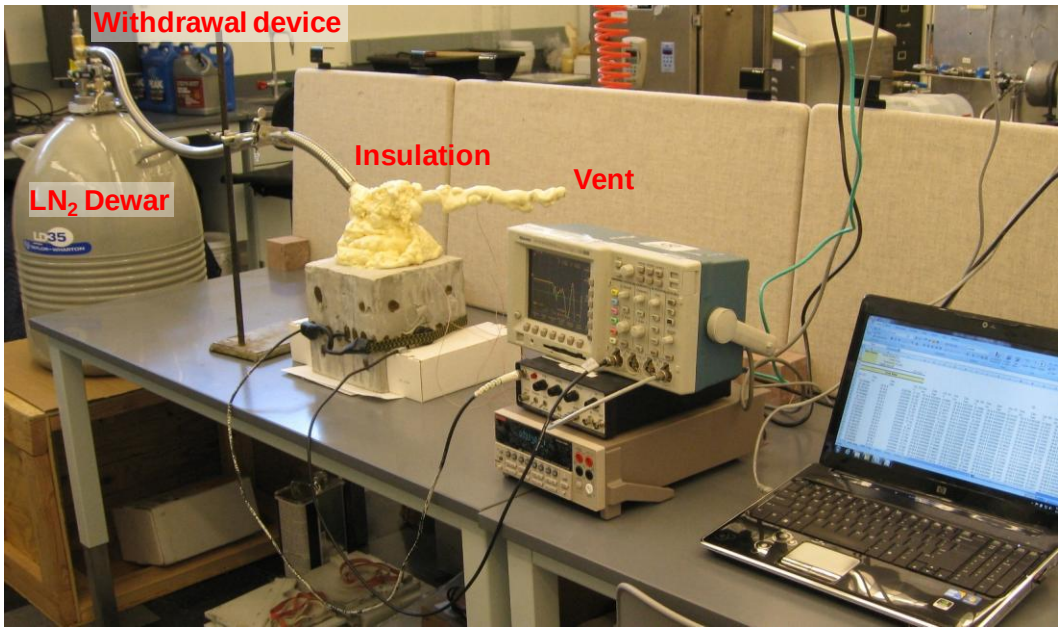

Figure 4.6 Experimental setup

Cracks

Before the thermal shock, no visible cracks near or inside the borehole existed. Several noticeable cracks are found near and inside the borehole after the thermal shock.

(a)

(b)

Figure 4.7 Cracks observed after the thermal shock (a) near the borehole and (b) at the borehole surface.

However, there were some pre-existing micro-cracks even before the thermal shock at the block surfaces due to the natural shrinkage of concrete (Figure 4.8). The dark spots are stains from the couplant used for securely attaching the ultrasonic sensors.

After the testing, not only are new cracks are generated, but the existing cracks have opened wider. Particularly, there were virtually no cracks at the bottom before applying cryogen. Some major cracks are generated after the cryogenic stimulation.

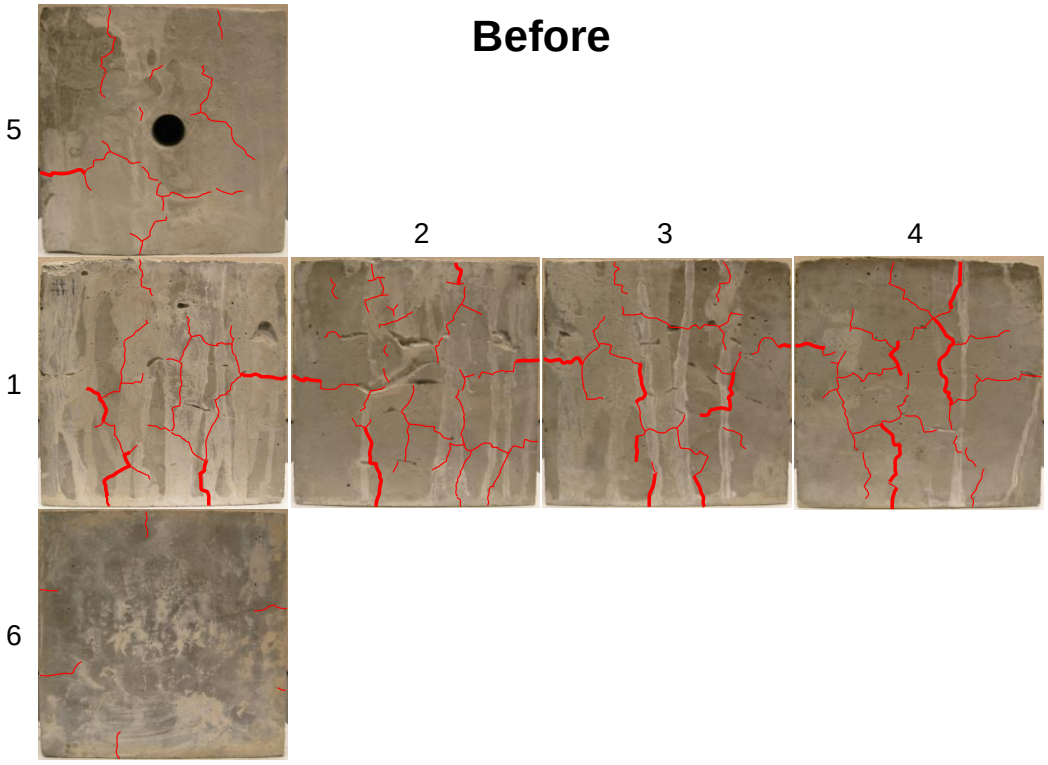

Figure 4.8 Pre-existing surface cracks – the superimposed lines are weighted according to the crack thickness.

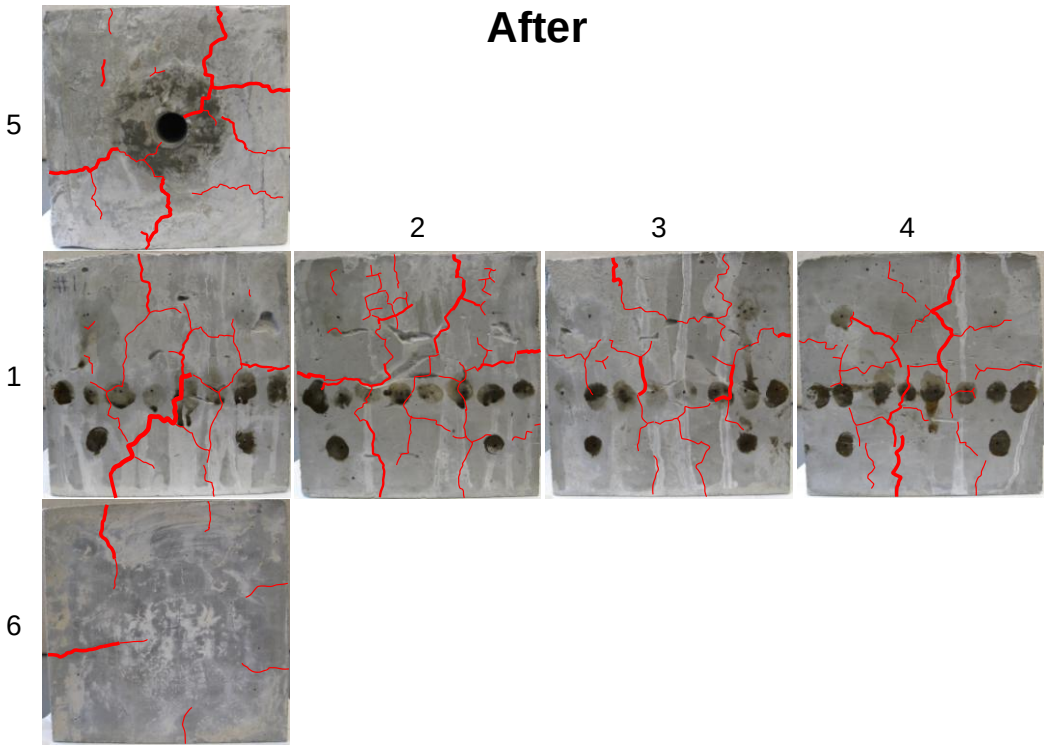

Figure 4.9 Surface cracks after the thermal shock. Note that the dark spots are stains from the couplant used for securely attaching the ultrasonic sensors.

Temperature

Thermocouples are used to measure temperatures at various locations in the experiment. Location 2 (black) is hung inside the borehole (Figure 4.10).

The spikes shown in the plots in Figure 4.11 are where the LN_2 is closed temporarily to reduce pressure inside the borehole, as the packer is not confined. LN_2 starts to leak from the packer toward the right surface at some point. This lowers the temperature at the right surface as shown in the plot.

Throughout the test, the temperature difference between inside the borehole and the block face is observed to be large.

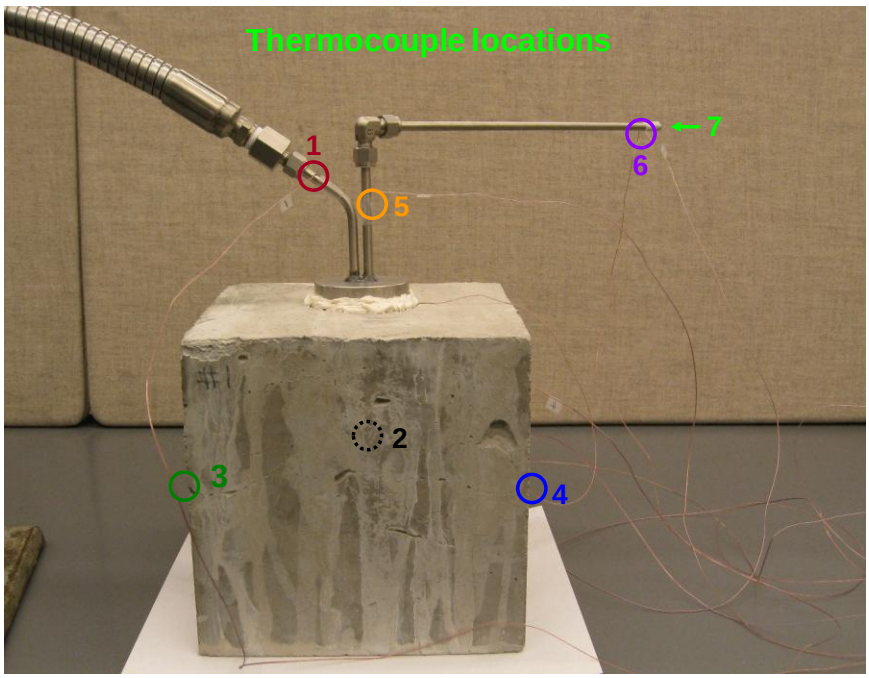

Figure 4.10 Locations of the thermocouples used in the temperature measurements

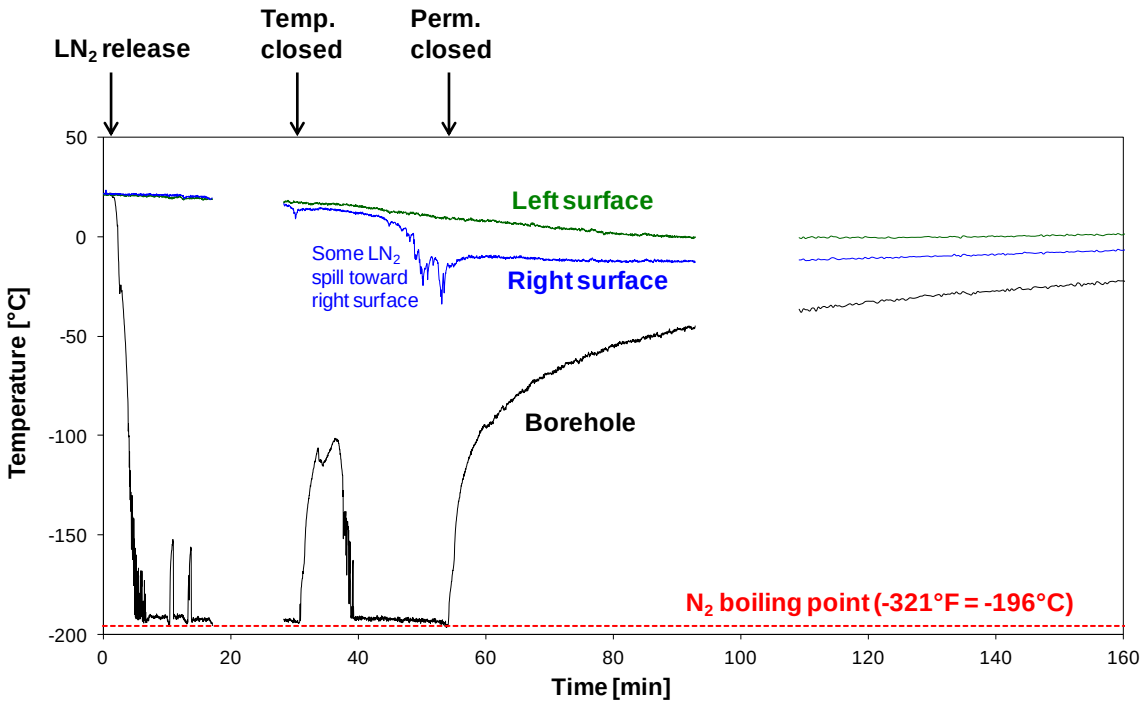

Figure 4.11 Temperature evolution during thermal shock experiment

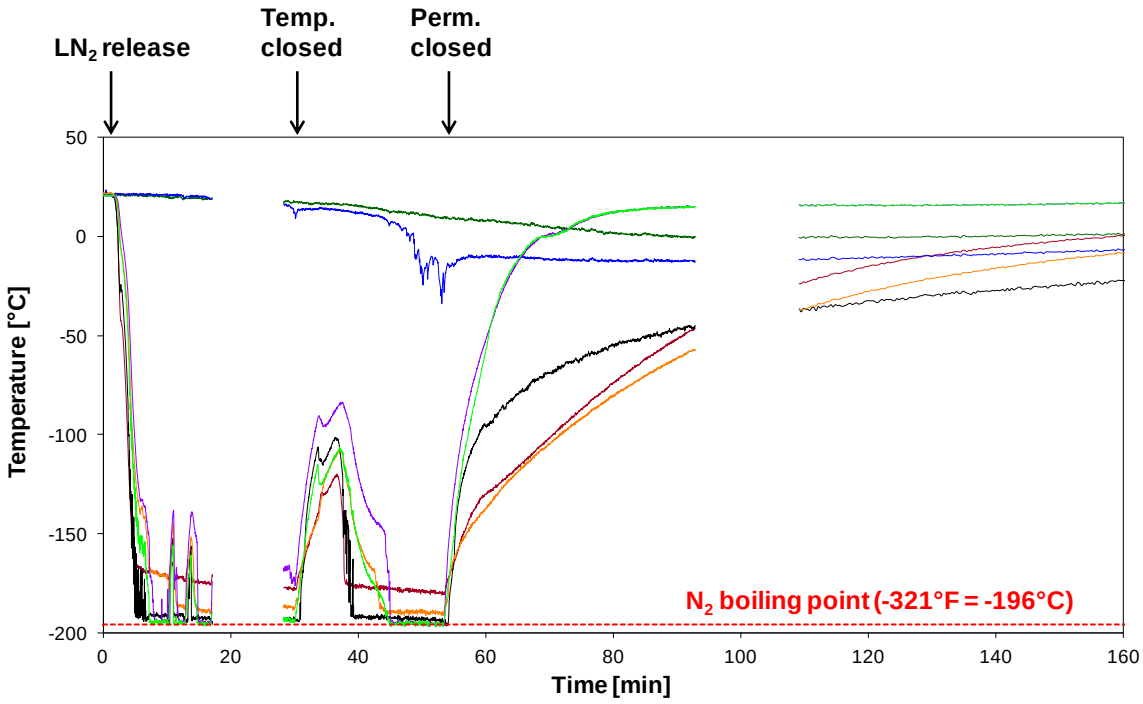

Figure 4.12 Temperature evolution during thermal shock experiment – with more locations

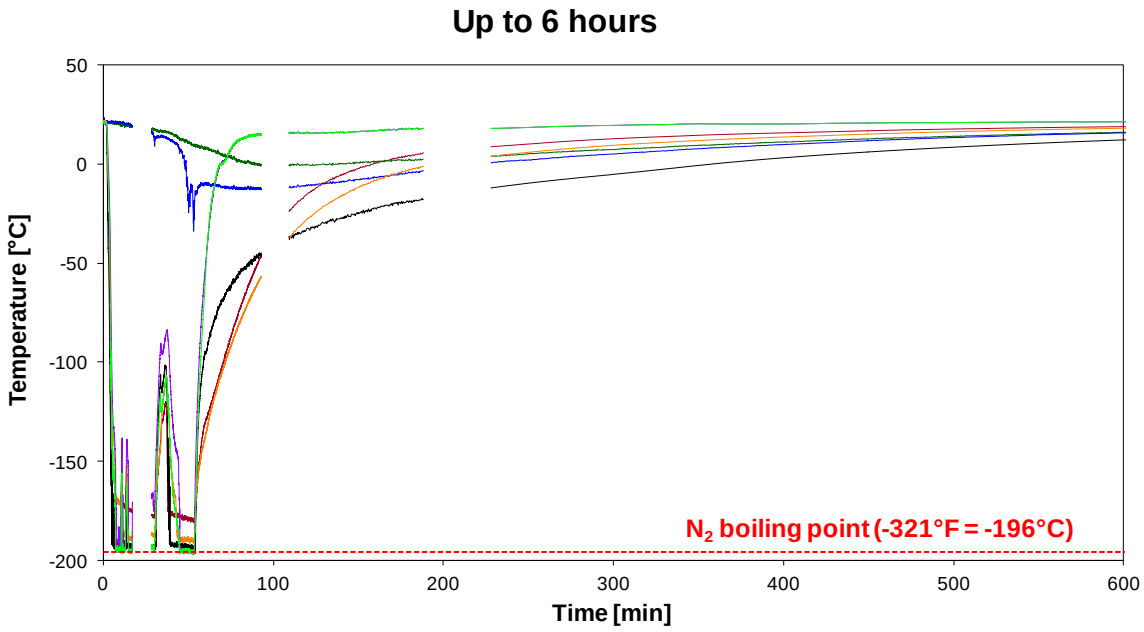

Figure 4.13 Temperature evolution after the thermal shock experiment (up to 6 hours)

Acoustic signatures

The characteristics of acoustic waves propagating through the medium depend on the mechanical properties of the medium. We would like to know the differences in the acoustic signatures before and after the cryogenic stimulation. Acoustic measurements are conducted before and after the test using S and P ultrasonic transducers. Acoustic waves are also monitored during the cryogenic stimulation; therefore, we mounted the S transducer acoustic sensors to the specimen surfaces during the testing.

Figure 4.14 shows the locations for the acoustic measurements before and after the cryogen stimulation. Acoustic signals are measured along Faces 1&3 and 2&4. For each face set, the acoustic measurements are conducted at 12 locations. We are mainly interested in P and S wave velocities and amplitudes.

In Figure 4.15, early arrival parts of elastic wave signals are presented with the normalized amplitude to compare changes in arrival time and waveforms. At most measurement locations, arrivals are delayed and waveforms have changed significantly. The characteristic of acoustic signatures approximately corresponds to the surface crack.

For example, the acoustic signals at location 12 is the least changed in terms of arrival time, and we also observed that the surface around location 12 is the least cracked due to the thermal shock.

In Figure 4.16, the signals still show early parts near the arrivals. However, the original amplitude is kept to compare changes in the amplitudes of the P and S waves. The amplitude measured at most locations for both P and S wave decreased significantly after the thermal shock (except for the location 12).

Finally, all signals are presented with their full range and original amplitude to compare global waveforms (Figure 4.16). It is observed that global amplitude is reduced and the global frequency of the signals became lower.

An analysis for the quantitative changes in velocity and frequency contents will be performed in the future.

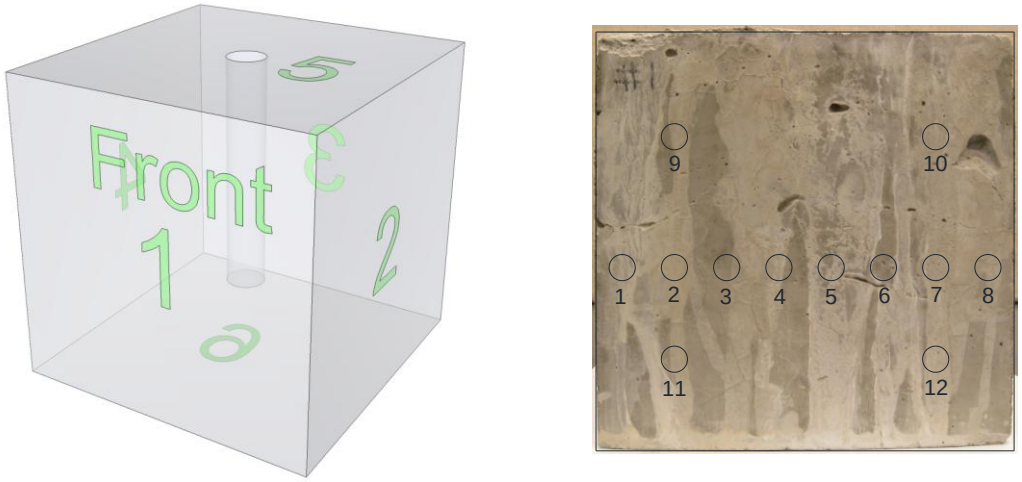

Figure 4.14 Acoustic measurement before and after thermal shock: measurement locations

(a)

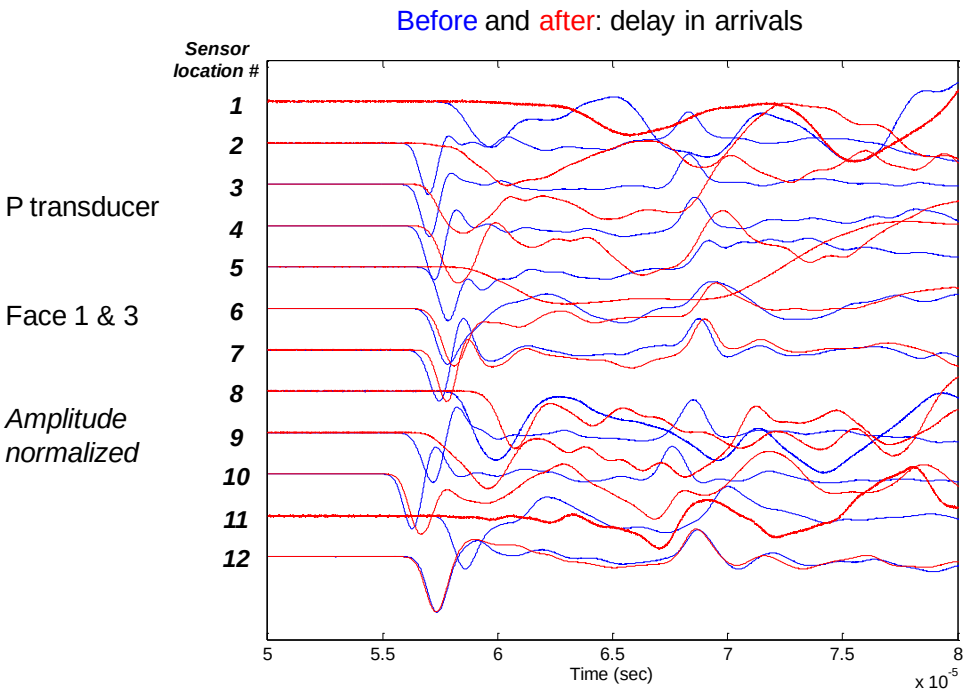
Before and after: delay in arrivals
Sensor location #
1
2
3
4
5
6
7
8
9
10
11
12
P transducer
Face 1 & 3
Amplitude normalized
5
5.5
6
6.5
7
7.5
8
Time (sec)
x 10-5

(b)

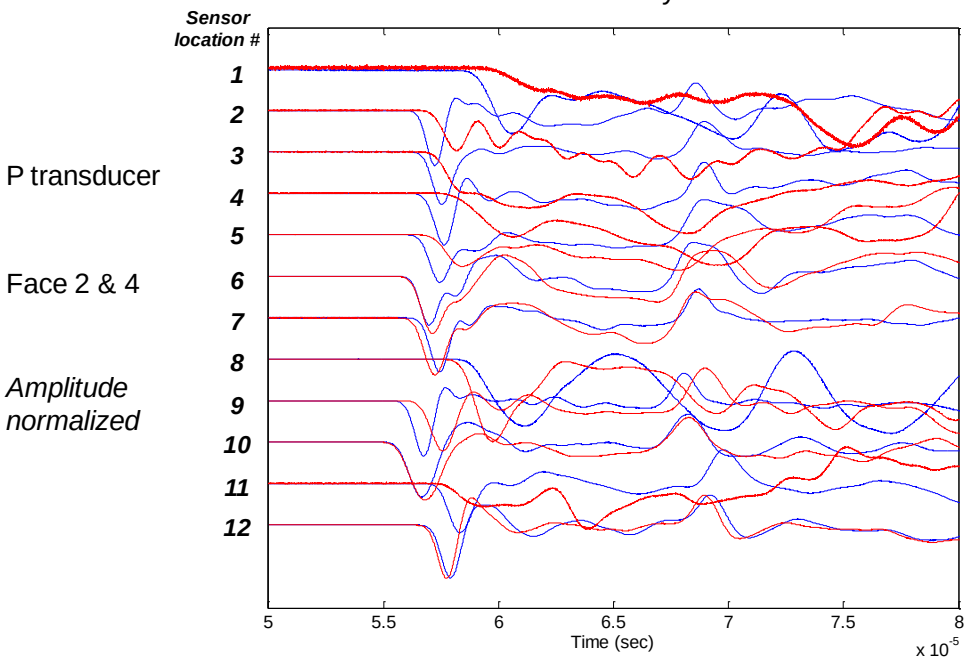
Before and after: delay in arrivals
Sensor location #
1
2
3
4
5
6
7
8
9
10
11
12
P transducer
Face 2 & 4
Amplitude normalized
5
5.5
6
6.5
7
7.5
8
Time (sec)
x 10-5

(c)

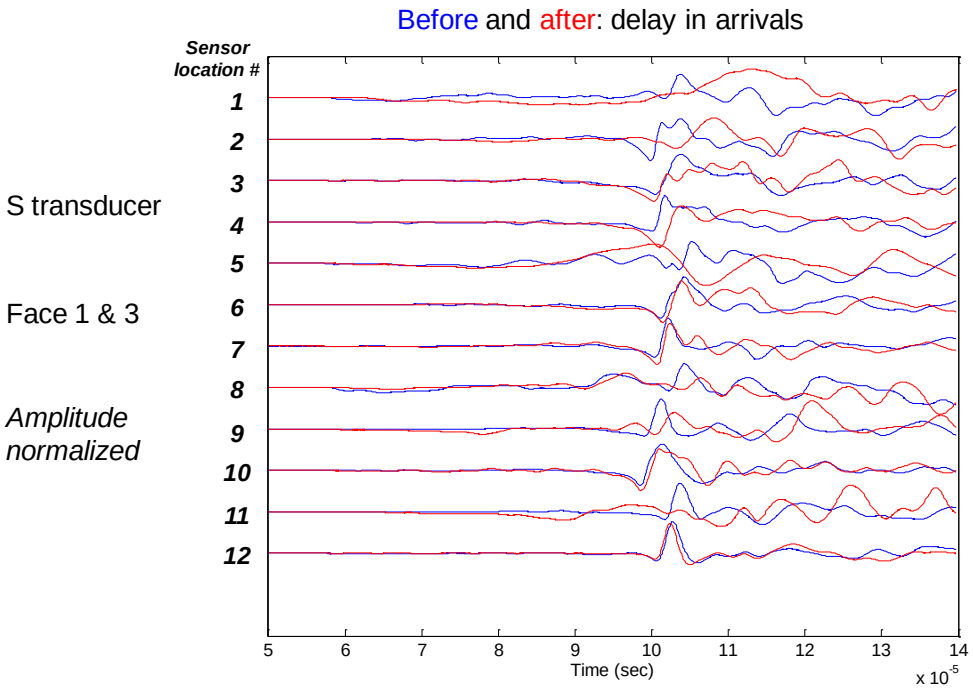

(d)

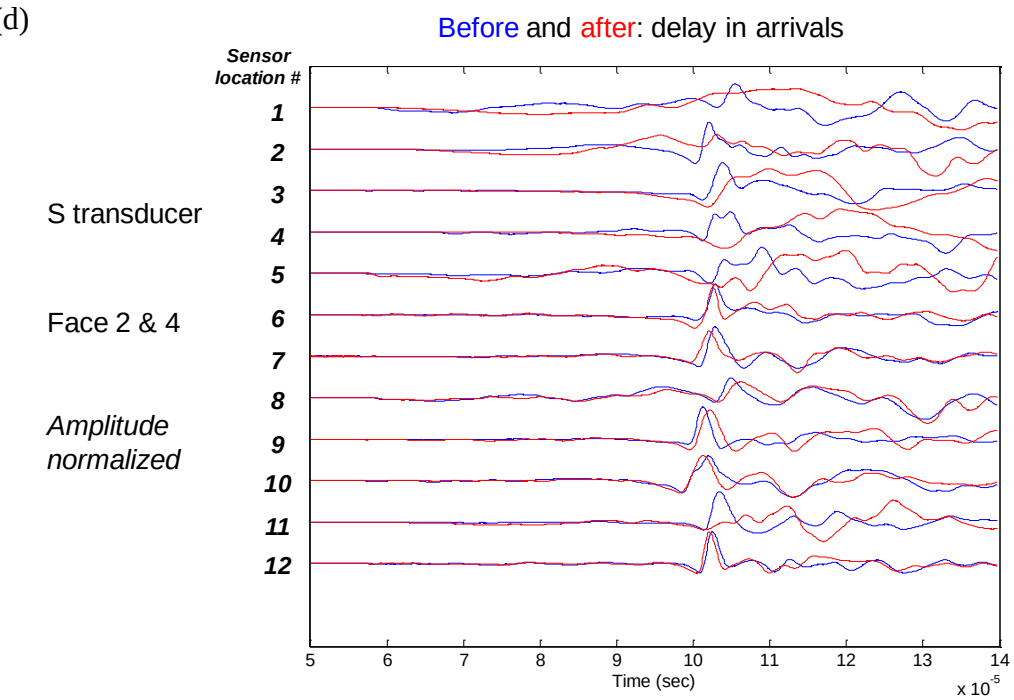

Figure 4.15 P and S wave arrivals before and after the thermal shock (compared with normalized amplitude).

(a)

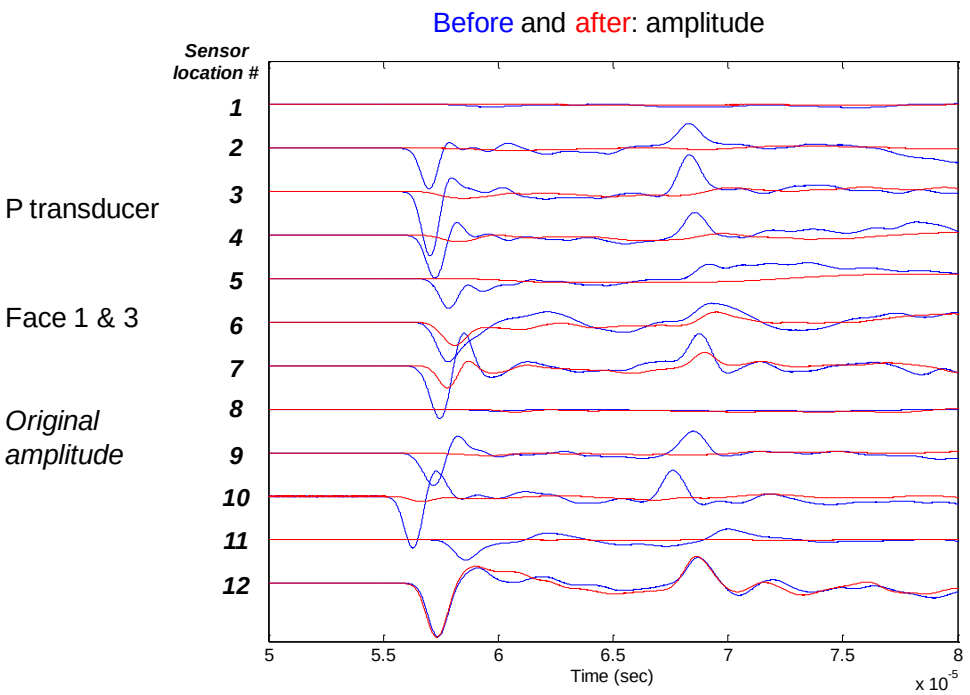
Before and after: amplitude
Sensor location #
1
2
3
4
5
6
7
8
9
10
11
12
P transducer
Face 1 & 3
Original amplitude
5
5.5
6
6.5
7
7.5
8
Time (sec)
x 10^-5

(b)

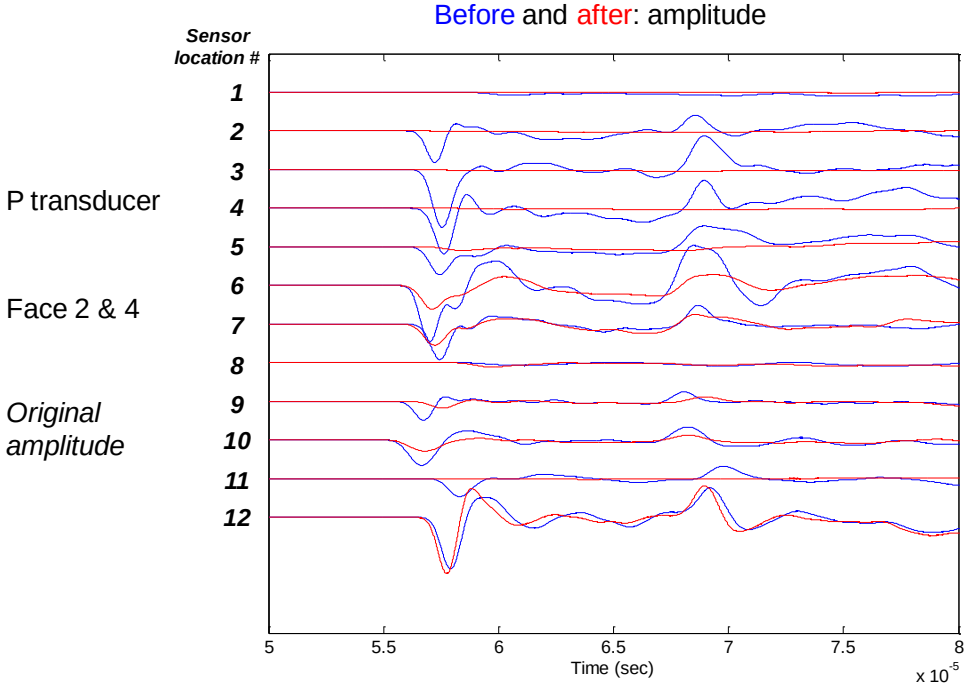
Before and after: amplitude
Sensor location #
1
2
3
4
5
6
7
8
9
10
11
12
P transducer
Face 2 & 4
Original amplitude
5
5.5
6
6.5
7
7.5
8
Time (sec)
x 10^-5

(c)

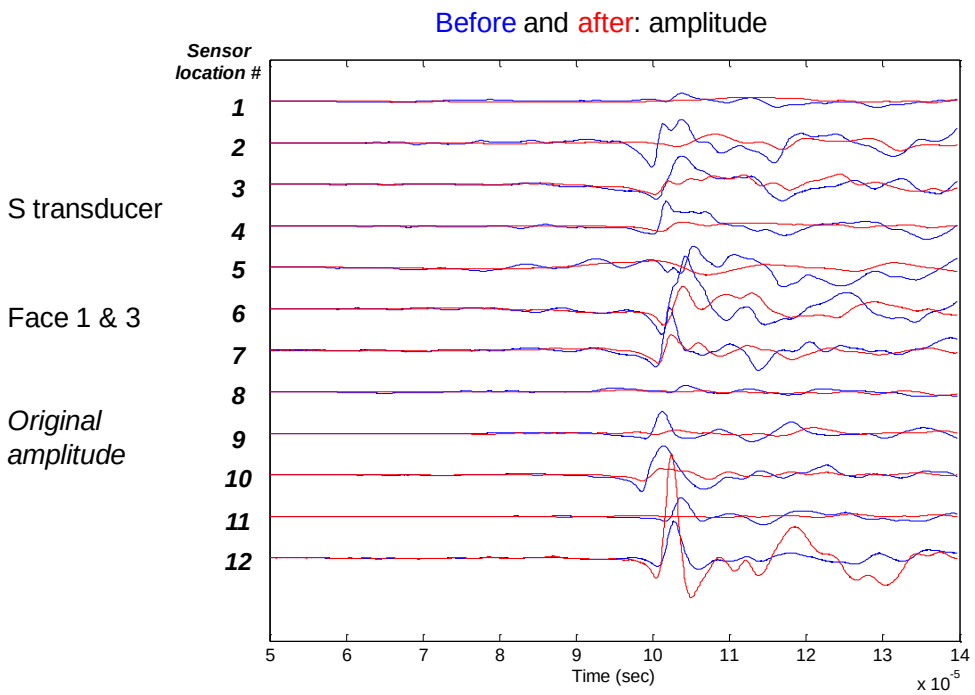

(d)

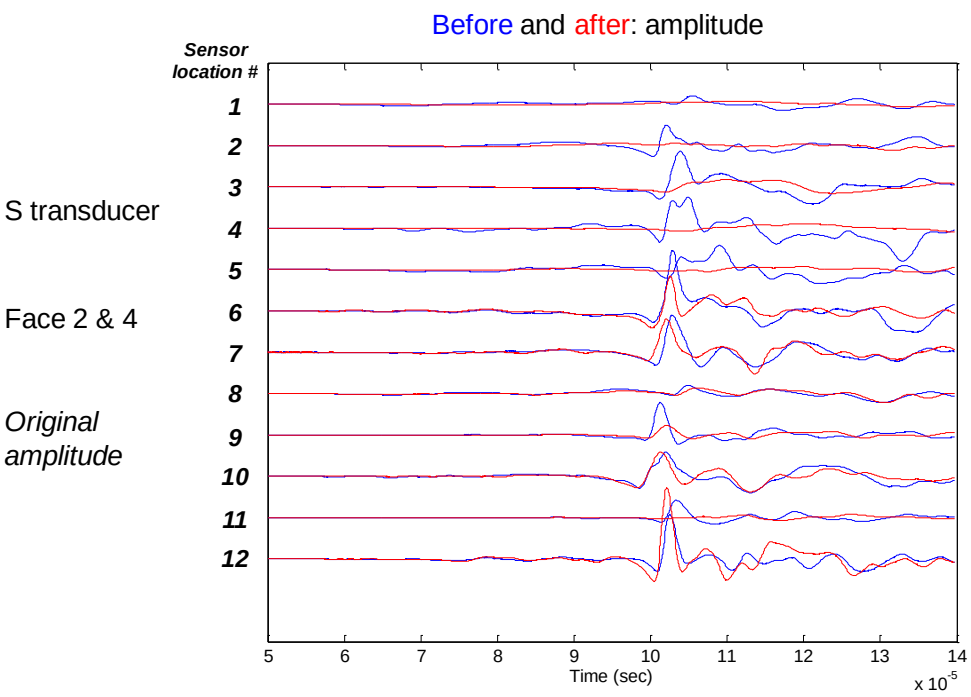

Figure 4.16 P and S wave amplitudes before and after the thermal shock.

(a)

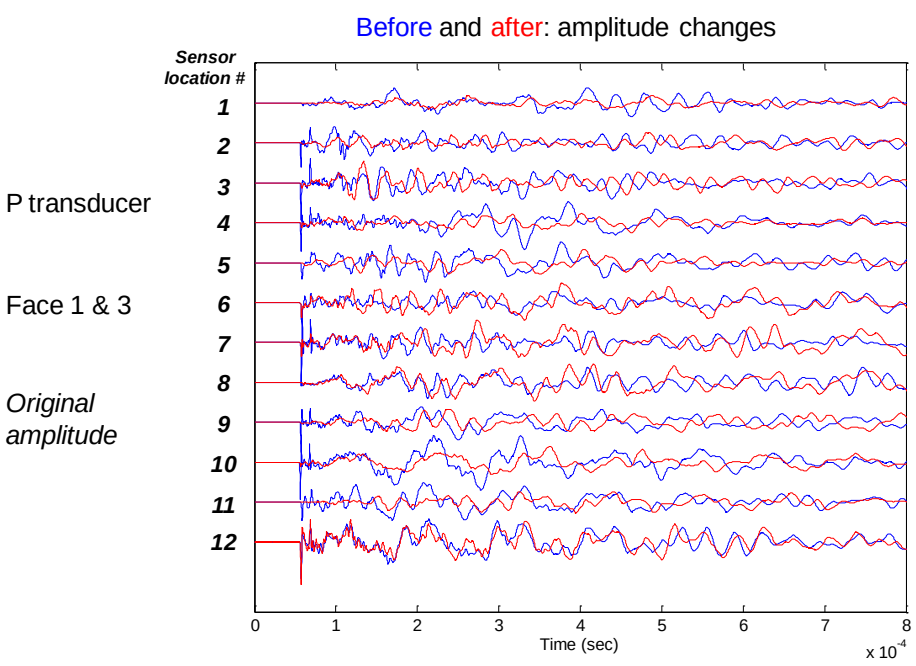
Before and after: amplitude changes
Sensor location #
1
2
3
4
5
6
7
8
9
10
11
12
P transducer
Face 1 & 3
Original amplitude
0
1
2
3
4
5
6
7
8
Time (sec)
x 10^-4

(b)

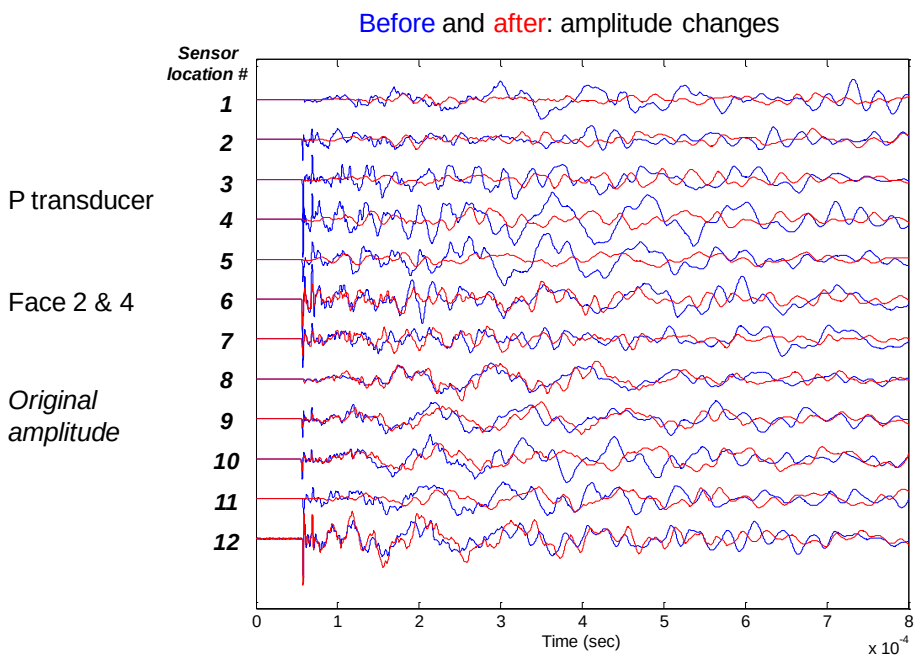
Before and after: amplitude changes
Sensor location #
1
2
3
4
5
6
7
8
9
10
11
12
P transducer
Face 2 & 4
Original amplitude
0
1
2
3
4
5
6
7
8
Time (sec)
x 10^-4

(c)

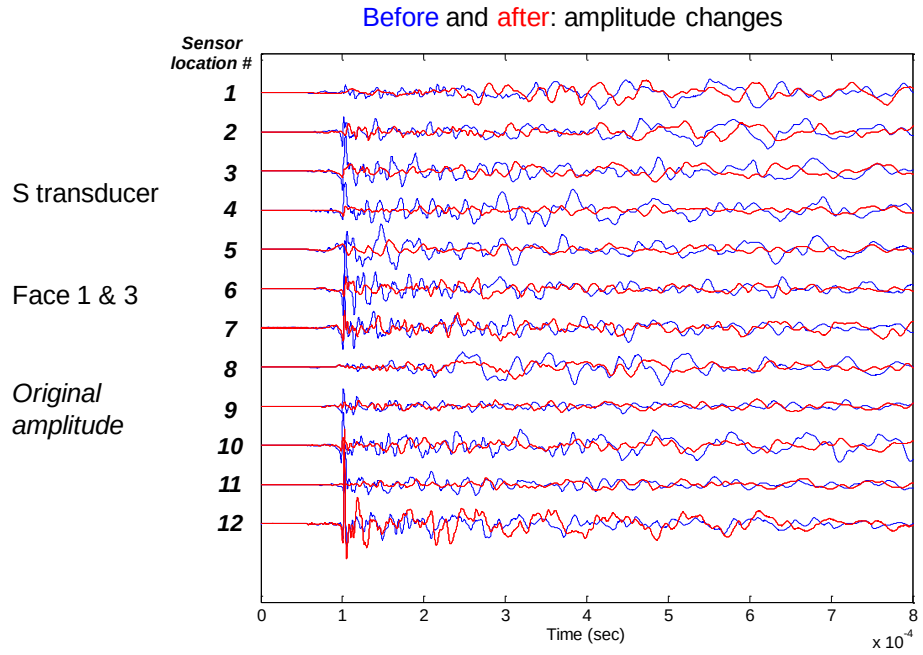

(d)

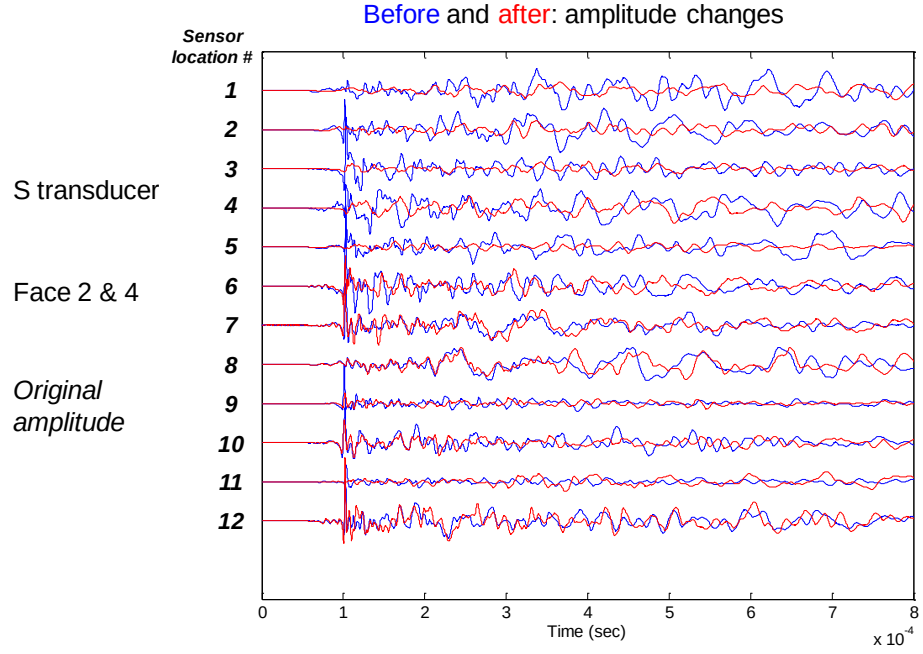

Figure 4.17 Global waveforms before and after the thermal shock.

4.3.2 Testing with a Confined Packer

In this test, we used the same concrete block that was used for the 1st test with the unconfined packer. For this experiment, a special structure is designed and fabricated to withstand some borehole pressure caused by vaporization (~10 psi) and future application of borehole pressurizations (up to ~500psi). A pressure transducer is attached to monitor borehole pressure, and a scale is used to record liquid nitrogen consumption. For safety, we made sure that top and bottom plates which are made of carbon-steel are not subjected to temperatures lower than -20°C to ensure that it does not reach the brittle-ductility transition point.

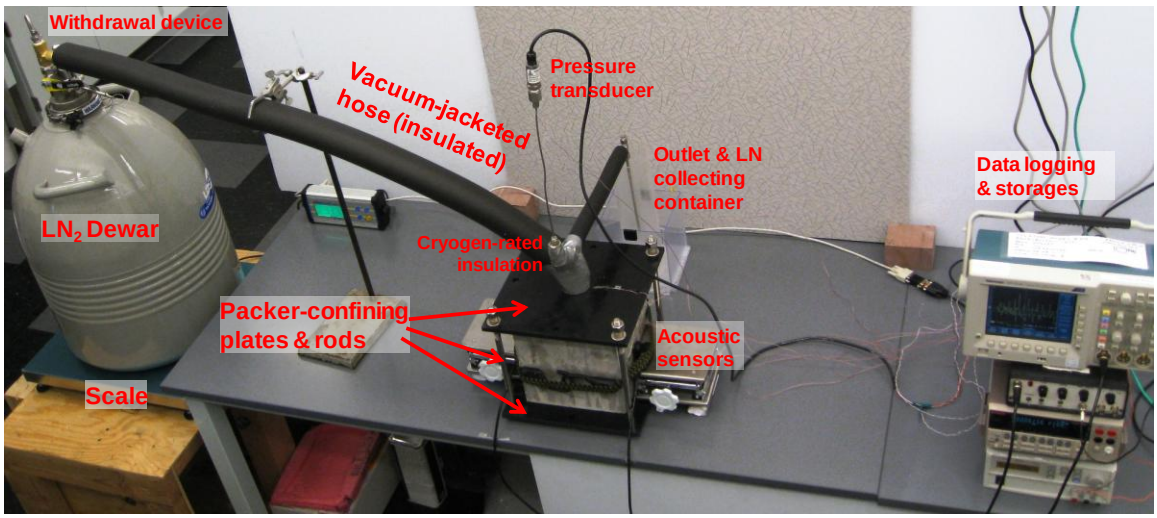

Figure 4.18 Experimental setup with "packer-confining structure"

Cracks

Major cracks were visible from the top of the borehole (Figure 4.19). However, there has been no noticeable change from the 1st thermal shock. Cracks at the borehole wall were visible from the borescope.

On the other hand, new cracks were generated on the block surfaces, and the existing cracks were a bit widened (Figure 4.20).There were relatively a small number of cracks at the bottom before applying the cryogen (after the 1st stimulation); however, many new cracks were created after the 2nd cryogen application.

The specimen was X-ray CT scanned at the Weatherford Lab at Golden, Colorado. The maximum resolution of the images from the scanner (Toshiba Aquilion 64) is 0.3mm×0.3mm×0.3mm. Thus, the CT images from the scanner shows only major cracks. Unfortunately, micro cracks were invisible from the scanned images. The X-ray images at the front and back of the specimen experienced artifacts called beam hardening as the cubic specimen enters and exits the X-ray field (Figure 4.21).

The CT images show that there are more fractures near the surfaces than inside. The animation of X-ray slides from a surface to a surface visualize shows the cracks distributed near the surfaces diminishes as it moves inside, although a few cracks exist independently internally.

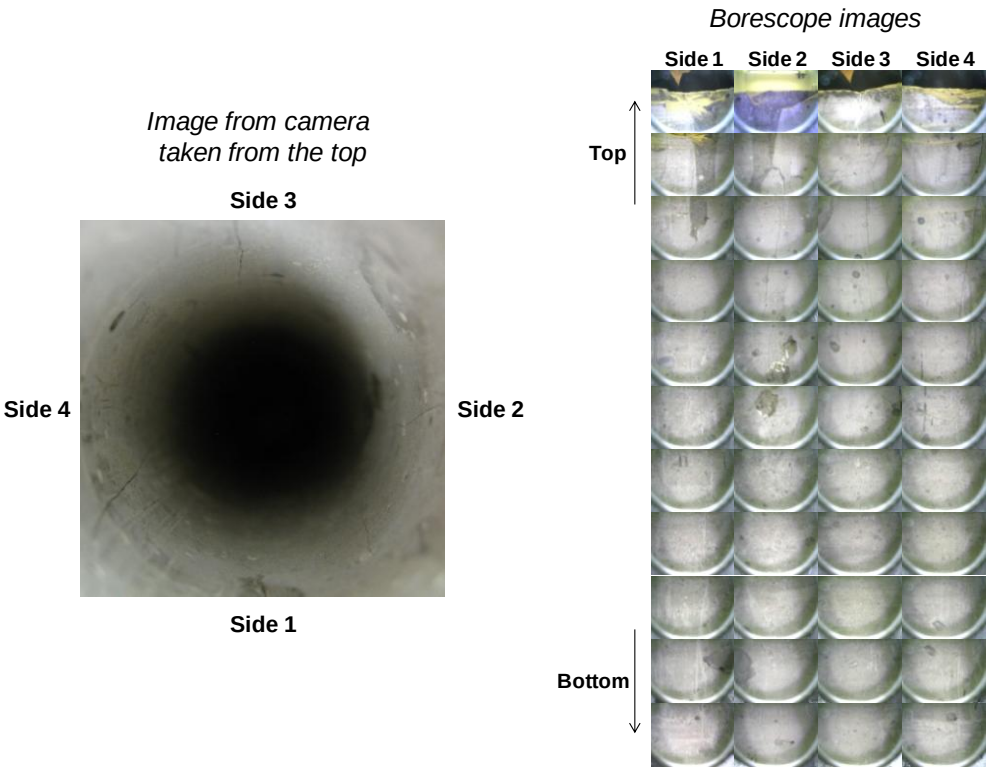

Figure 4.19 Cracks at the borehole walls observed from the top and the borescope.

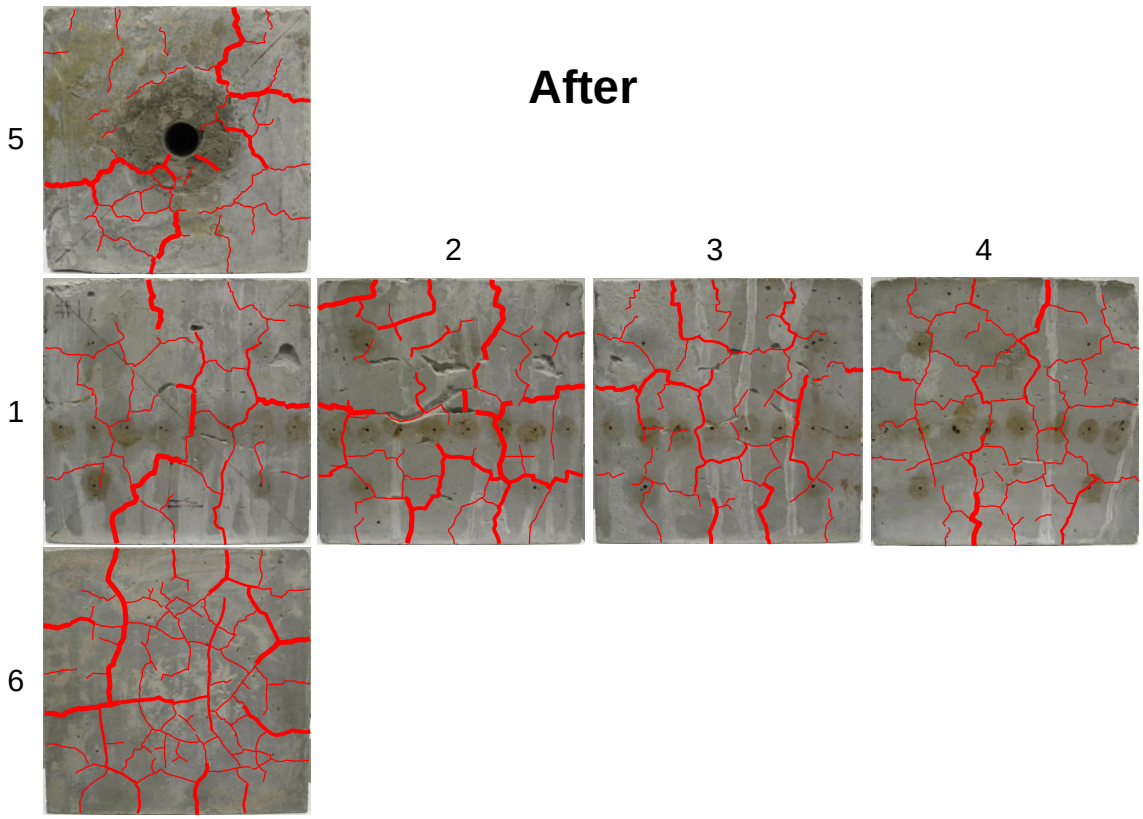

Figure 4.20 Surface cracks after the 2nd thermal shock – the superimposed lines are weighted according to the crack thickness.

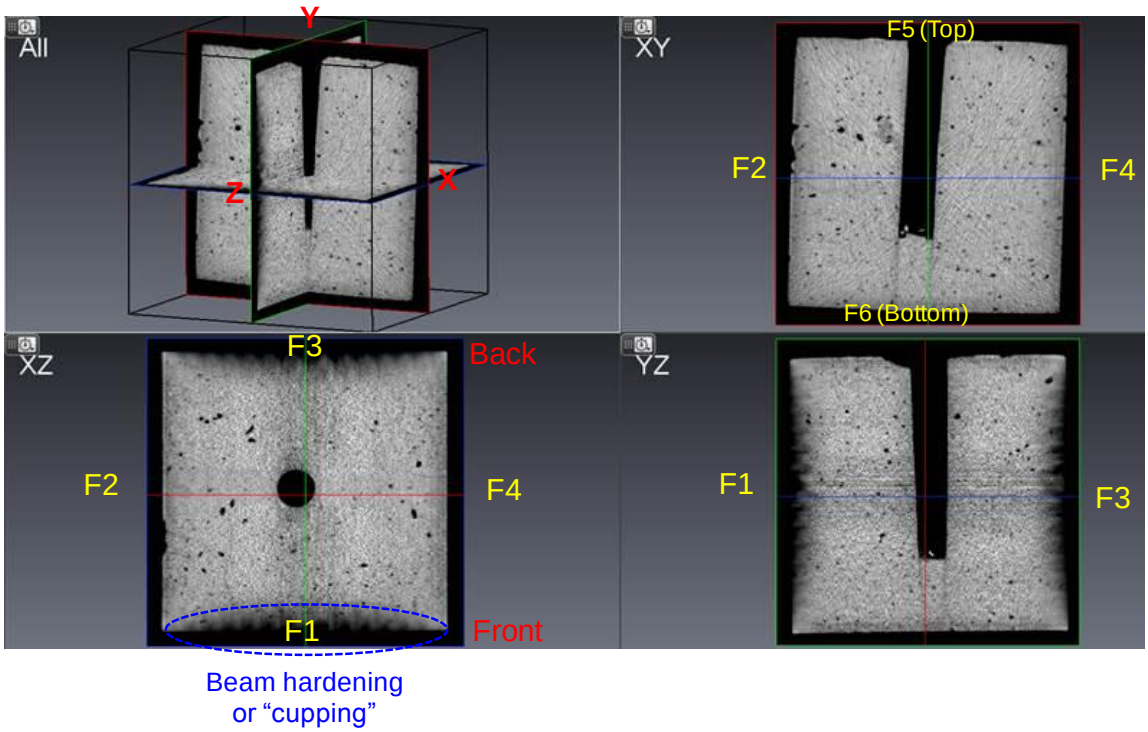

Figure 4.21 CT images: axis and direction.

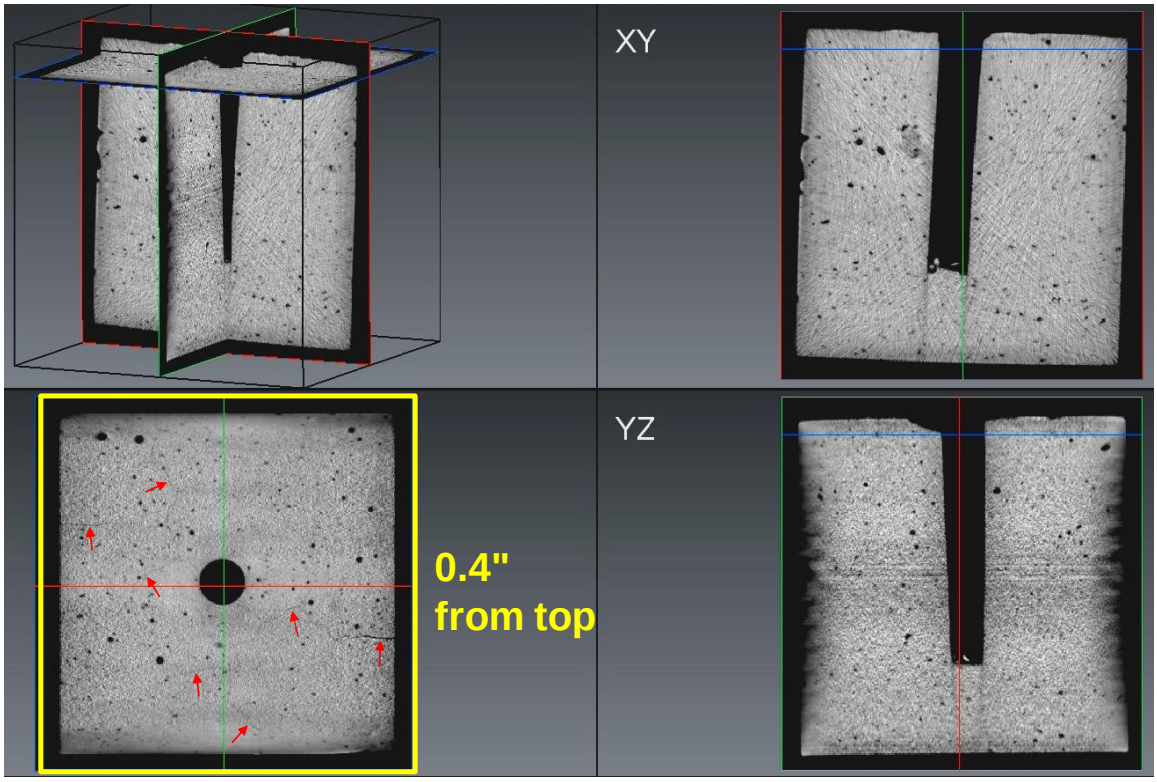

Figure 4.22 The CT slide at 0.4" from the top surface.

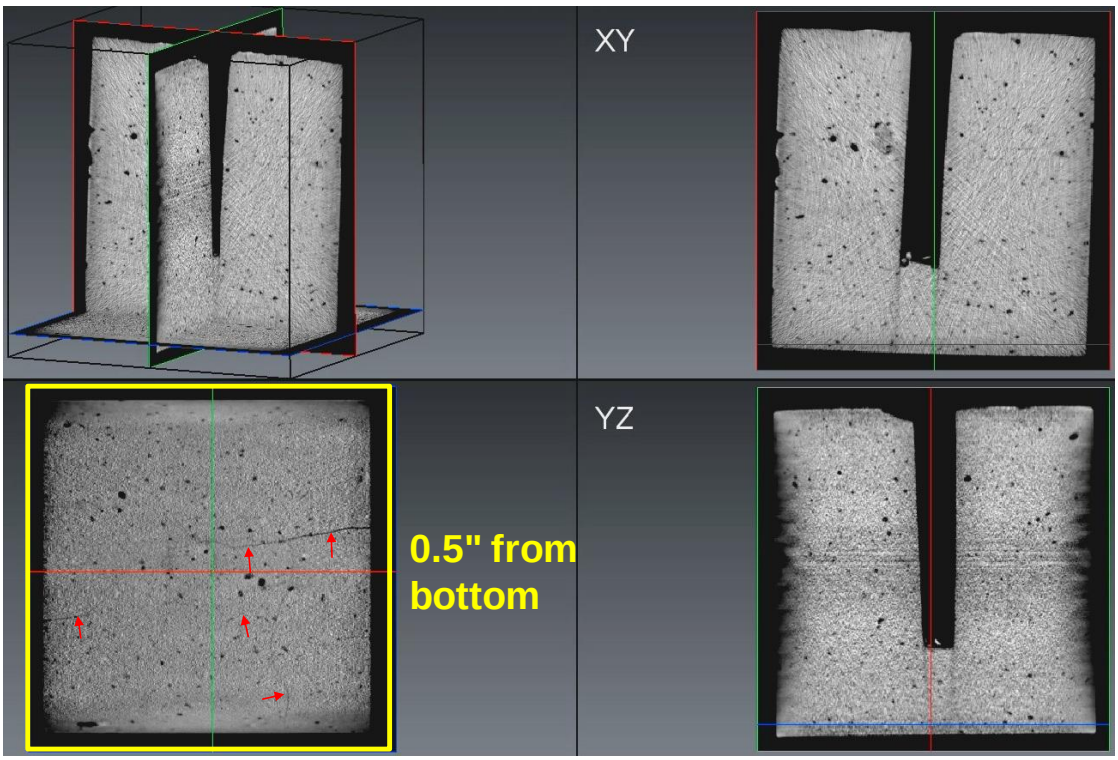

Figure 4.23 The CT slide at 0.5" from bottom.

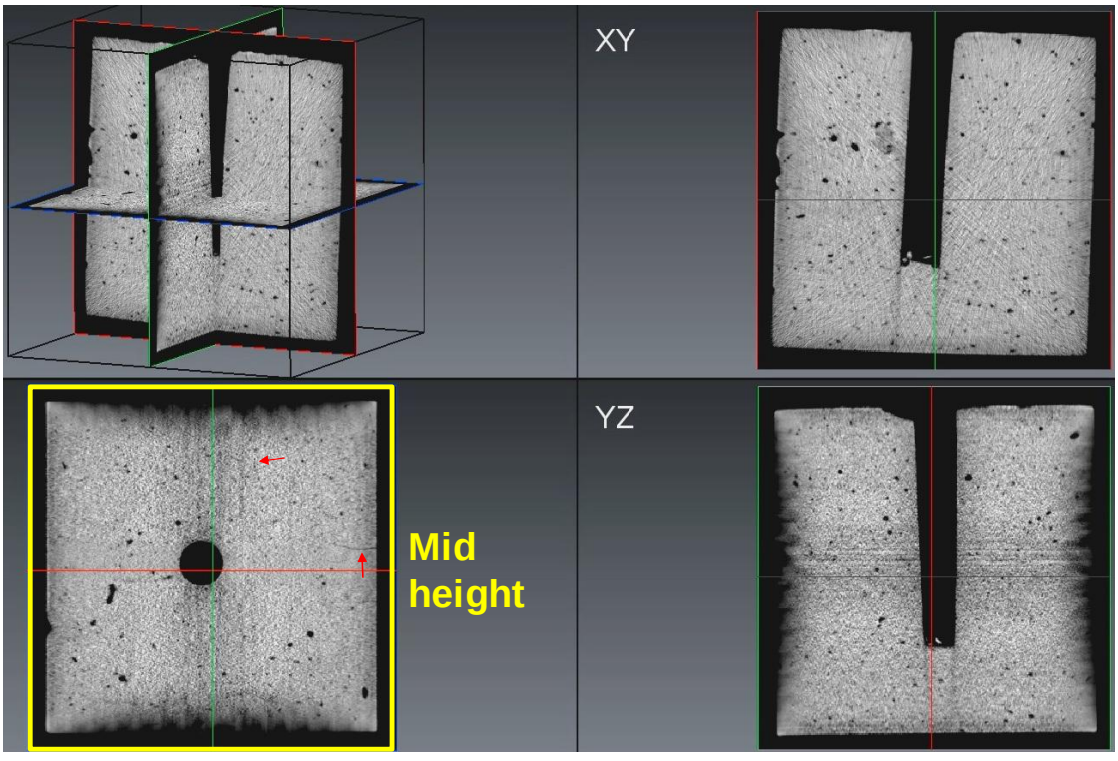

Figure 4.24 The CT slide at the mid height.

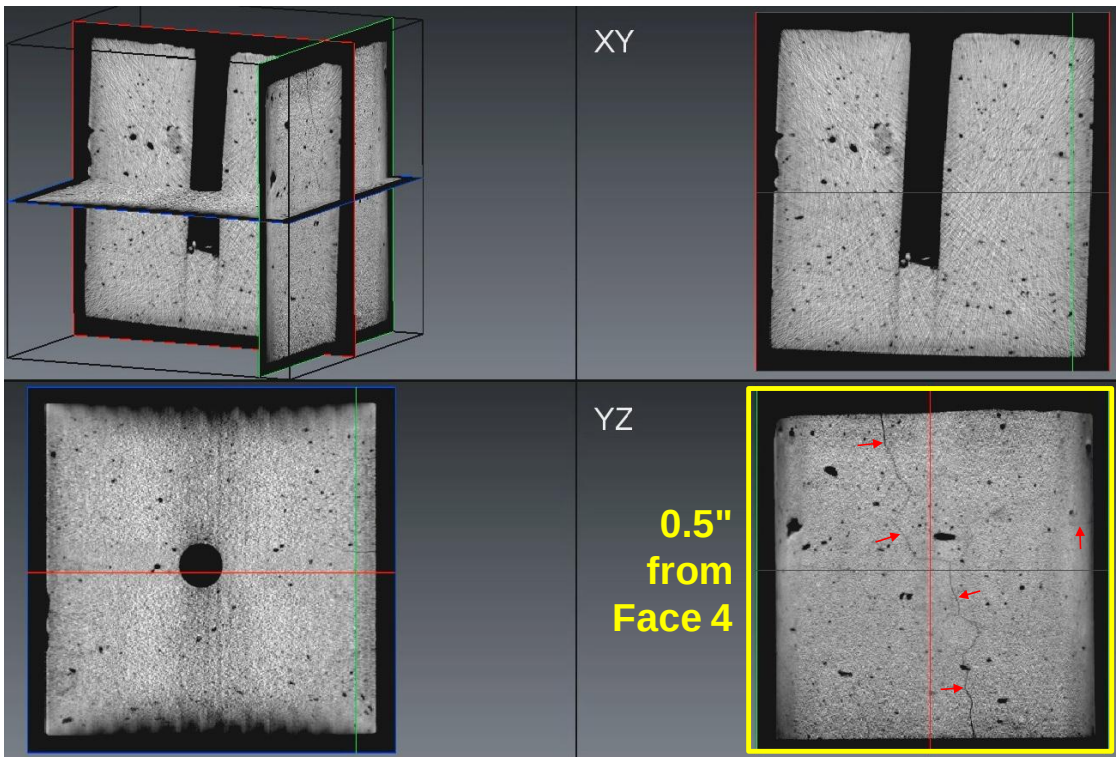

Figure 4.25 The CT slide at 0.5" away from Face 4.

Temperature, pressure, and liquid nitrogen consumption

Figure 4.27 shows the seven locations of the thermocouples (TC) where temperature is measured. TC #2 is hanging in the air inside the borehole, while TC #1 is attached to the borehole wall surface. Temperatures at the carbon steel plate (TC #4) and near the pressure transducer (TC #3) are monitored to protect the plates and the sensor.

The temperature evolution during the experiment at the seven locations is plotted in Figure 4.27. Throughout the test, the temperature difference between the inside of the borehole and the block face is observed to be large. It is observed that cooling at the borehole surface is slower. This is due to very large temperature difference between the surface and the liquid nitrogen. The liquid nitrogen immediately boils off at near contact with the surface, creating a vapor cushion between the LN2 and the surfaces. The gas nitrogen has a much lower thermal conductivity than the LN2, thus delaying the heat transfer to the rock surface. This phenomena is called the Leidenfrost effect. We had to repeat partially closing and opening the Dewar lever to control the amount of GN & LN leaking out through fractures and at the outlet as well for safety (Note that the top surface of the block had some fractures from the 1^{st} thermal shock). It is observed that the temperature inside the borehole is sensitive to lever operations.

The amount of LN flowed out of Dewar is monitored using a scale. The nonlinear curve of LN consumption vs. time at the initial part before the first partial closure shows that more vaporization occurs at the beginning and as the system cools down, increasing the amount of liquid nitrogen that comes out from the Dewar (Figure 4.28). The pressure is generated due to rapid vaporization at the borehole and along transport lines. The changes in pressure clearly correspond to the Dewar lever operation (Figure 4.28).

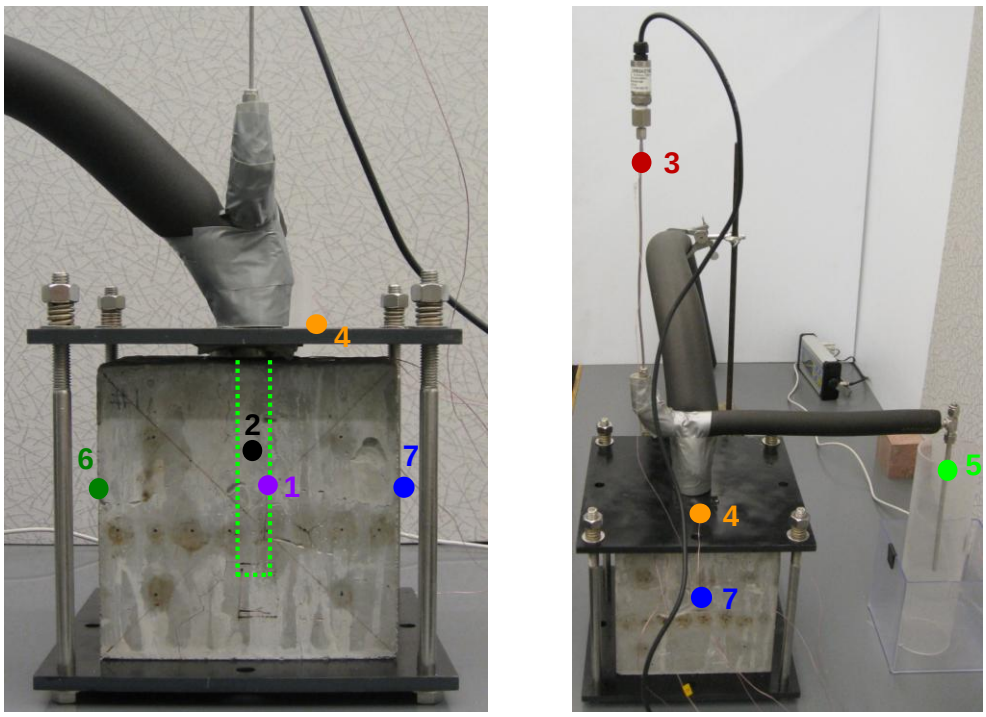

Figure 4.26 Locations of thermocouple tips

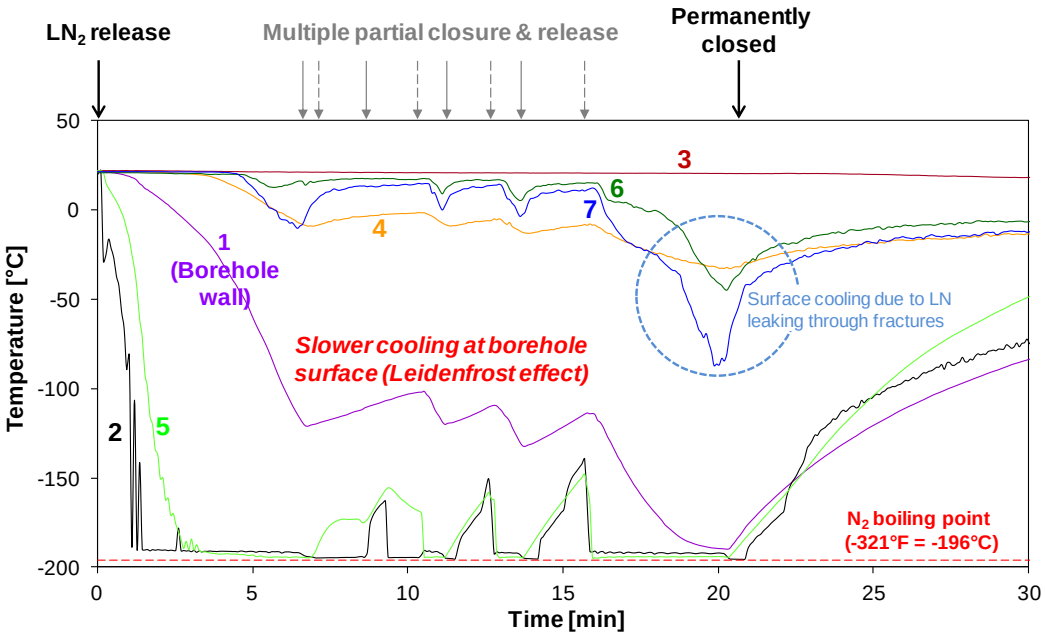

Figure 4.27 Temperature vs. time during testing.

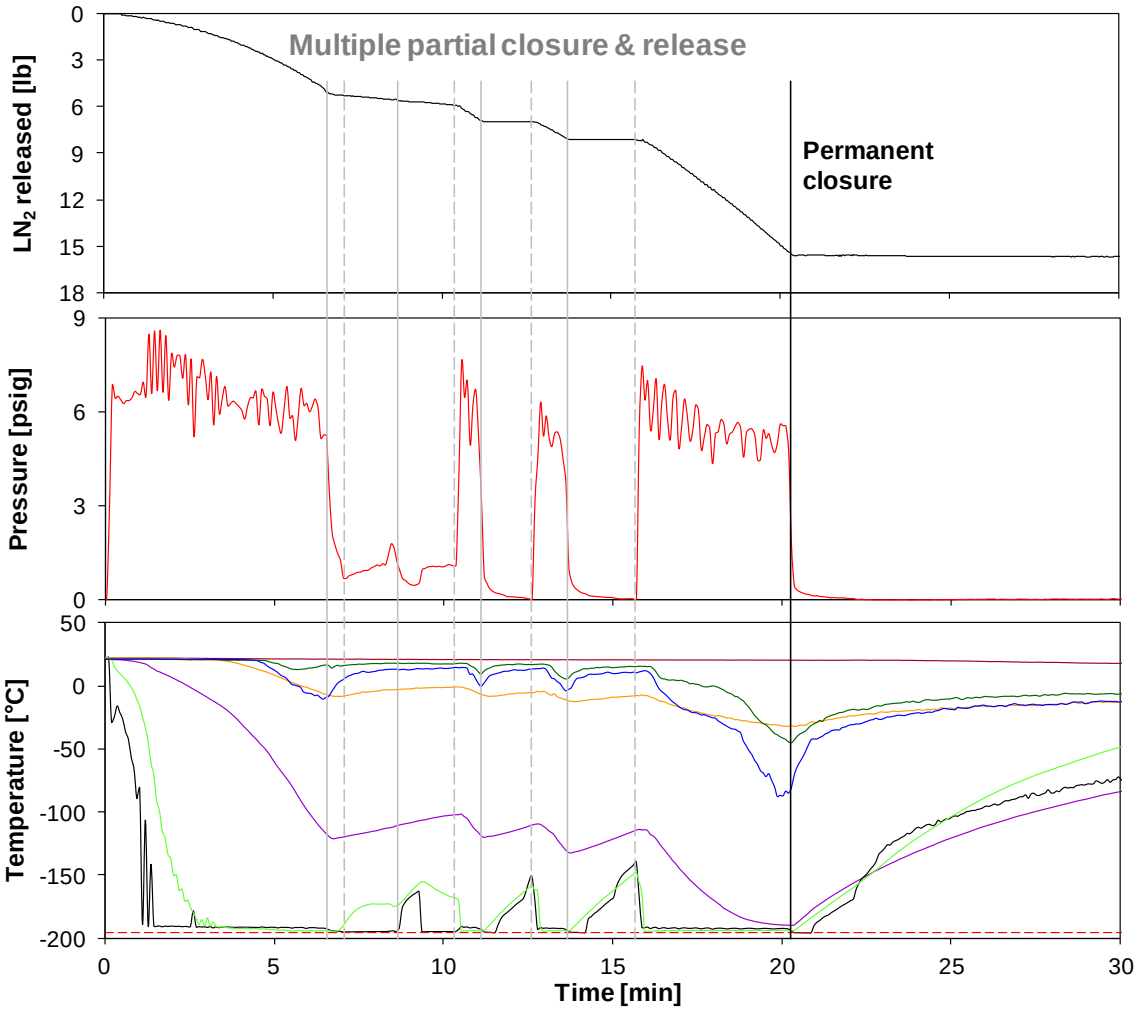

Figure 4.28 Synchronized plots of LN_2 consumption, temperature, and pressure with time.

Acoustic signatures

Similar to the case of the 1st thermal shock, in all locations, the P and S wave velocity decreased after the cryogenic stimulation (Figure 4.29). Wave amplitudes reduced significantly (Figure 4.30), and global wave amplitudes were reduced (Figure 4.31) after the cryogenic fracturing in most locations. Higher frequency contents are more filtered after the stimulation. An analysis for the quantitative changes in velocity and frequency contents will be performed in the future.

(a)

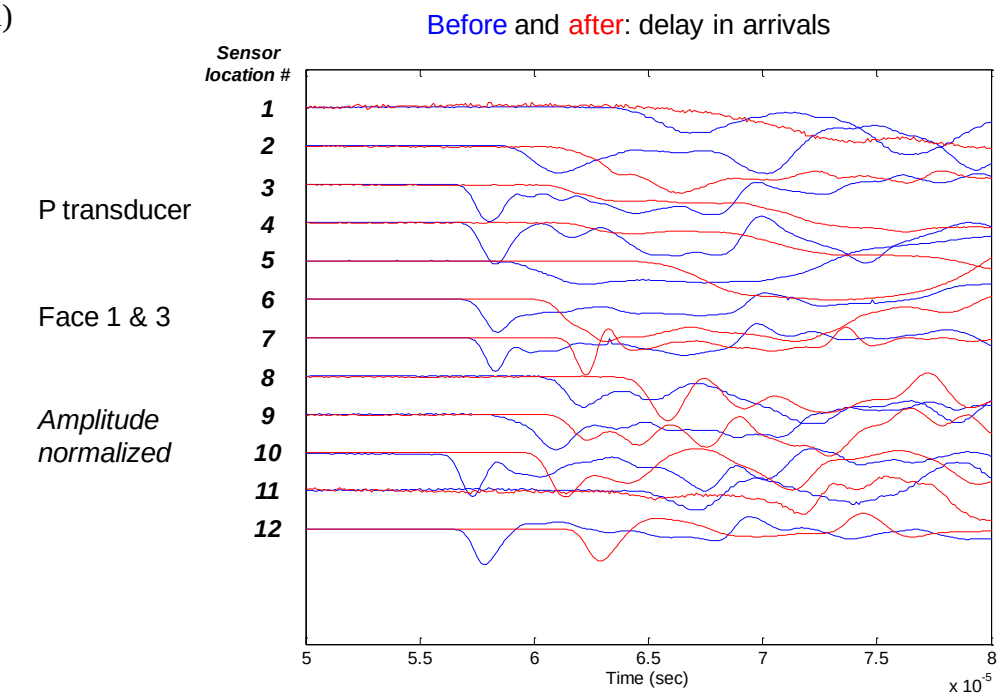
Before and after: delay in arrivals
Sensor location #
1
2
3
4
5
6
7
8
9
10
11
12
P transducer
Face 1 & 3
Amplitude normalized
5
5.5
6
6.5
7
7.5
8
Time (sec)
x 10^-5

(b)

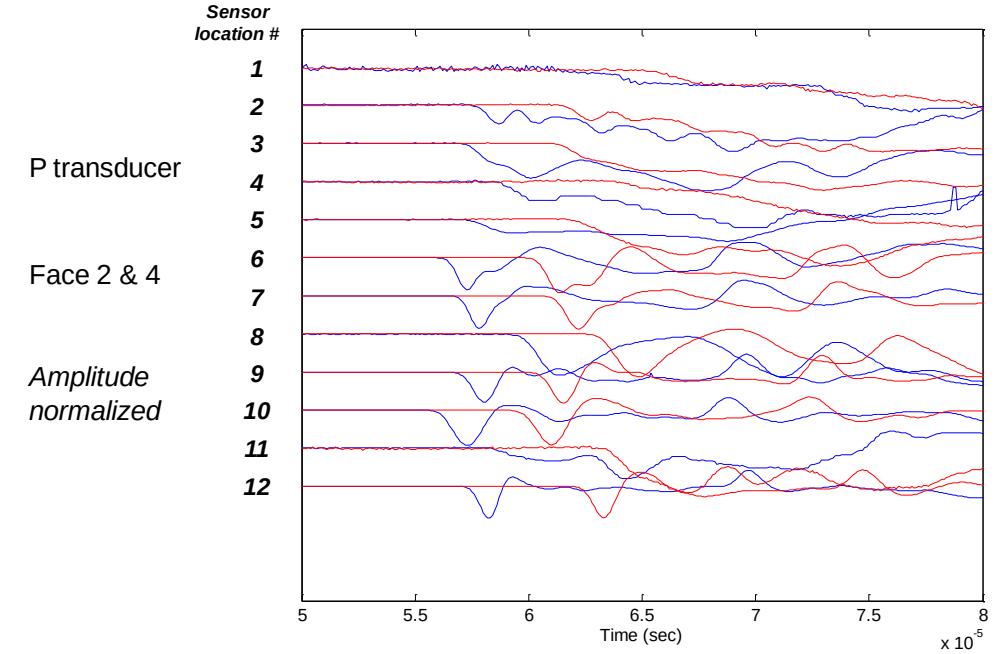
Before and after: delay in arrivals
Sensor location #
1
2
3
4
5
6
7
8
9
10
11
12
P transducer
Face 2 & 4
Amplitude normalized
5
5.5
6
6.5
7
7.5
8
Time (sec)
x 10^-5

(c)

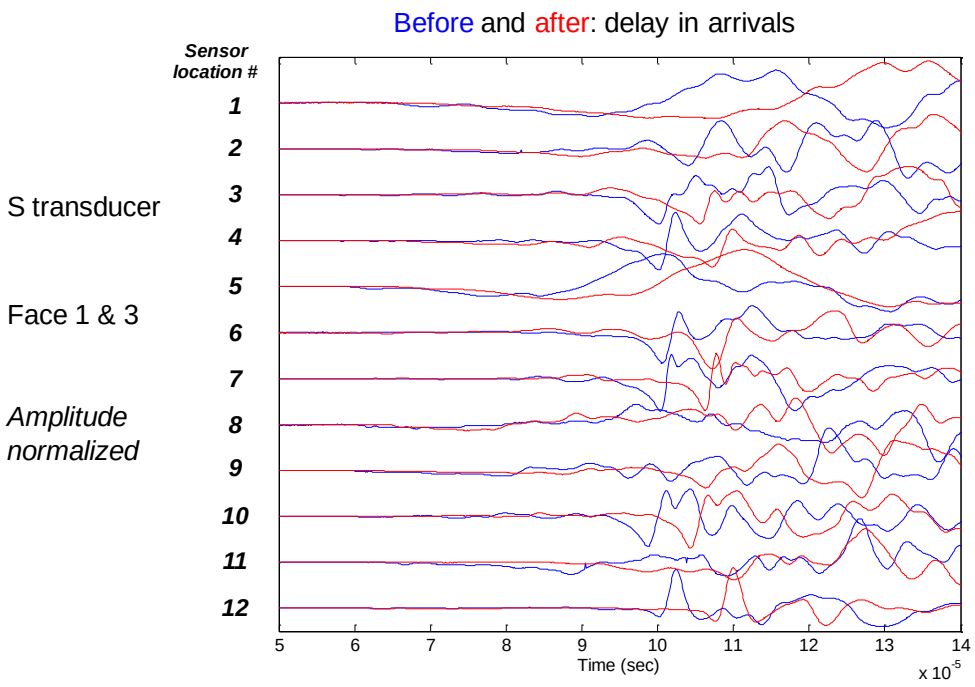

(d)

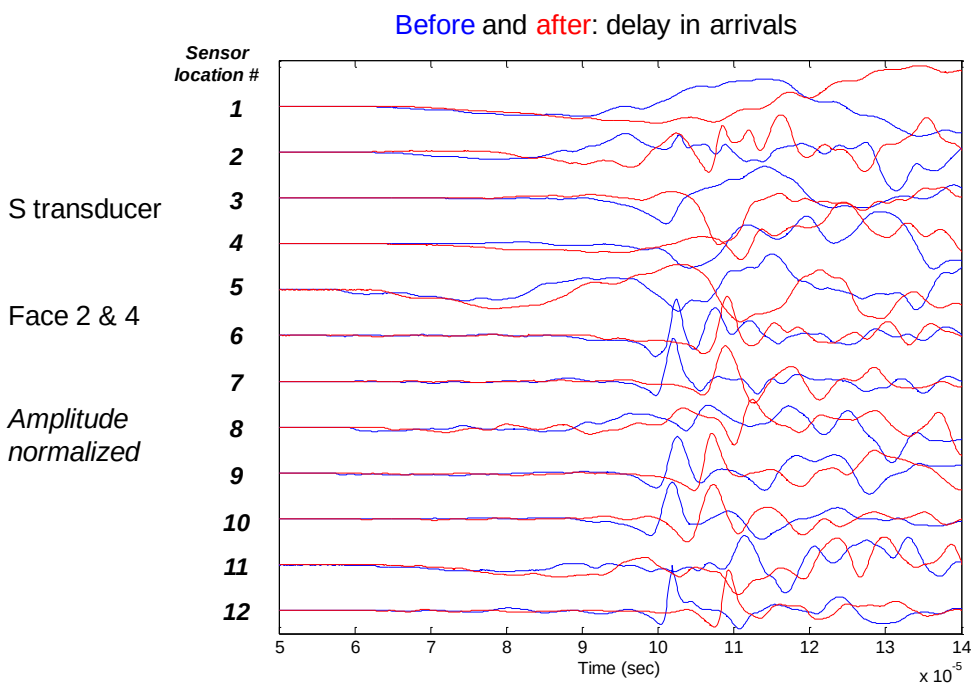

Figure 4.29 P and S wave arrivals before and after the thermal shock (compared with normalized amplitude).

(a)

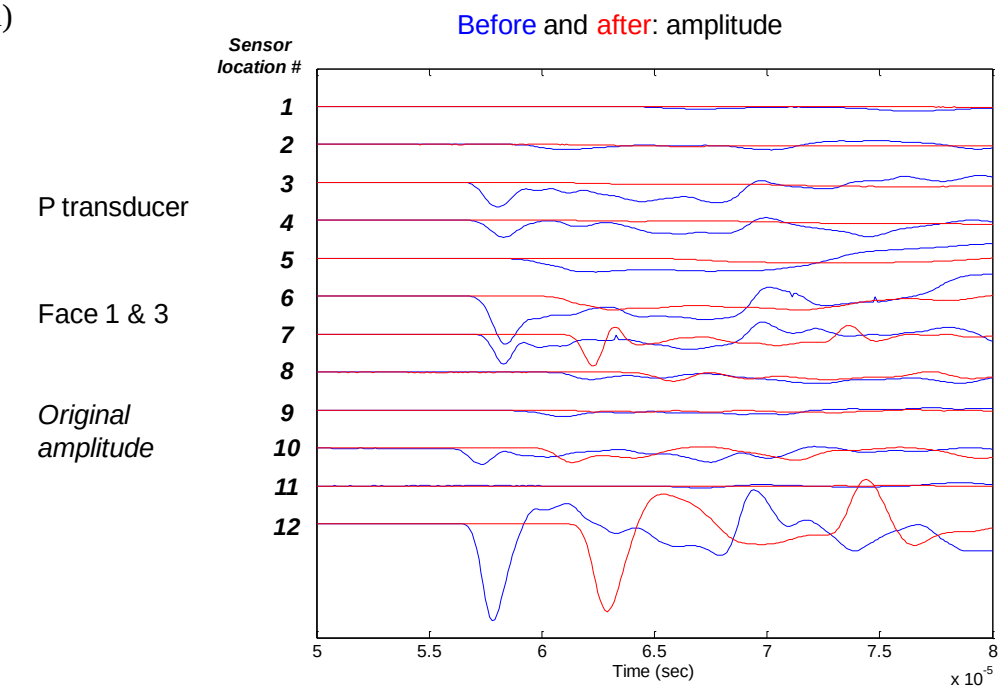
Before and after: amplitude
Sensor location #
1
2
3
4
5
6
7
8
9
10
11
12
P transducer
Face 1 & 3
Original amplitude
5
5.5
6
6.5
7
7.5
8
Time (sec)
x 10-5

(b)

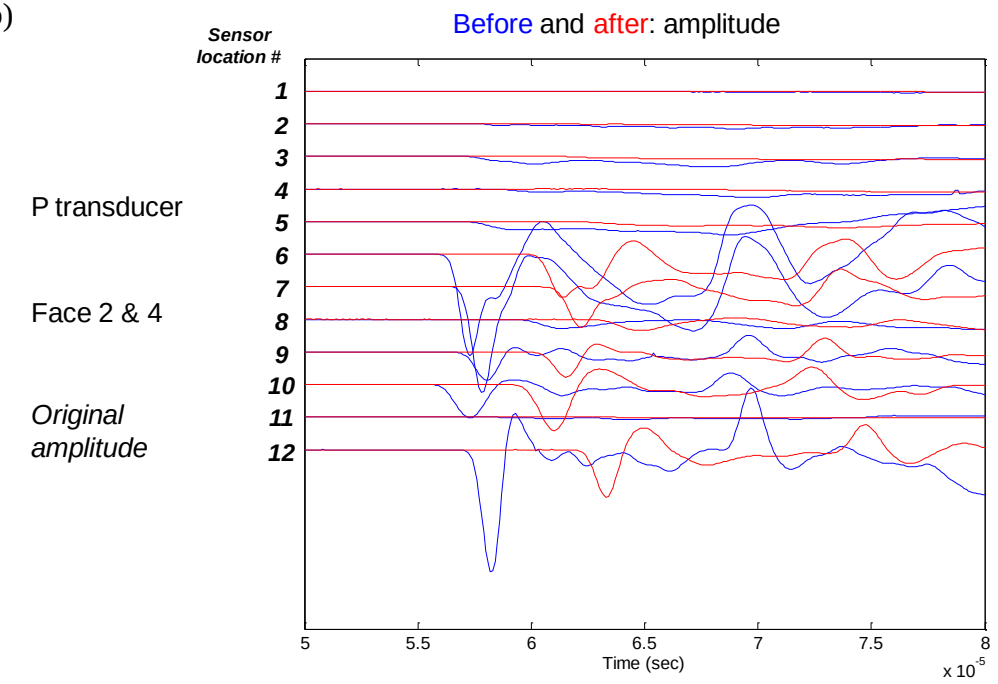
Before and after: amplitude
Sensor location #
1
2
3
4
5
6
7
8
9
10
11
12
P transducer
Face 2 & 4
Original amplitude
5
5.5
6
6.5
7
7.5
8
Time (sec)
x 10-5

(c)

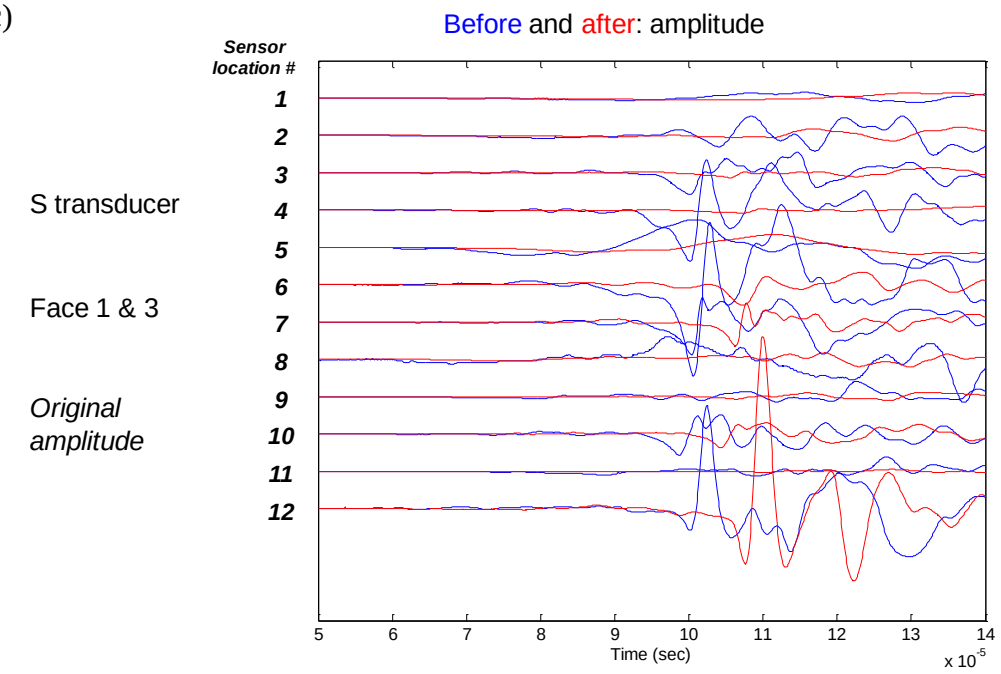

(d)

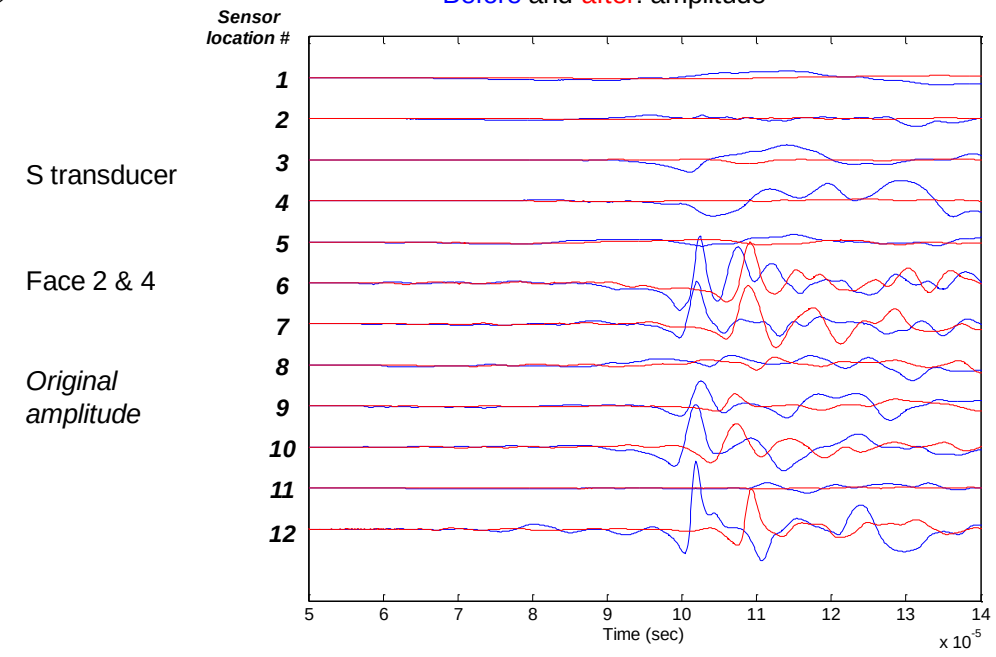

Figure 4.30 P and S wave amplitudes before and after the thermal shock.

(a)

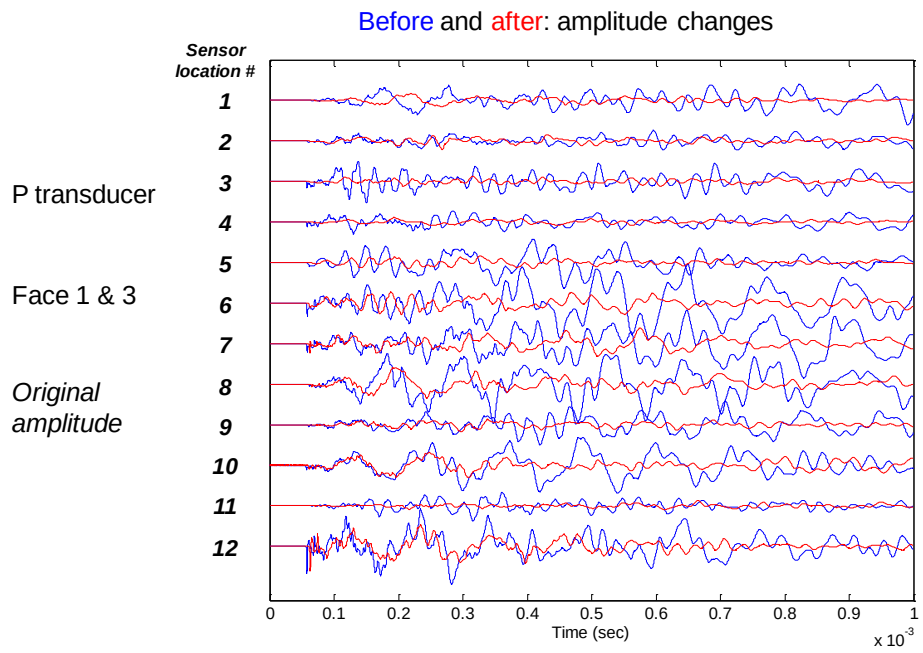
Before and after: amplitude changes
Sensor location #
1
2
3
4
5
6
7
8
9
10
11
12
P transducer
Face 1 & 3
Original amplitude
0
0.1
0.2
0.3
0.4
0.5
0.6
0.7
0.8
0.9
1
Time (sec)
x 10-3

(b)

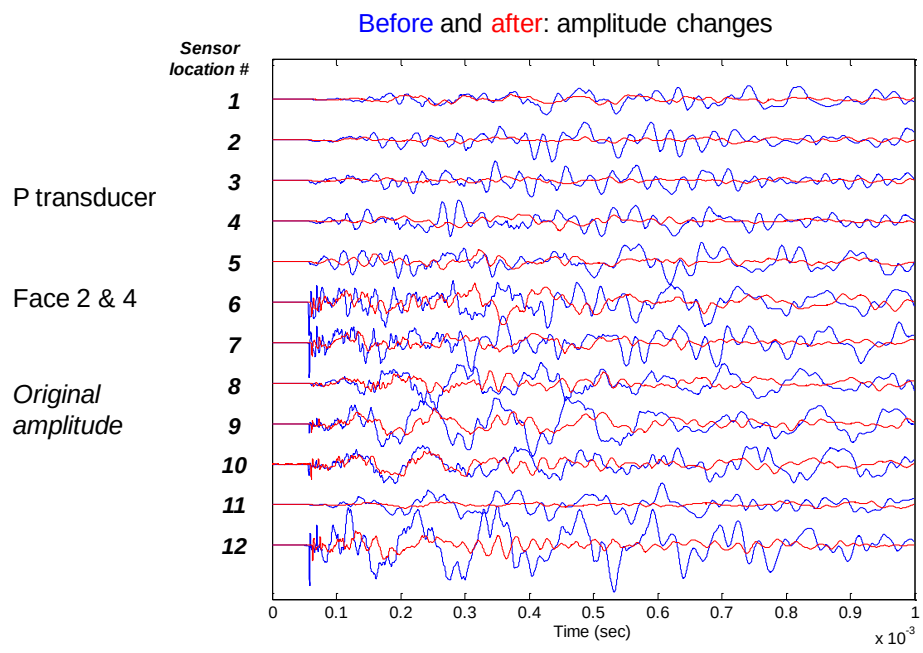
Before and after: amplitude changes
Sensor location #
1
2
3
4
5
6
7
8
9
10
11
12
P transducer
Face 2 & 4
Original amplitude
0
0.1
0.2
0.3
0.4
0.5
0.6
0.7
0.8
0.9
1
Time (sec)
x 10-3

(c)

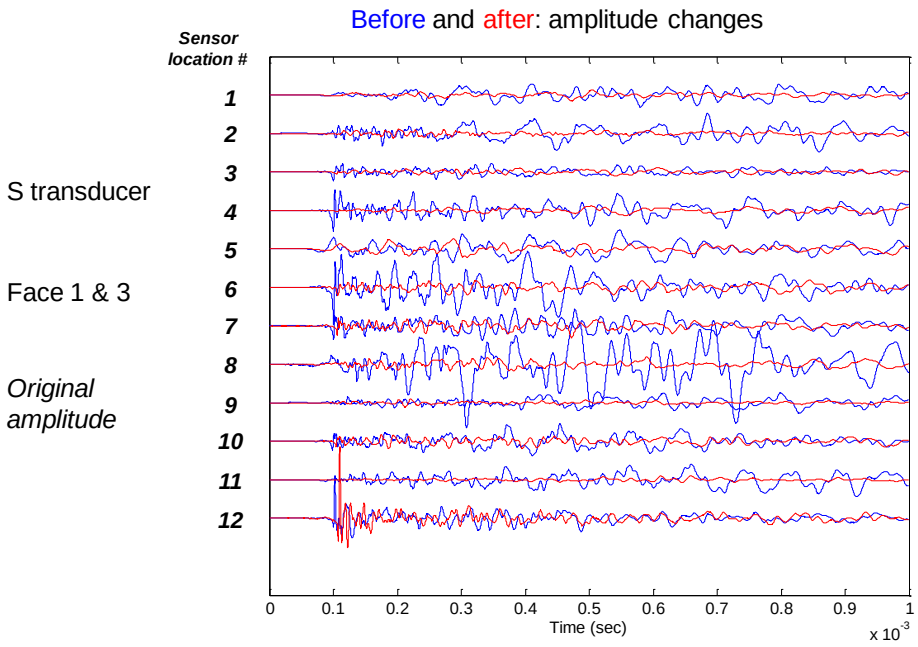

(d)

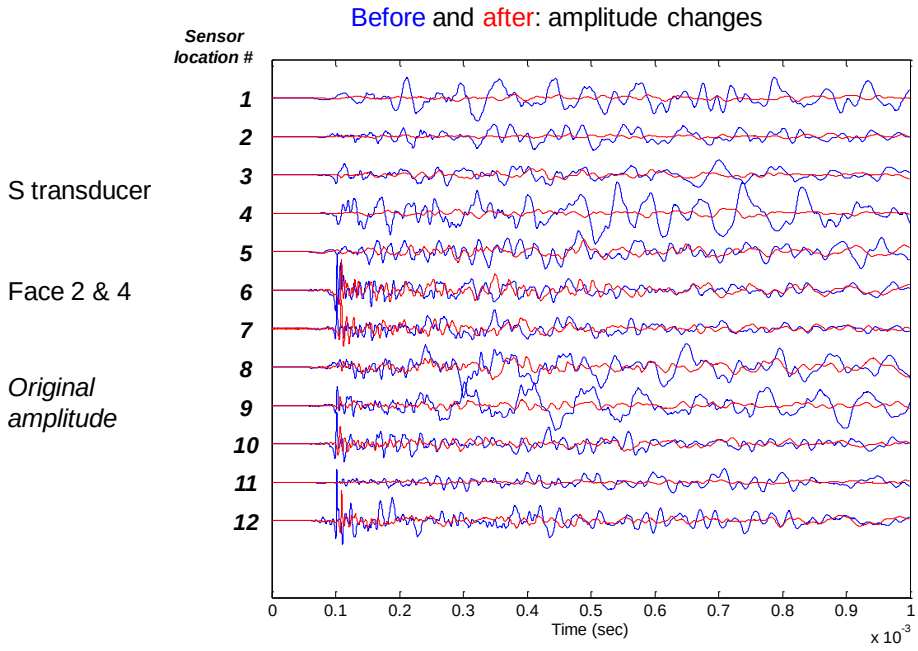

Figure 4.31 Global waveforms before and after the thermal shock.

Some other observations

The concrete specimen was already slightly cracked due to the 1st thermal shock at the surfaces of the borehole and the block. At the later stage of the experiment, fractures might have been opened up more, allowing significant nitrogen permeation. It is observed that the matrix became highly permeable to liquid nitrogen and gas through the fractures (Figure 4.32). The amount of leaking also depended on the release rate from the Dewar.

There were no leakages through the packer/rock interface. The epoxy seal and stainless steel packer with tubes connected all remained intact under the cryogenic temperature and the pressure conditions (Figure 4.33). The cryogen-rated insulation and plastic container remained functional. The upper plate (carbon steel) survived at low temperatures (~-30°C). One of the reasons why these are undamaged is that, unlike the borehole environment, temperature propagation is slower in the surrounding environment. Another reason could be that small volume does not create enough contraction to fail the materials and/or interfaces. The thermocouple's plastic insulation coat remained functional throughout the experiment. The block surfaces started to form frost once the temperature of the surface become well below the water-freezing point.

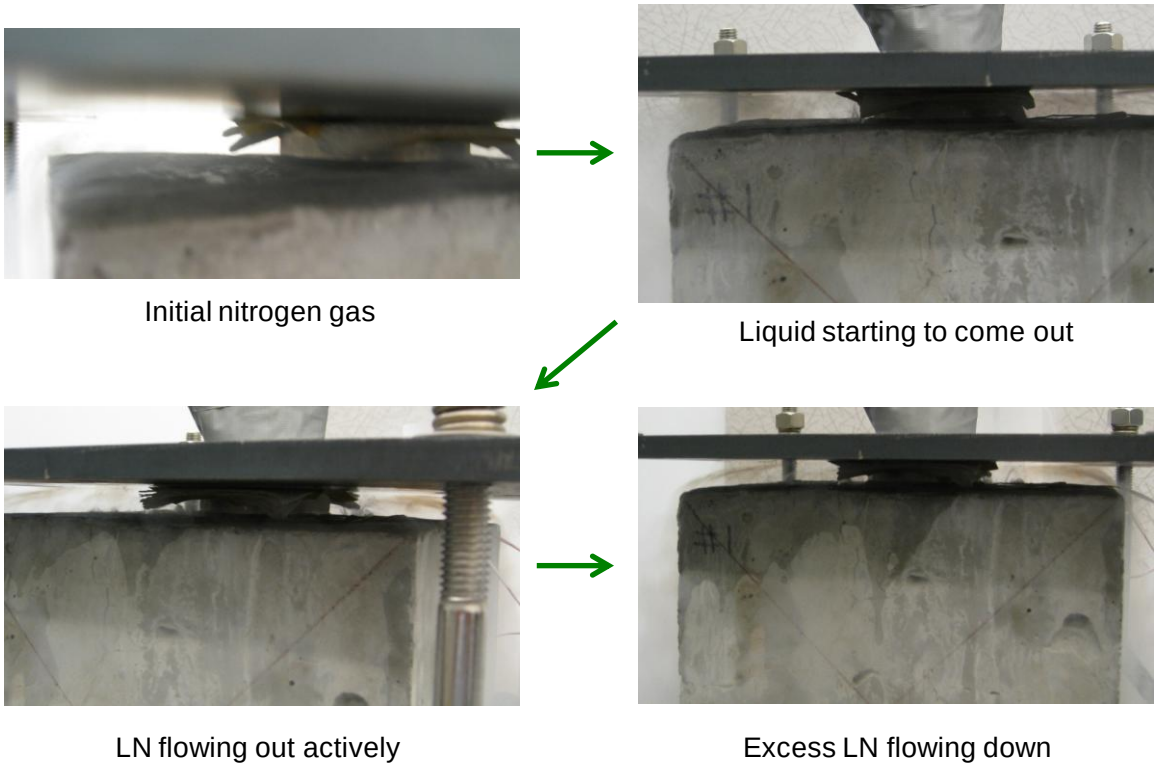

Figure 4.32 liquid nitrogen and gas nitrogen permeating through fractures

(a) Epoxy and stainless steel packer

(b) Insulations and carbon steel plates

Figure 4.33 Cryogenic performance of surrounding materials.

4.4 Thermal Shock and Pressurizations on Sandstone Specimen

Cryogenic stimulation experiments were performed on a sandstone specimen obtained from a local quarry in Denver. Multiple thermal shocks and pressurizations were applied to the specimen due to its more resistance to thermal shock than the previous concrete specimen. The following thermal stimulations are applied on the sandstone specimen.

a. The 1st thermal shock – cold nitrogen gas (4.4.1)
b. The 2nd thermal shock – cold nitrogen gas (4.4.2)
d. The 3rd thermal shock – liquid nitrogen) (4.4.3)
d. The 4th thermal stimulation – liquid nitrogen + pressurizations (4.4.4)

Note that in the 1st and 2nd thermal shocks, cold nitrogen gas was used for the thermal shock. It was not our intention, but rather due to a malfunction of the withdrawal device, which results in cold nitrogen gas instead of liquid nitrogen released during thermal shock. This problem was improved from the 3rd thermal shock.

4.4.1 Thermal Stimulation with Cold Nitrogen Gas

From this test, acoustic measurements are not conducted during the cryogenic stimulation due to risk of damage to the sensors.

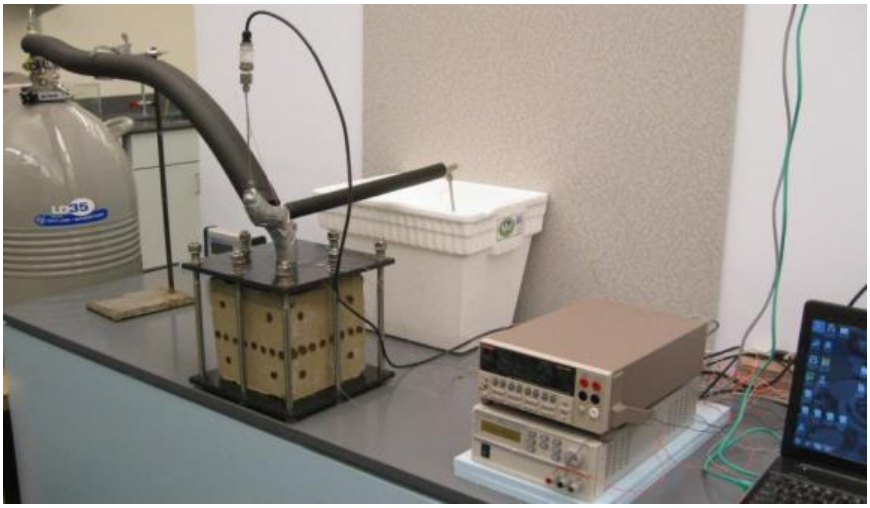

Figure 4.34 Experimental setup (the 1st thermal shock)

Temperature, pressure, and LN_2 consumption

The pressure inside the borehole is basically following a similar level to the pressure inside the Dewar (the pressure inside the borehole slightly less by about 1 psi). In this test, the Dewar was opened completely until the end of the test without partial or temporal closure in the middle (Figure 4.35). The high-frequency fluctuation of borehole pressure as shown in the plot is also indicated by the sound at the outlet.

Due to the malfunctioning of the withdrawal device, nitrogen exists as a gas state in the borehole throughout the test. This is also indicated by temperatures and the outlet content (no droplet of LN_2 observed throughout the test) (Figure 4.37)

The temperature in the borehole is significantly higher than LN_2 boiling point. There seems to be no indication of the Leidenfrost effect according to the temperature data.

At the end of the test, no noticeable cracks are found at the block surfaces by visible examination. Because we found no cracks and the thermal shock became inefficient, we performed the 2nd thermal shock (next section).

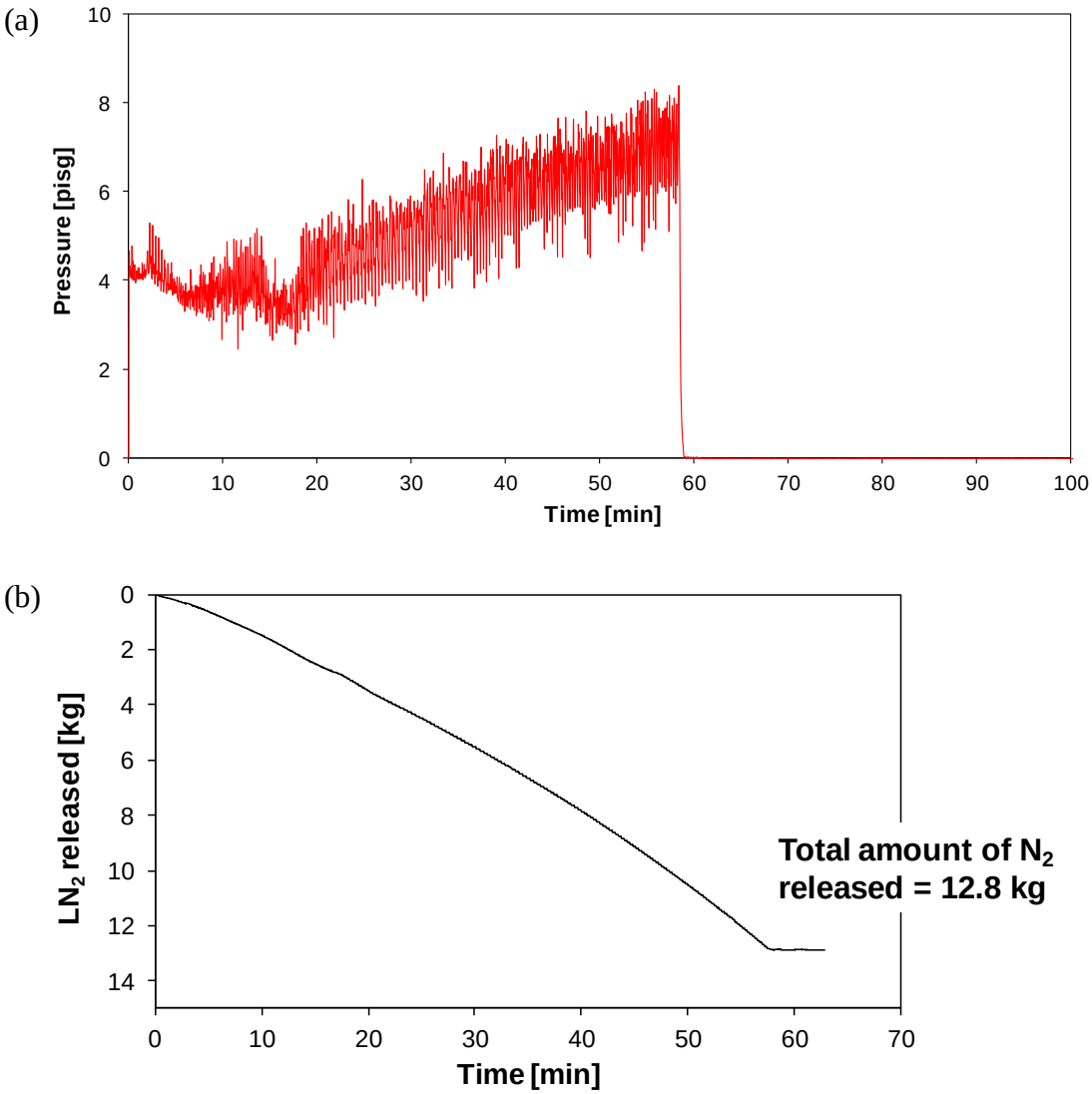

Figure 4.35 Pressure generated during nitrogen gas flow and LN2 consumption

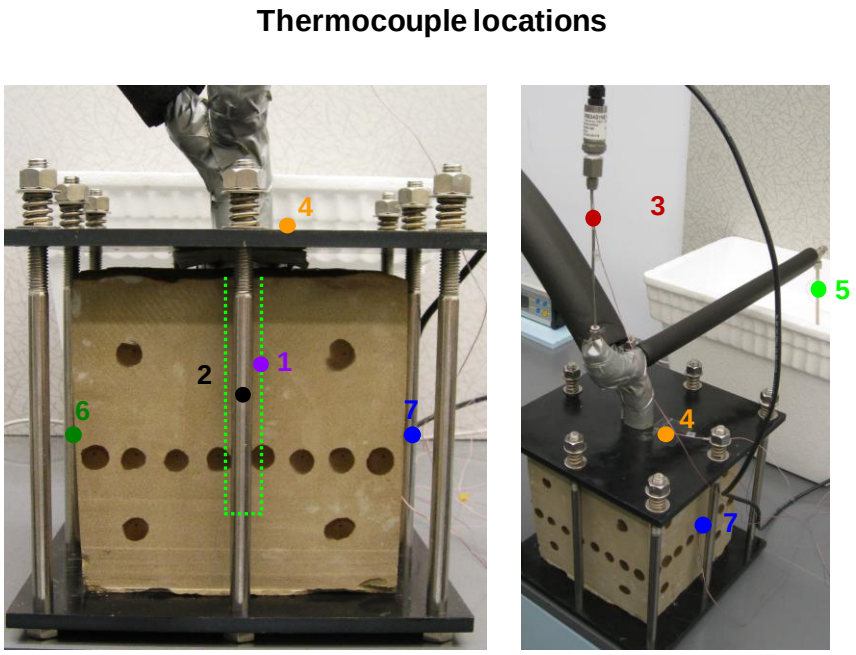

Figure 4.36 Locations of temperature sensors. Note that the dark spots are from the couplant used for the ultrasonic measurements.

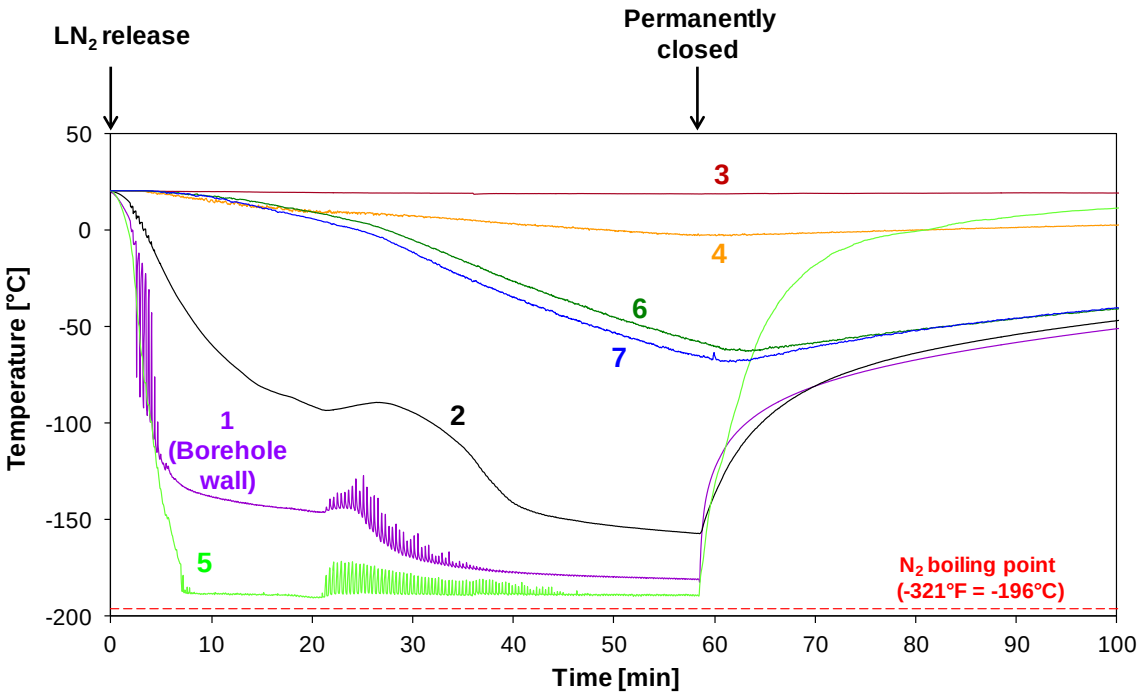

Figure 4.37 Temperature during the 1st thermal shock.

4.4.2 Thermal Stimulation with Cold Nitrogen Gas

In the 2nd thermal shock, the outlet is moved further back to prevent any accidental leakage from the outlet tank and to stay away from cold vapor (Figure 4.38). Again, due to malfunctioning of the withdrawal device, cold nitrogen gas instead of liquid nitrogen was release during the thermal shock. The pressure and nitrogen consumption follows similar trends as the previous test and thus are omitted here.

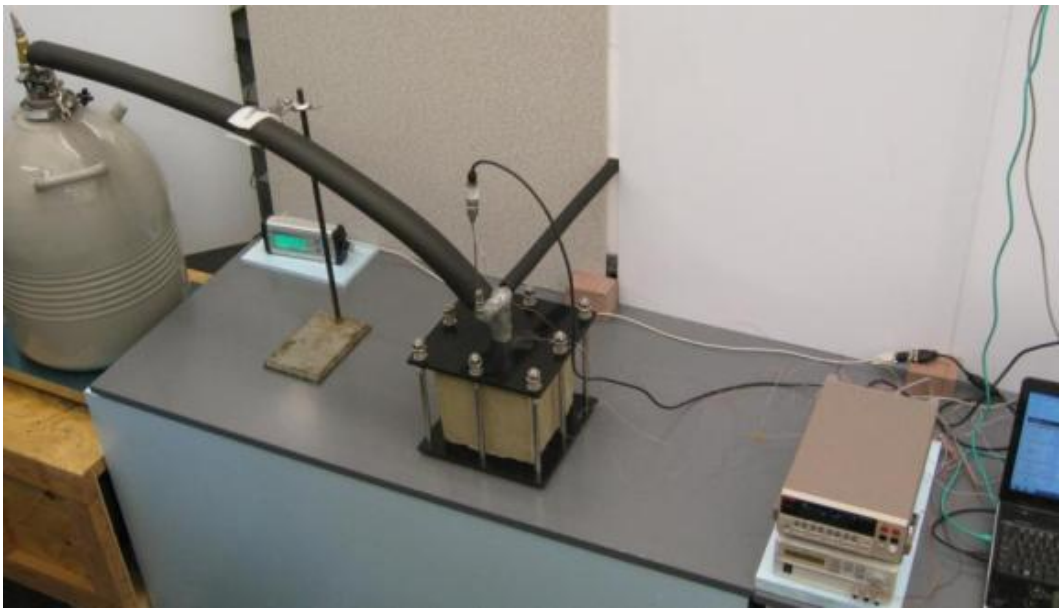

Figure 4.38 Experimental setup for the 2nd thermal shock.

Temperature and crack examination

Due to the lengthy duration of the experiment (75 minutes), even the surface of the rock become very low (as low as -70°C) (Figure 4.39). The high-frequency fluctuation of the temperature data (in TC #1,2,5) was also indicated by the flow sound at the outlet, which is related to the pressure changes in the borehole.

No noticeable cracks are generated after the two thermal shock, possibly due to slower dropping of temperature (causing lower thermal gradient) and higher final temperature, and possibly also the lower brittleness and the higher strength of the sandstone block.

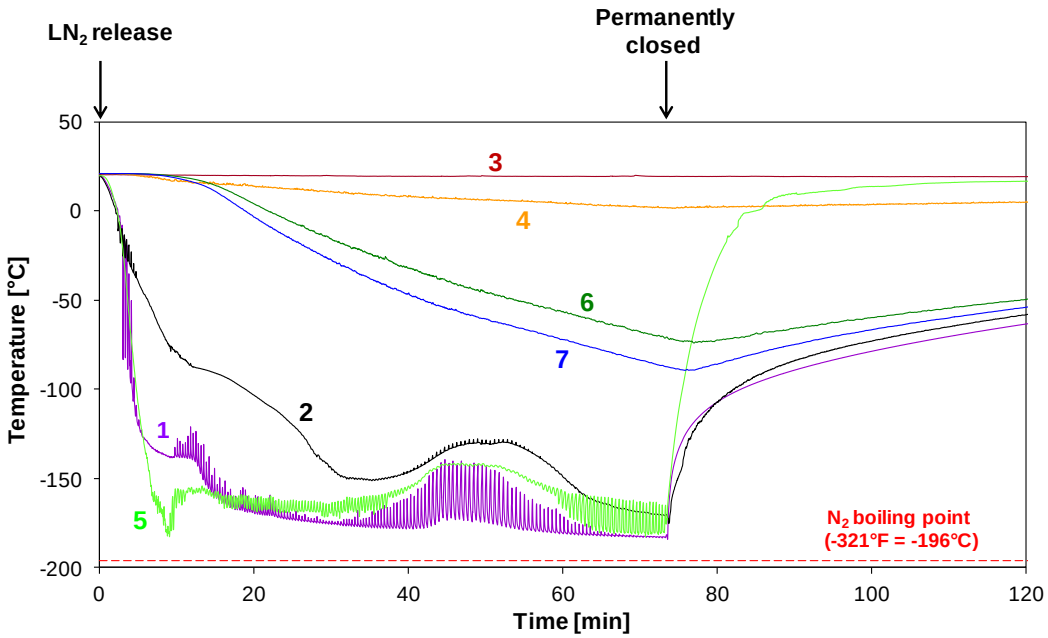

Figure 4.39 Temperature vs. time

Other observations

A significant amount of frost formed on the surface of the rock towards the end of the test (Figure 4.40). The frost was first noticed at the top and sides of the specimen, which are closer to the borehole.

After the 2nd thermal shock, the packer is examined and then dismantled to check its integrity in sealing. We confirmed that the sealing is good and the nitrogen passage was not interrupted (Figure 4.41).

At the end of test **3 hours after the test**

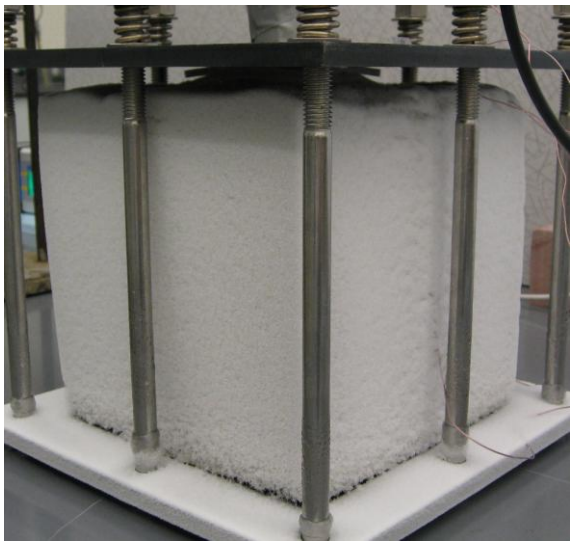

Figure 4.40 Frost attracted at the surfaces

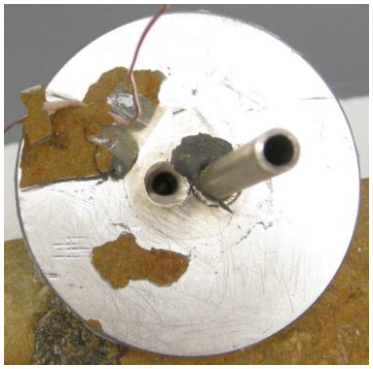

Figure 4.41 Packer and sealing: leakage and integrity check.

Air pressure decay test

The characteristics of air pressure decay over time can be a qualitative measurement of air permeability before cryogenic influence. Before any thermal shock, and after the 1st and 2nd thermal shocks, bulk air permeation tests were performed. Air pressure is applied to the borehole and the valve is closed to record the pressure decay over time using a pressure transducer. We have noticed only minute changes in the decay profile.

Figure 4.42 Air pressure decay test

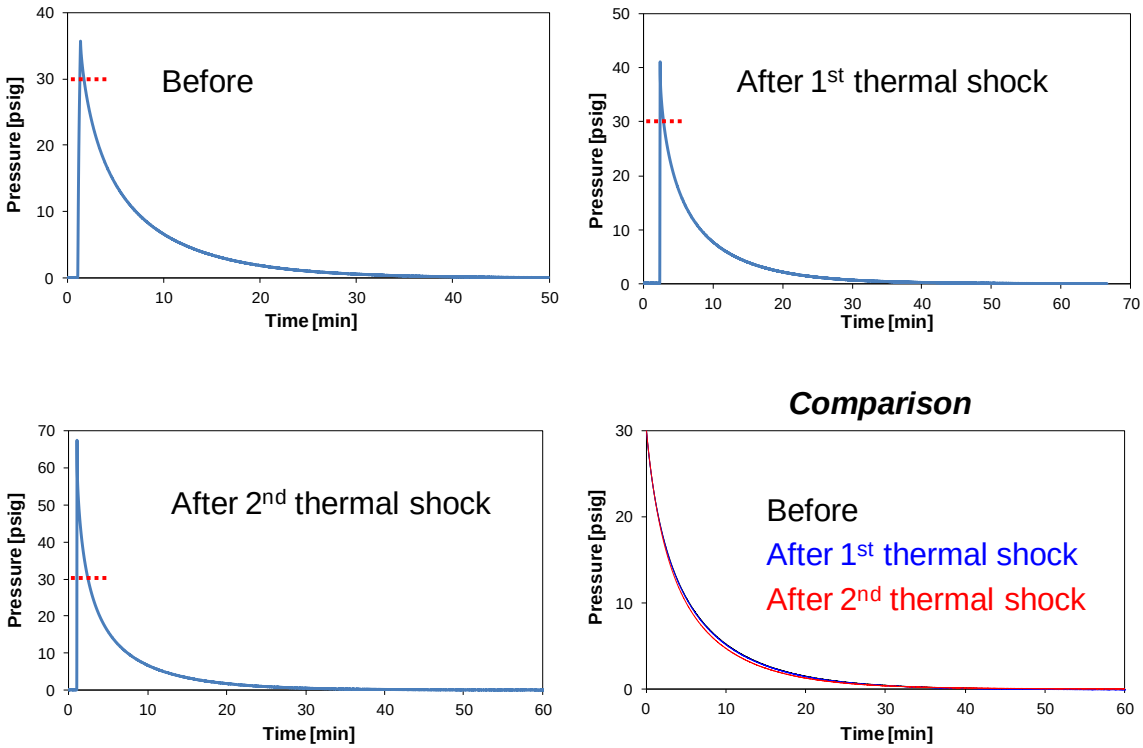

Figure 4.43 Pressure decay comparison

4.4.3 Thermal Shock with Liquid Nitrogen (the 3rd Thermal Shock)

Immediate liquid nitrogen flooding is important to make sure the borehole is cooled as fast as it can be. The efficient transport of LN_2 depends on the leakage in the Dewar (affecting pressure inside the Dewar) and the condition of the withdrawal device. Finally, the device is improved and we got liquid nitrogen released during the 3rd thermal shock. The 3rd thermal shock test is finished by the depletion of LN_2 in the Dewar tank (Figure 4.45)

Acoustic measurements were performed after the 3rd thermal shock to keep track of the indication of material deterioration due to the thermal shocks. The summary of the acoustic signal is compared later.

Temperature, pressure, and LN_2 consumption

The temperature data shows much more immediate temperature decrement compared with the two previous experiments. It also shows the Leidenfrost effect, which is another indication that LN_2 exists at the borehole. In Figure 4.45, the pressure plot shows a steady increase in the pressure until the end of test. While not knowing the cause of this increase, the temperature data also matches this trend by showing a steady increase of temperature.

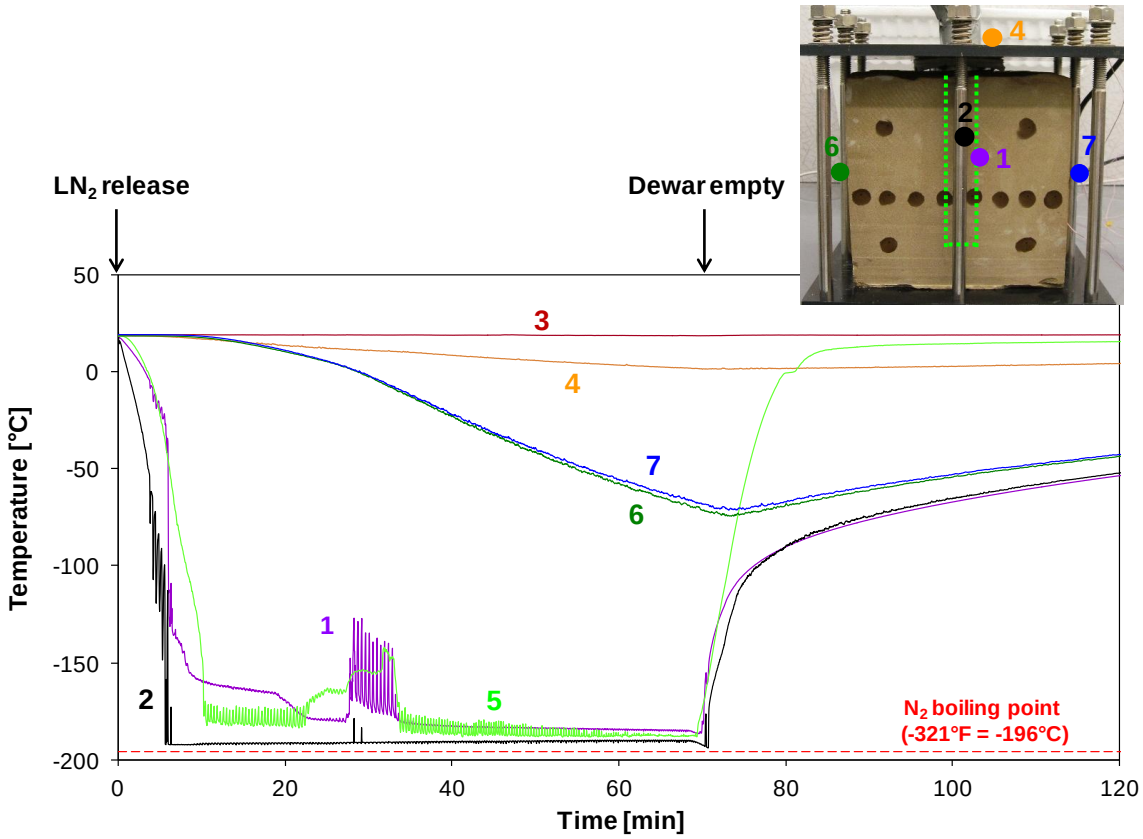

Figure 4.44 Temperature evolution during the 3rd thermal shock.

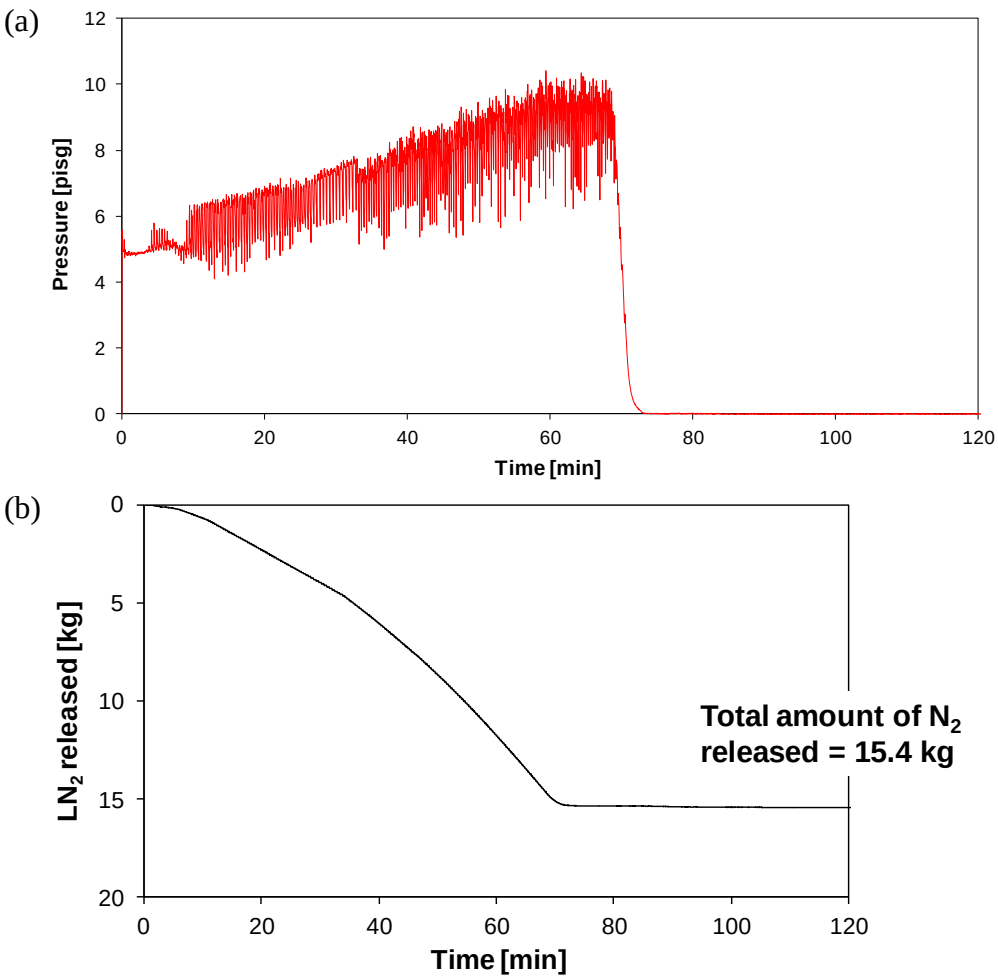

Figure 4.45 Pressure and LN2 consumption vs. time of the 4th thermal shock.

4.4.4 The 4th Thermal Shock (LN_2) & Pressurizations

At the 5th test, new devices are included to pressurize the borehole such as cryogenic-rated valves, a cryogenic pressure relief valve, an accumulator (sample cylinder), and a compressed nitrogen cylinder. The relief pressure of the pressue release valve is 275 psi, so the pressure inside the borehole is not to exceed that pressure.

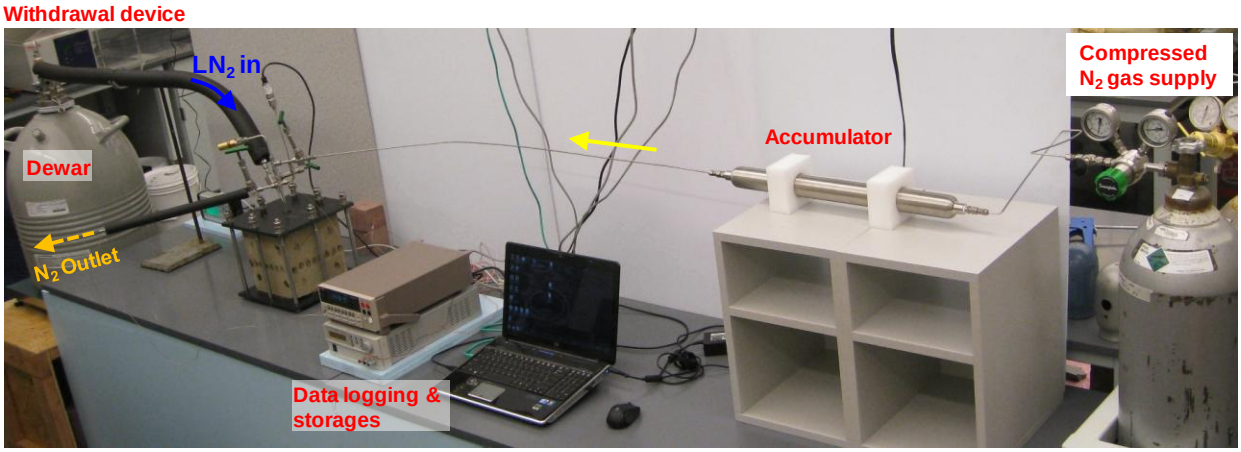

Figure 4.46 Experimental setup for thermal shock & borehole pressurization (protection shields not shown in this picture).

Pressure, temperature, and LN_2 consumption

Our pressure transducer's limit is 300 psi and our cryogenic relief valve's limit is 275 psi. So the borehole is not to be pressurized higher than that. Furthermore, unconfined specimens cannot sustain much pressure because geomaterials are generally weak at tensile stress.

After a thermal shock, two different borehole pressurizations are attempted. One is by natural vaporization of liquid nitrogen under a closed system. The other is pressurizing the borehole by supplying compressed nitrogen gas (Figure 4.48). It is observed that LN_2 vaporization causes the pressure to increase up to only 250 psi and thus the pressure relief valve was never operated (Figure 4.49). This means that nitrogen (most probably as a gas state) at the borehole was lost at a fairly high rate by permeation through the rock. This fast permeation rate is also hinted at the air permeability tests done on the previous tests.

The temperature inside the borehole increases rapidly as the borehole is pressurized (both forced pressurization and self-pressurization) (Figure 4.50). This is a negative aspect of borehole pressurization that pressurization increases temperature according to gas law. The temperature increases when the LN_2 supply discontinues. In addition to this, the temperature also increases from the pressurization.

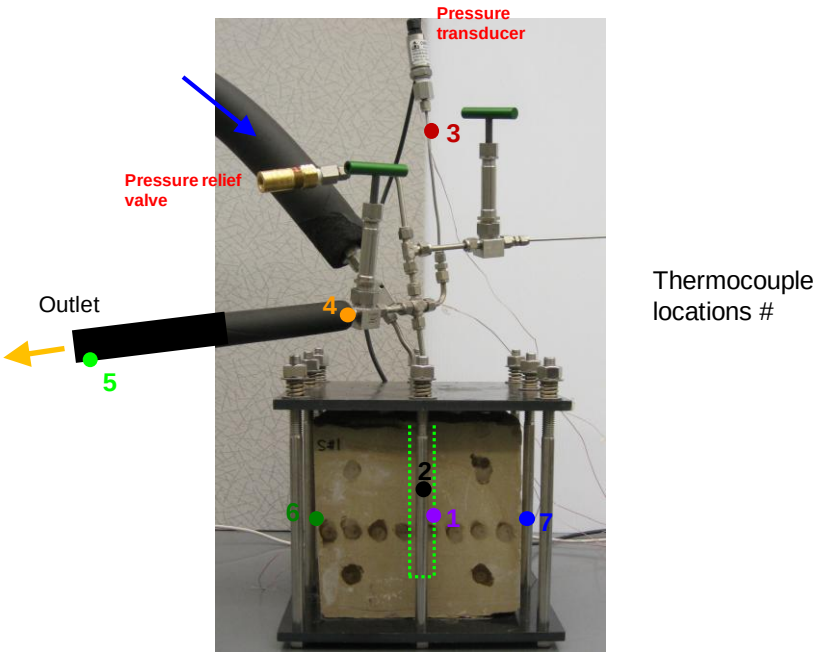

Figure 4.47 Experimental setup near the specimen and locations of thermocouple tips (the picture was taken before insulation is applied).

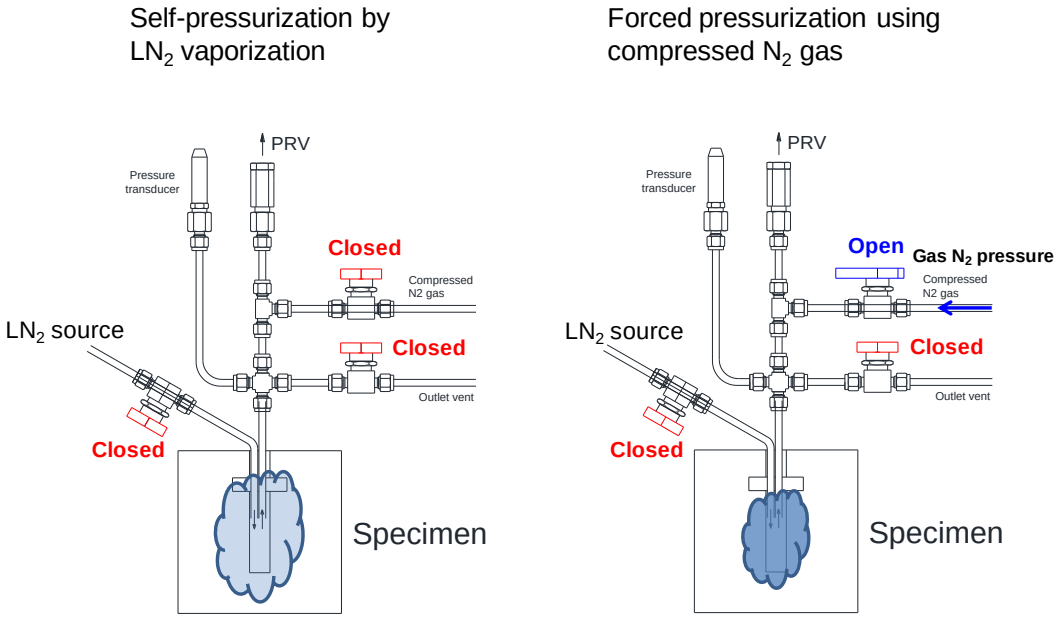

Figure 4.48 Two borehole pressurization schemes.

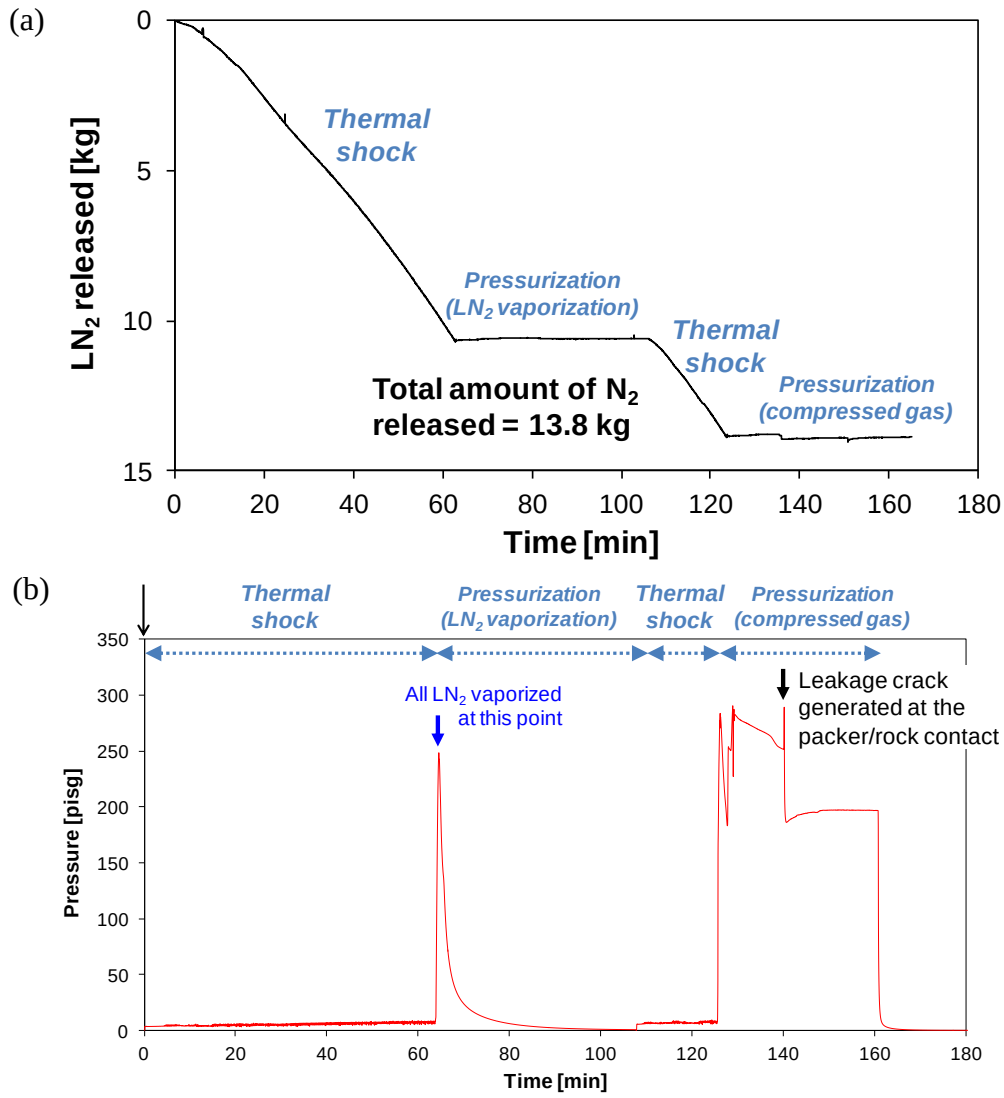

Figure 4.49 LN_2 consumption and borehole pressurization monitoring

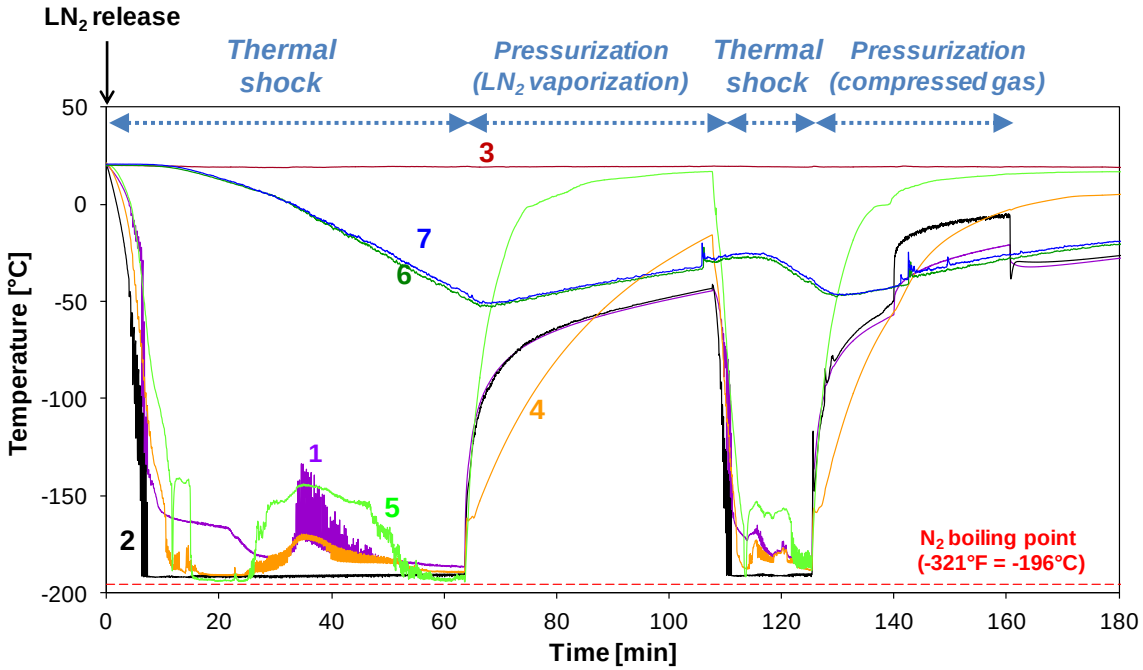

Figure 4.50 Temperature vs. time during the stimulation.

Bubble leakage test

During the experiment, we observed that a leak hole/crack was generated at the 2nd pressurization (force pressurization) at the packer/rock interface by sound as well as pressure data.

After the test, a bubble agent is used to detect the leak crack. In order to do this, the borehole is pressurized to about 50 psi by air. The liquid that was used for the bubble tests is specially designed for sensitive leak tests in pressurized equipment such as Dewar or gas tank. A leak hole that was created during the cryogenic experiment is located from the massive bubble generation (Figure 4.51a). Then the bubble agent is applied all over the top surface and Face 1 to observe permeation pattern at the block surfaces. We observed that there are several localized permeation spots (or "leaking holes") as shown in Figure 4.51 a and c.

The bubble leakage test shows that permeation through the stone is not homogeneous; there are invisible path (cracks, holes, or simply less tight zone) that allows more permeation of air/fluid. We are not sure the holes/cracks are particularly due to the cryogenic stimulations because we did not compared before and after.

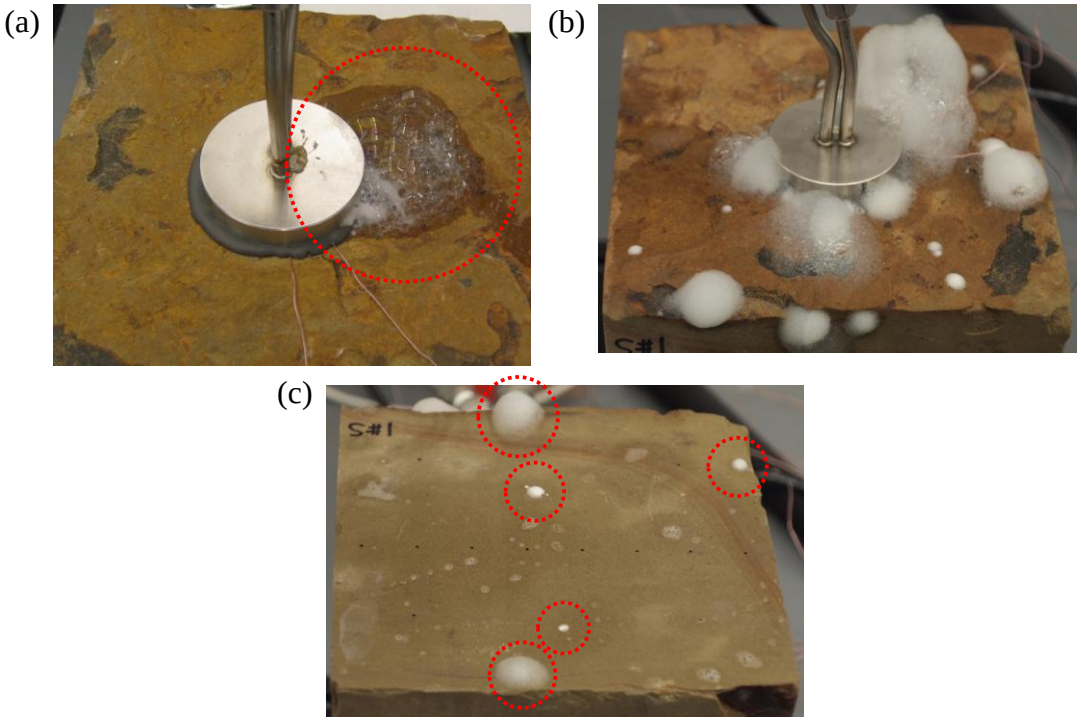

Figure 4.51 Leakage/permeation test by bubbles. (a) Leakge hole created at the packer/rock contact during the gas pressurization of the 4th test. (b) Localized air permeation observed at the top. (c) Local permeation at the side (Face 1).

Acoustic measurements

The P and S wave signatures before any thermal shock, after the 3rd thermal shock, and after the 4th thermal shock are compared. The velocities and amplitudes clearly changed, but in relatively small magnitude considering the number of stimulations performed. This shows that sandstone is relatively resistant to cryogenic stimulations compared to the cement concrete. The decreasing or increasing velocities as the sensor location moves along the surface seems to be due to both changing travel distance (due to uneven cut) as well as the internal rock properties. An analysis for the quantitative changes in velocity and frequency contents will be performed in the future.

(a)

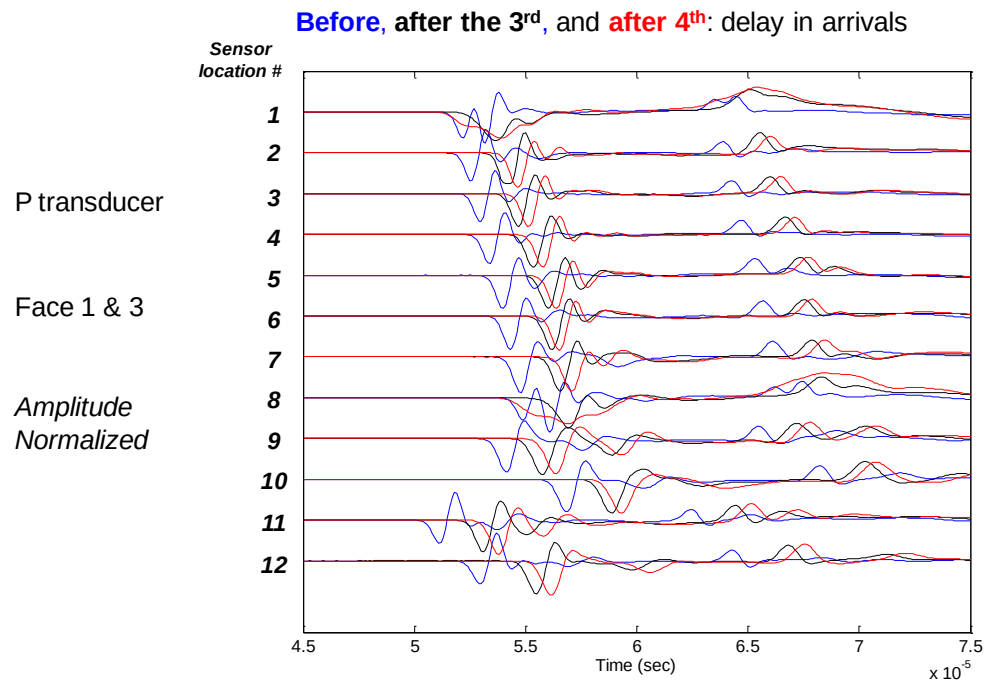

P transducer

Face 1 & 3

Amplitude Normalized

(b)

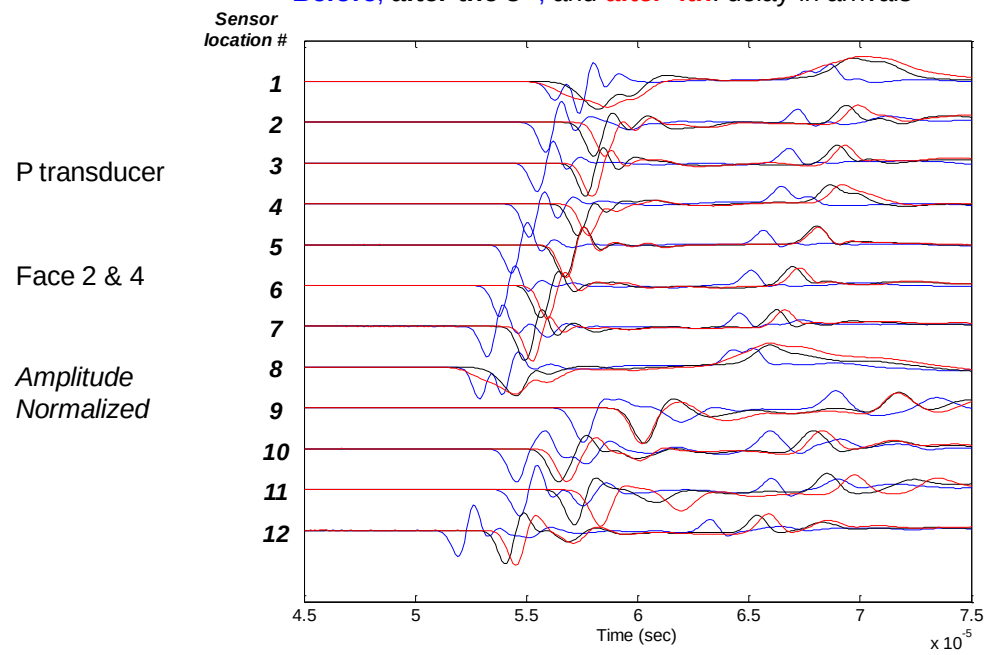

P transducer

Face 2 & 4

Amplitude Normalized

(c)

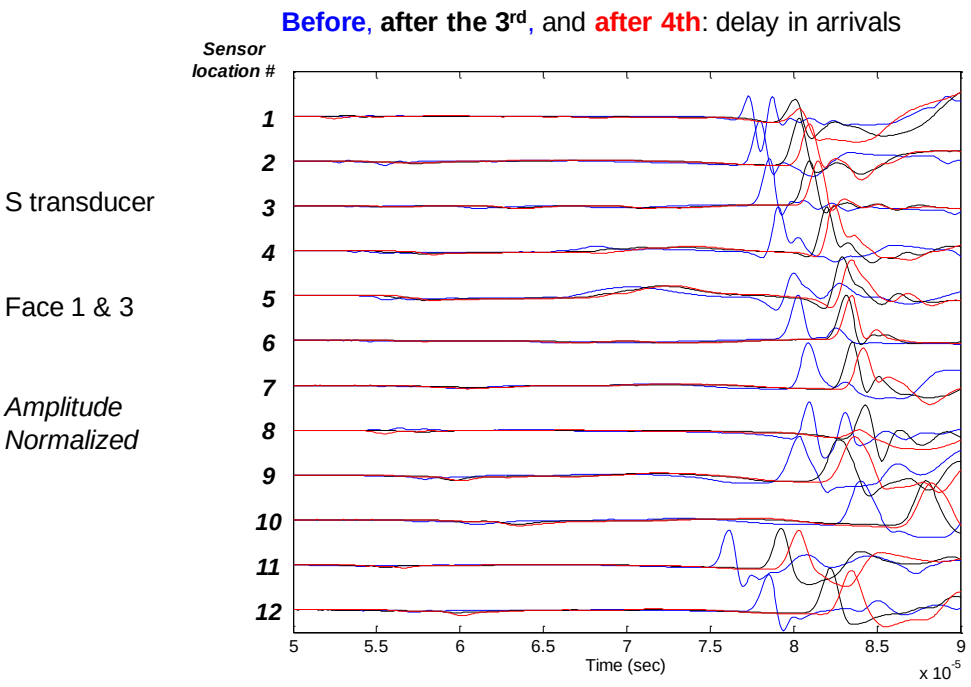

(d)

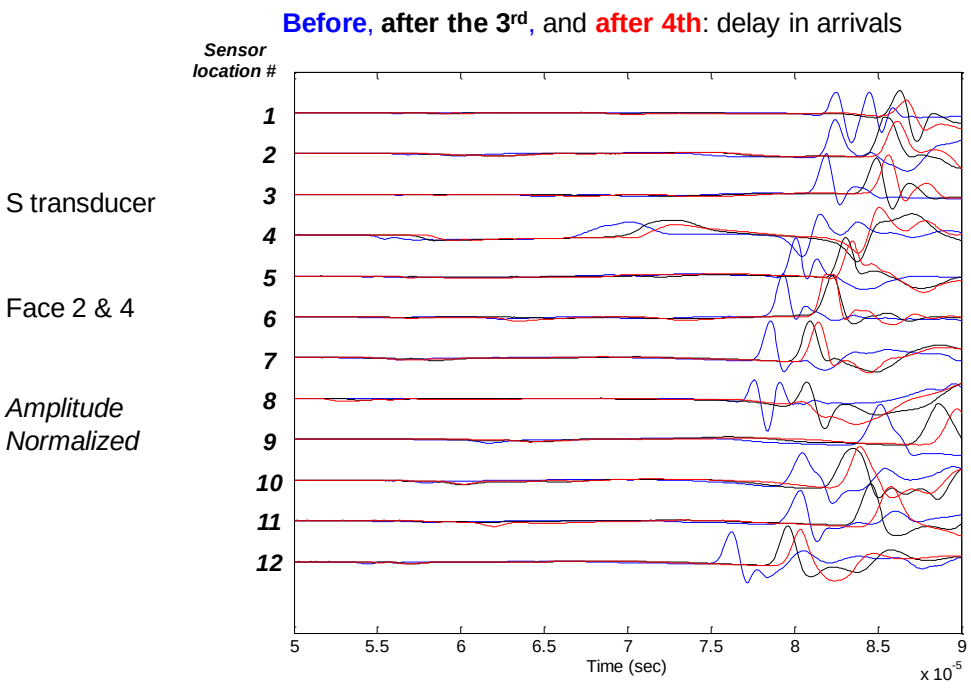

Figure 4.52 P and S wave arrivals before and after the cryogenic stimulation (compared with normalized amplitude).

(a)

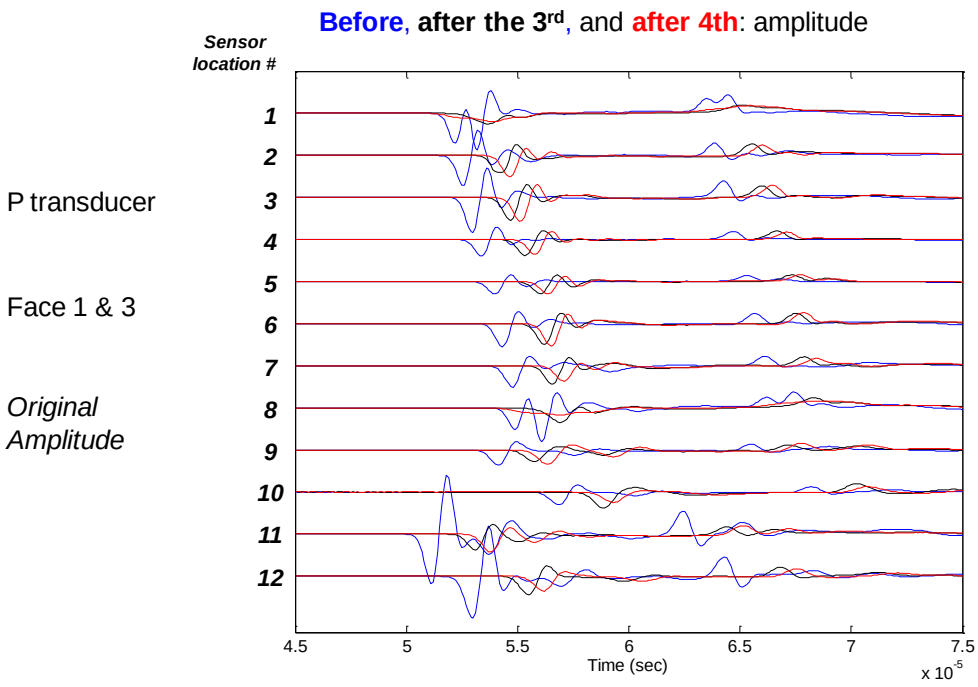

P transducer

Face 1 & 3

Original Amplitude

(b)

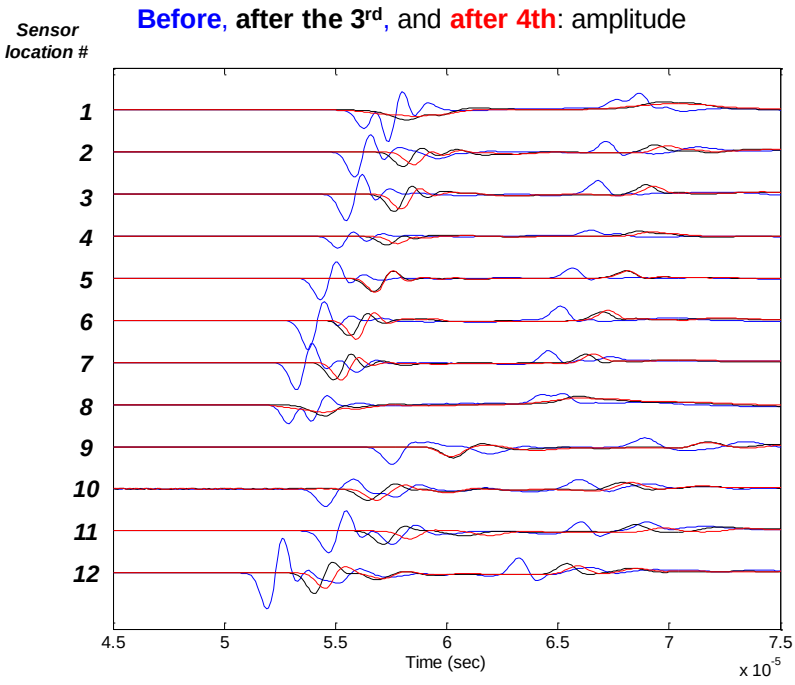

P transducer

Face 2 & 4

Original Amplitude

(c)

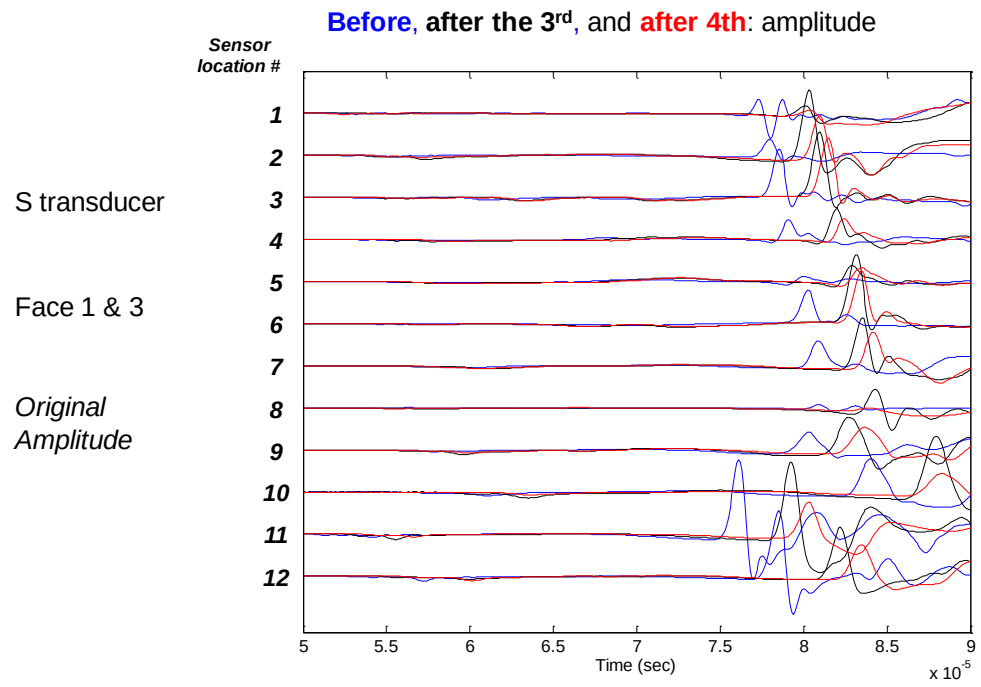

(d)

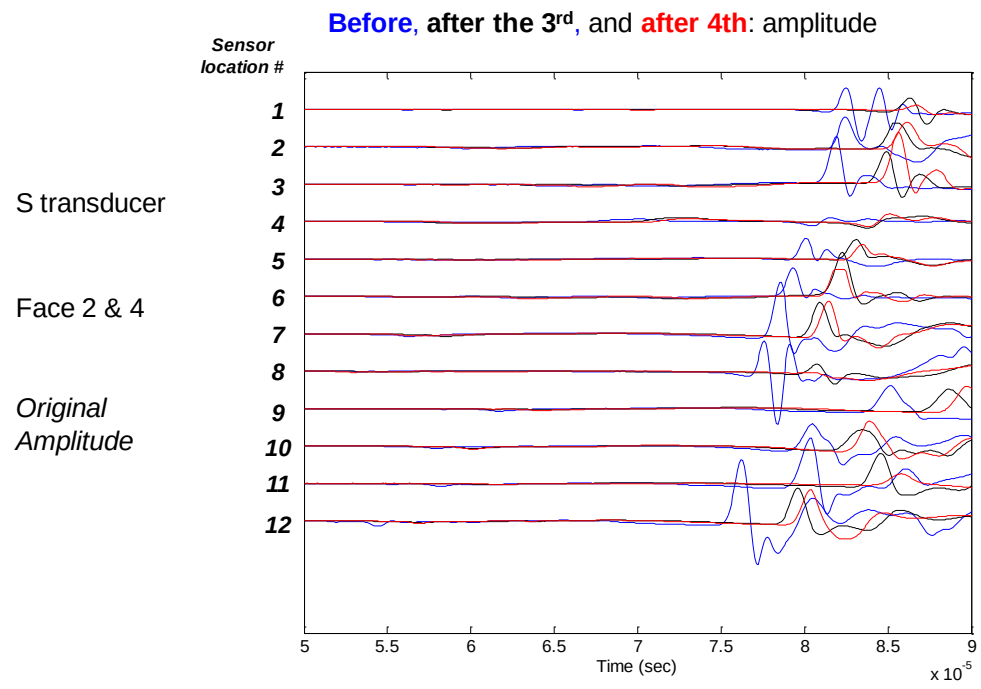

Figure 4.53 P and S wave amplitudes before and after the cryogenic stimulations.

(a)

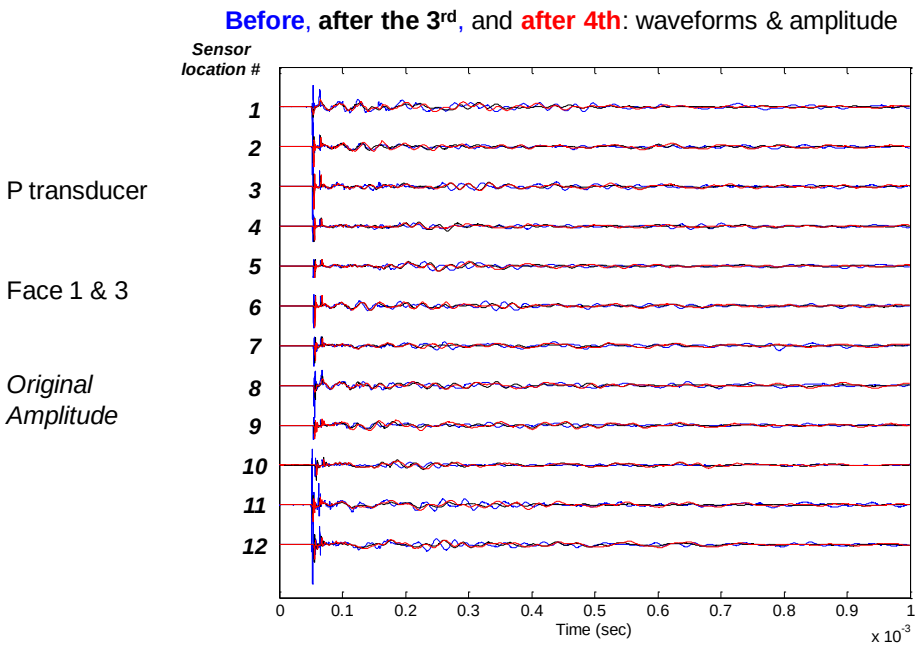
Before, after the 3rd, and after 4th: waveforms & amplitude
Sensor location #
1
2
3
4
5
6
7
8
9
10
11
12
P transducer
Face 1 & 3
Original Amplitude
0
0.1
0.2
0.3
0.4
0.5
0.6
0.7
0.8
0.9
1
Time (sec)
x 10-3

(b)

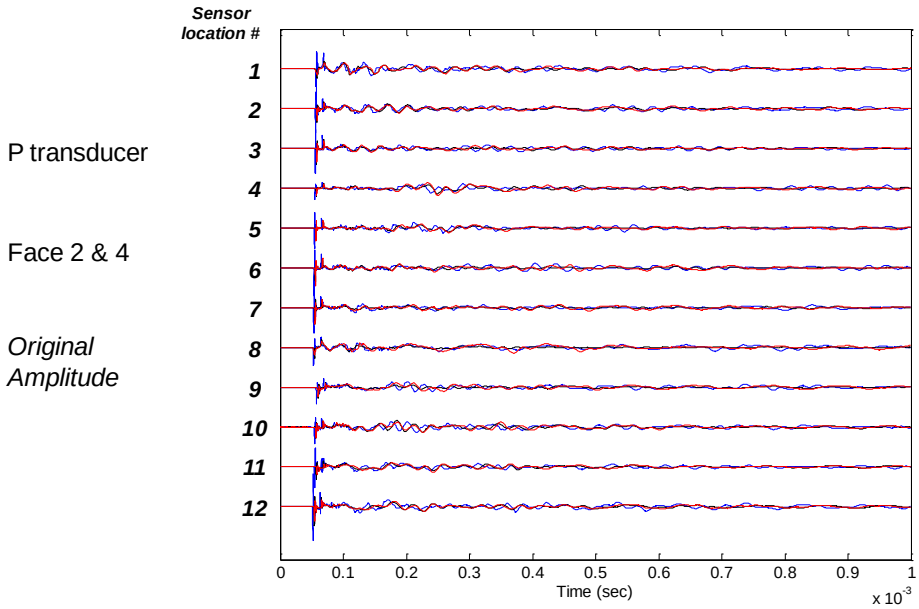
Before, after the 3rd, and after 4th: waveforms & amplitude
Sensor location #
1
2
3
4
5
6
7
8
9
10
11
12
P transducer
Face 2 & 4
Original Amplitude
0
0.1
0.2
0.3
0.4
0.5
0.6
0.7
0.8
0.9
1
Time (sec)
x 10-3

(c)

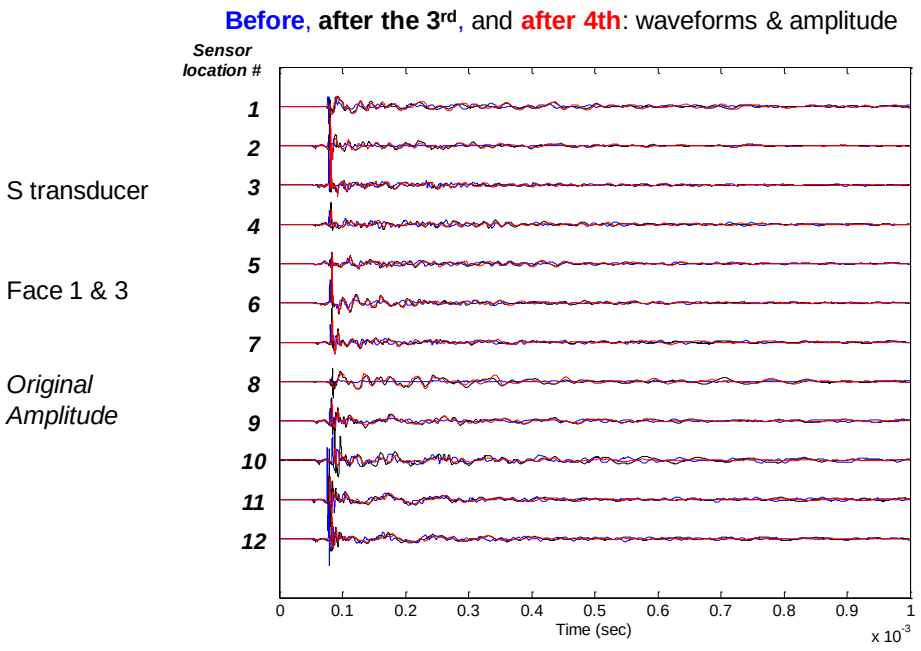

(d)

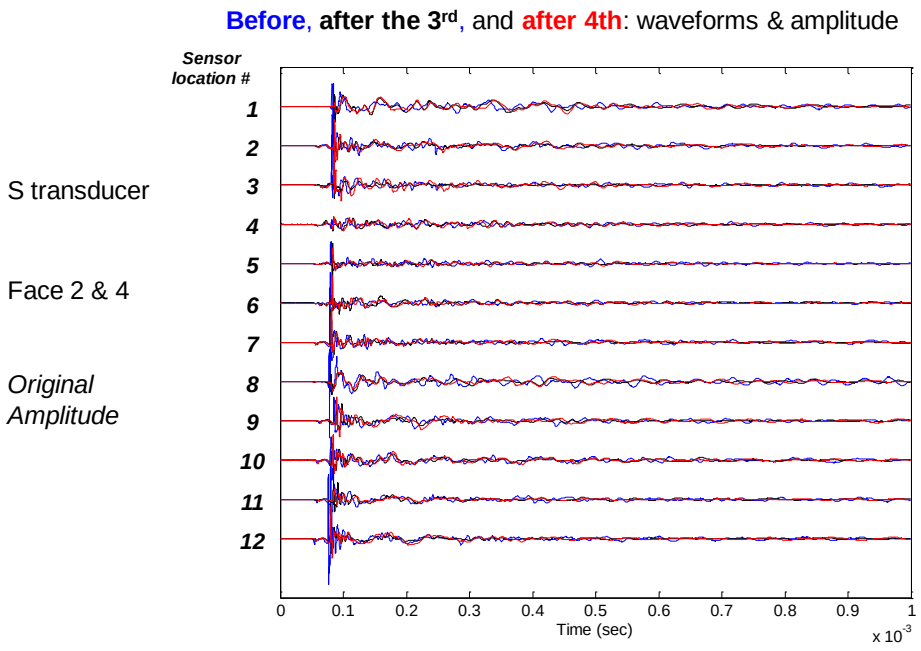

Figure 4.54 Global waveforms before and after the cryogenic stimulation.

4.5 Thermal Shock on Acrylic Cylinder Specimen

Experiments are performed to observe and study the development and morphology of cracks generated from cryogenic thermal shock at the borehole geometry. Acrylic specimens are chosen because they are transparent, and relatively brittle, which is one of the important characteristics of rocks.

4.5.1 Specimen 1

The dimensions of the acrylic specimen 1 are illustrated in Figure 4.55. The acrylic cylinder is 4" in diameter and 9.1" in height and the borehole is 7" deep and 0.5" in diameter. A 0.5" stainless steel tube is inserted and attached to the borehole wall to the depth of 2.5". LN_2 inlet tubing is inserted to 2.25" below the casing end.

Taking advantage of the specimen being transparent, we observed the flow characteristics inside the borehole. Upon the start of the experiment, nitrogen inside the borehole was flown initially as a gas state (for about 1~2 minutes), and then flown as a gas mixed with droplets of liquid, and finally flown in a more continuous phase of liquid with still a significant amount of gas phase intermixed.

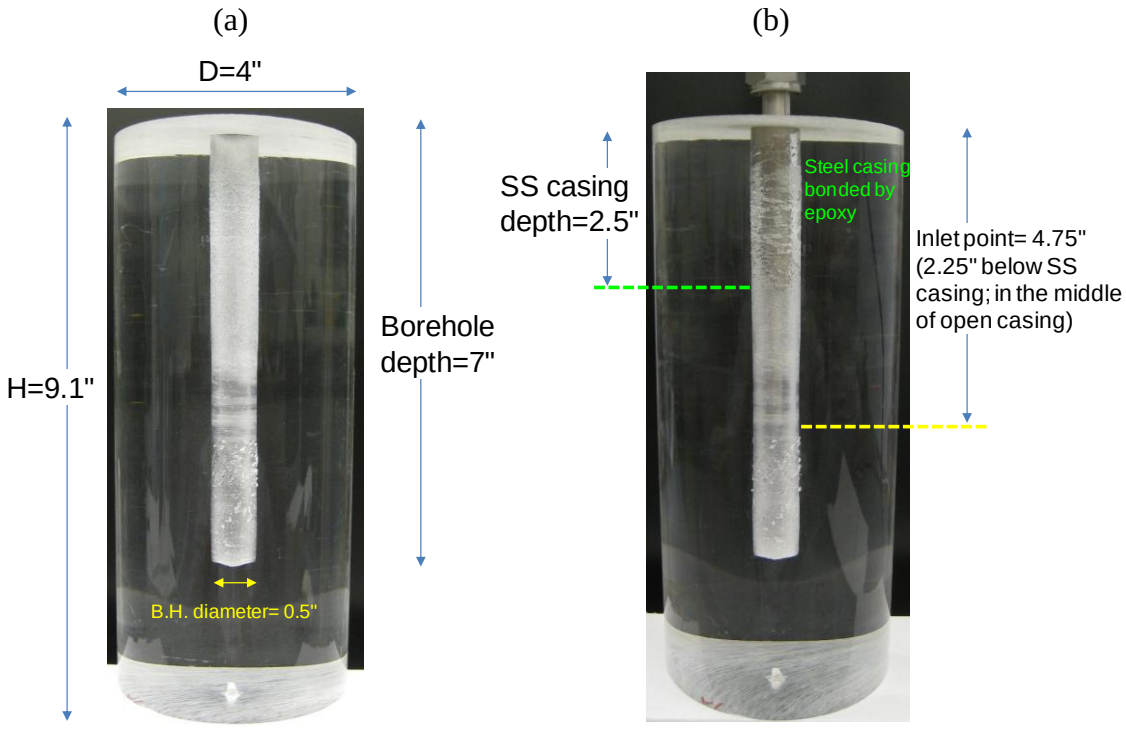

Figure 4.55 Acrylic specimen 1. (a) Dimension. (b) Description of stainless steel casing and inlet tube.

Temperature, pressure, and LN_2 consumption

Temperature decreased fairly rapidly compared to the previous experiments, potentially aided by efficient tube connections and insulations. Although a lot of LN_2 (20kg) was used, most of the fractures occurred at an early stage (within 20 minutes). The Dewar lever was opened fully during releasing LN_2 without any partial or full closure.

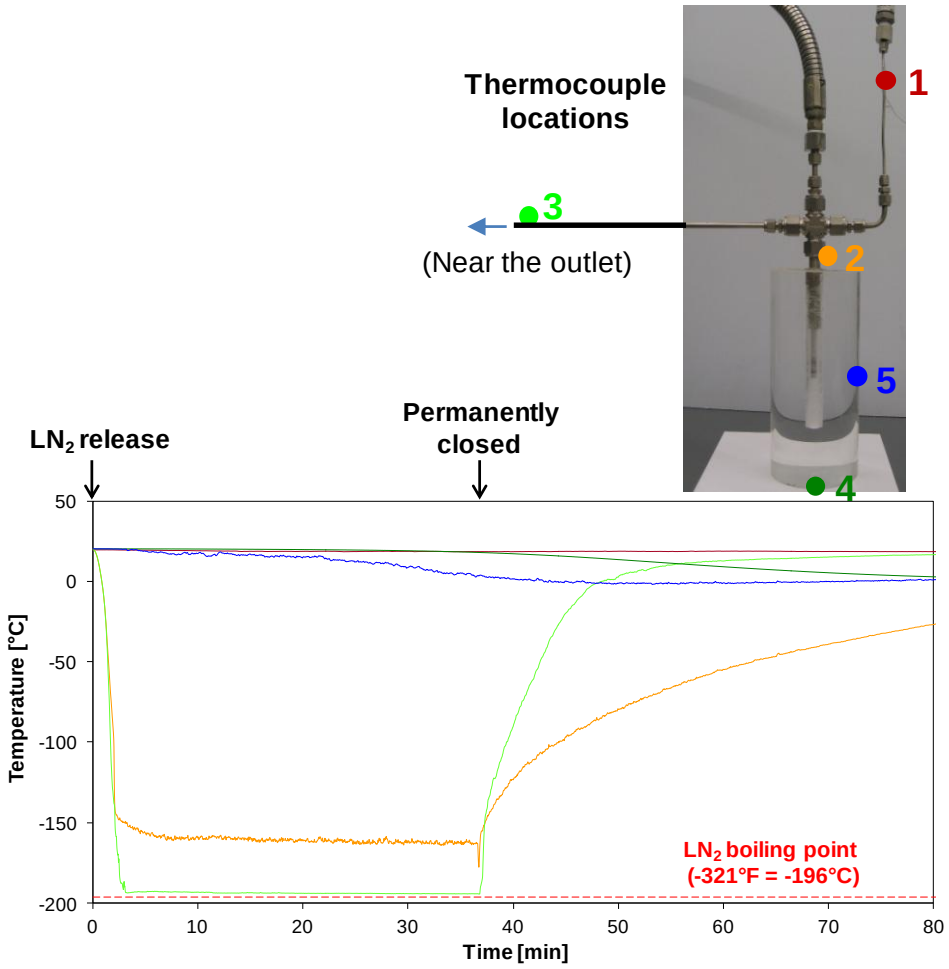

Figure 4.56 Locations of thermocouple tips and temperature evolution during the experiment.

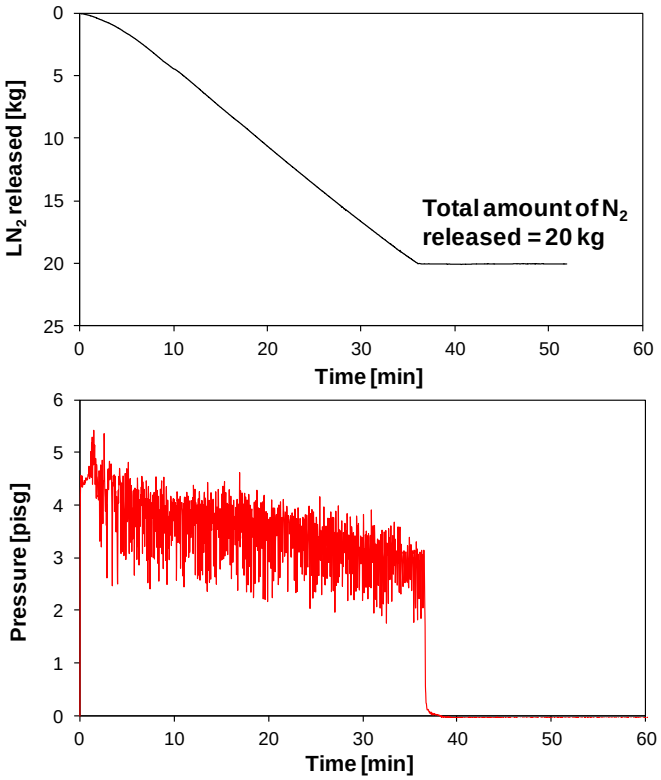

Figure 4.57 Borehole pressure and LN_2 released during the test.

Crack development

Images of specimens are captured in a time-lapse manner throughout the experiment (Figure 4.58). It is observed that fracture growth is not continuous, but rather jumpy and instantaneous. It emits clear audible sounds, when the fracture jumps to grow. The magnitude/amount of jump (or instantaneous growth) tends to decrease as the fracture grows larger. Most of the cracks occurred within 20 minutes.

The dominant pattern of crack morphology is a horizontal, planar, radial propagation. Each of such cracks is created, spaced by a certain length (exclusion distance). This can be explained by the fact that the specimen is cylindrical with a borehole height greater than the diameter, which makes the amount of thermal contraction greater in the longitudinal direction. An exclusion distance exists because a set of crack cannot be created closer than a certain length due to a limited amount of thermal contraction (Figure 4.59).

The circumferential thermal contraction does generate vertical cracks, though in less magnitude. The vertical tension cracks tend to initiate from or form between the existing

horizontal radial cracks, bridging between the radial cracks. It's energy-efficient to start from pre-existing defects (i.e., the horizontal radial crack) and propagate toward an existing defect (Figure 4.58~Figure 4.59). At the end of the experiment, the specimen shows complex fracture morphology created by interplay between longitudinal and circumferential thermal contraction in action (Figure 4.58).

Temperature distribution at the surface is also affected by the location of cracks. In fact, free movement of the liquid nitrogen was observed inside the cracks. This may help a crack to further propagate. Figure 4.60 show that some cracks approached the surface at a later stage of the experiment, and the temperature near the crack is readily affected by the proximity to the cracks.

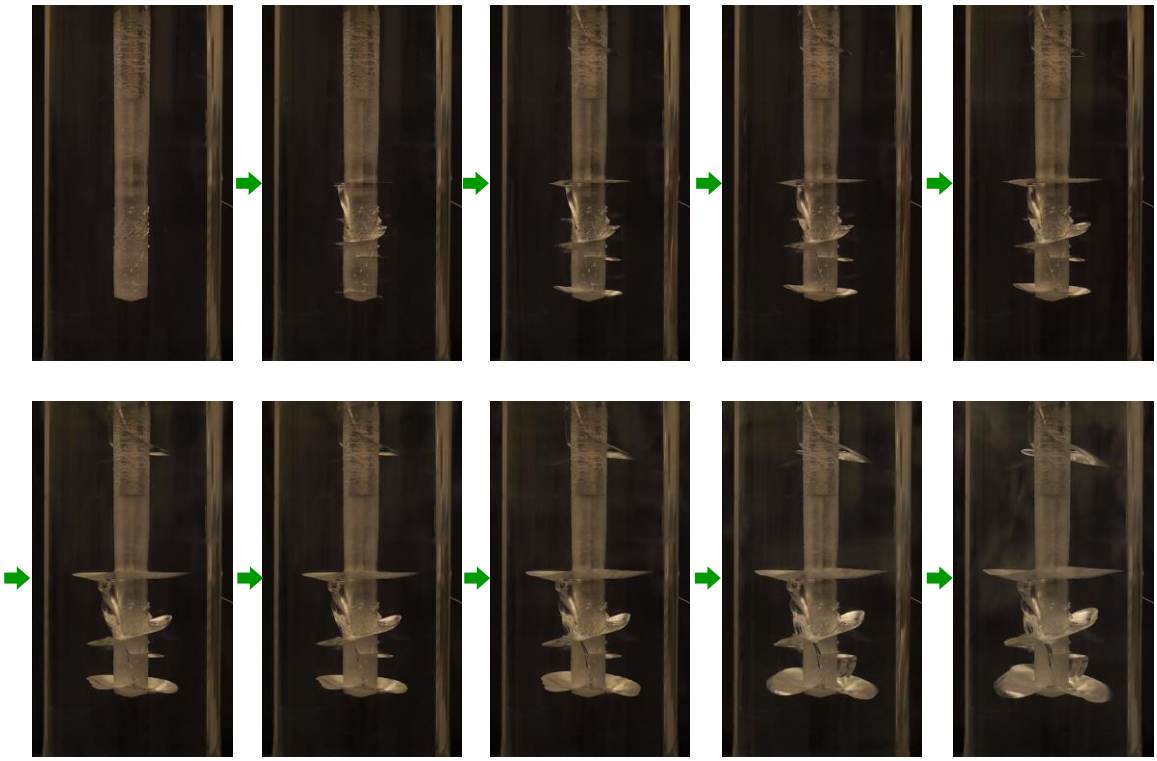

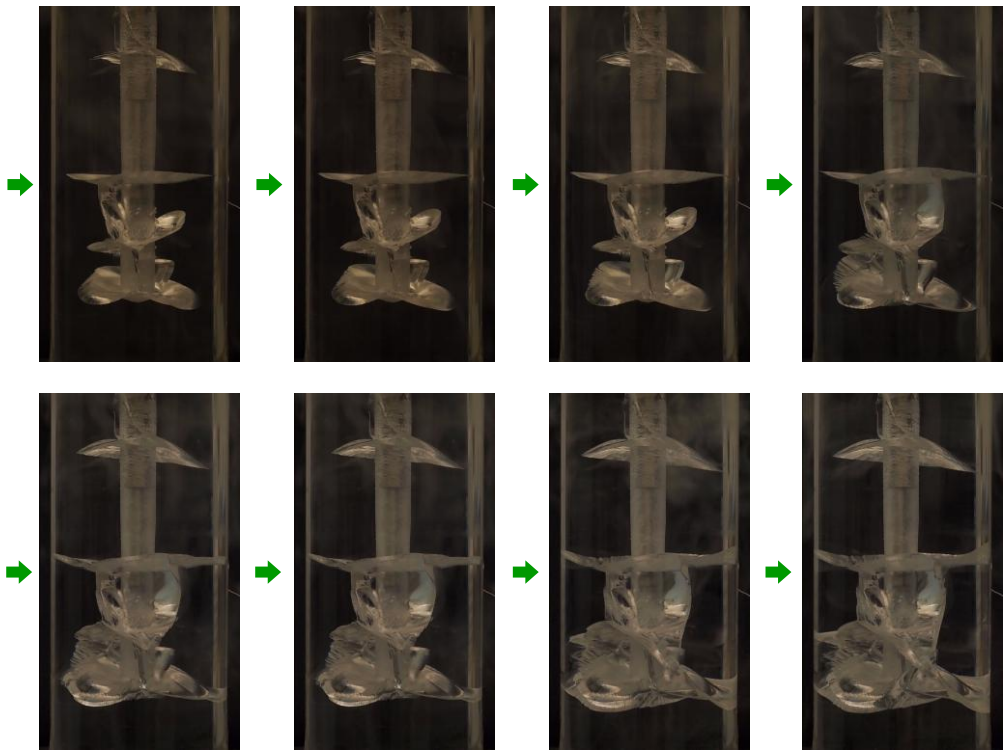

Figure 4.58 Crack development. The steps shown above do not represent all the crack growth steps.

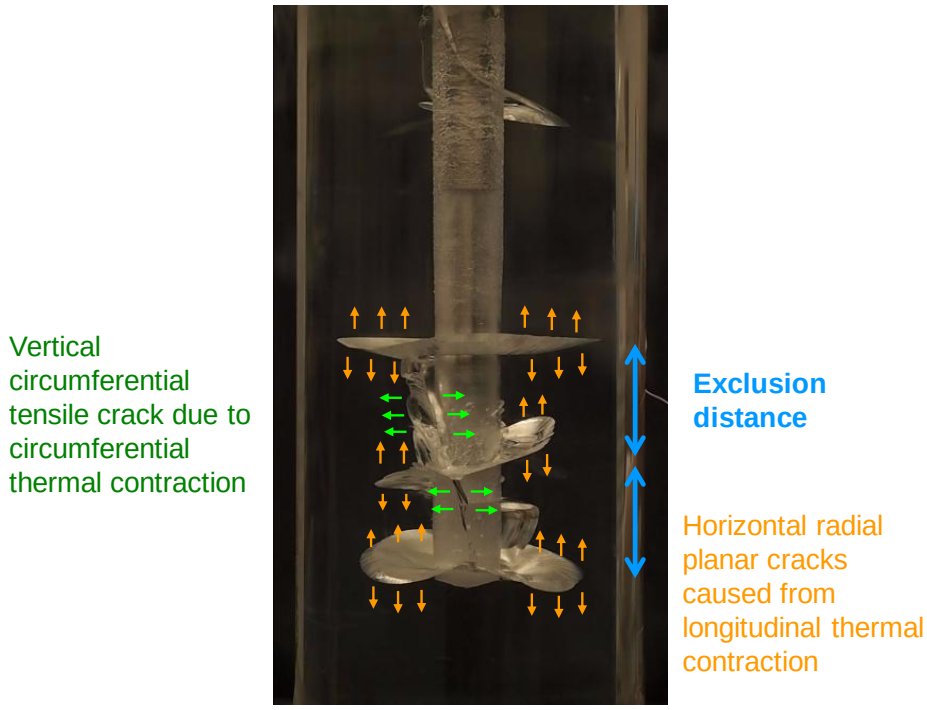

Figure 4.59 Crack morphology and driving thermal tensile stresses.

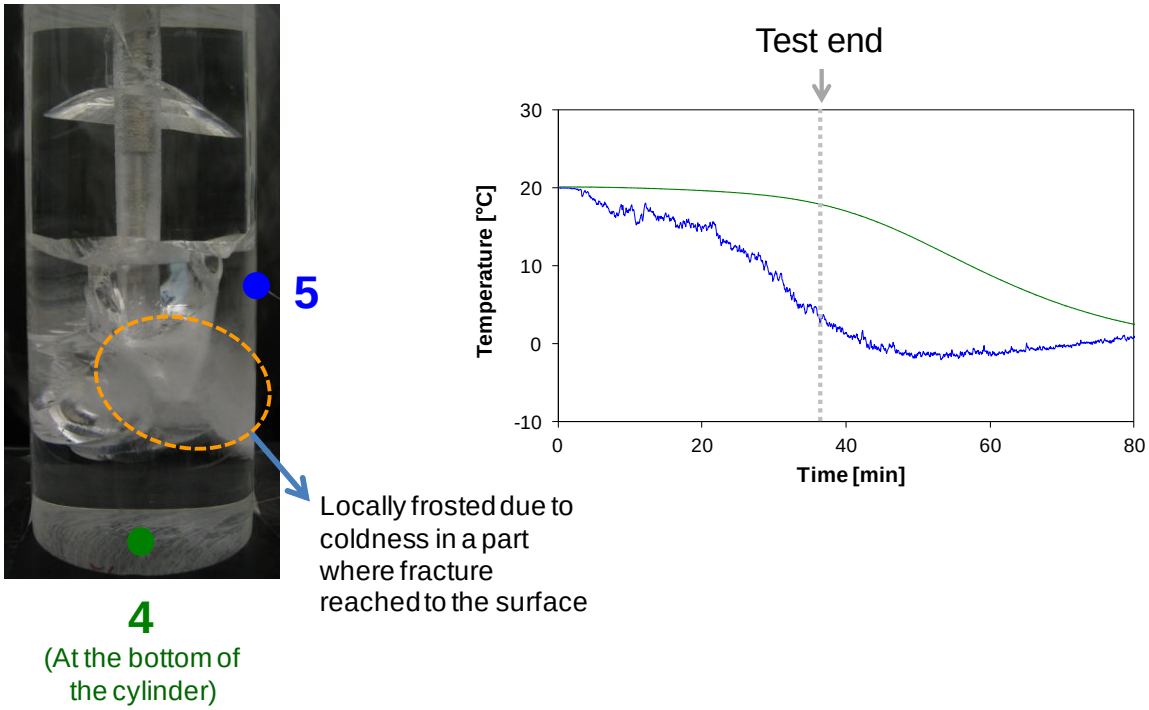

Figure 4.60 Effect of crack propagation on surface temperature

Effect of borehole condition

One major planar radial crack occurred at the steel casing area at an early stage. This should be affected by the presence of the steel casing, which has a high heat conductivity; the steel casing will have shorter period during which it is under Leidenfrost effect. However, further growth is limited because LN_2 cannot flow into the generated crack (Figure 4.61).

We have noticed that the distribution of cryogenic temperature inside the borehole is affected by the location of the injection point. Cracks are mainly generated near and right in front of the injection point, which suggest colder temperatures near the inlet (Figure 4.61).

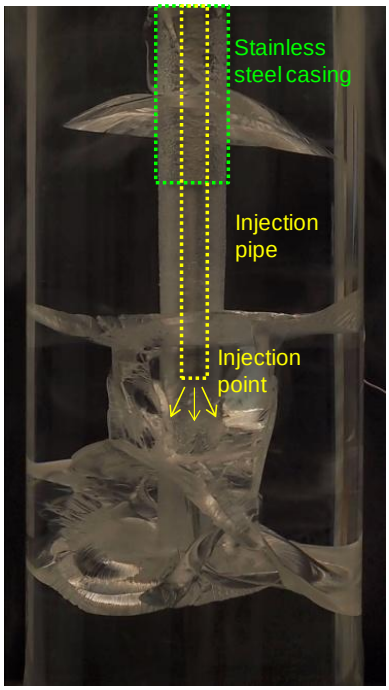

Figure 4.61 Effect of borehole condition.

4.5.1 Specimen 2

The sample dimensions are the same as those of the Specimen 1. Both the steel casing and the inlet point are 1.5" in depth. The injection point is purposely located higher than the previous test for the Specimen 1 to see the effect of the location of injection point. The experiment is finished by depletion of LN_2 tank. The duration of the experiment is 11 minutes and the amount of nitrogen consumption is 7.6kg.

Temperature

Temperatures at the side (TC #2, TC #4, and TC #5) dropped by non-negligible amount shortly after the end of the test (depletion of LN_2) as shown in Figure 4.63 and Figure 4.64. It is probably due to the pressure drop at the borehole. The temperature distribution at the surface is also dependent on the proximity to the cracks (Figure 4.64).

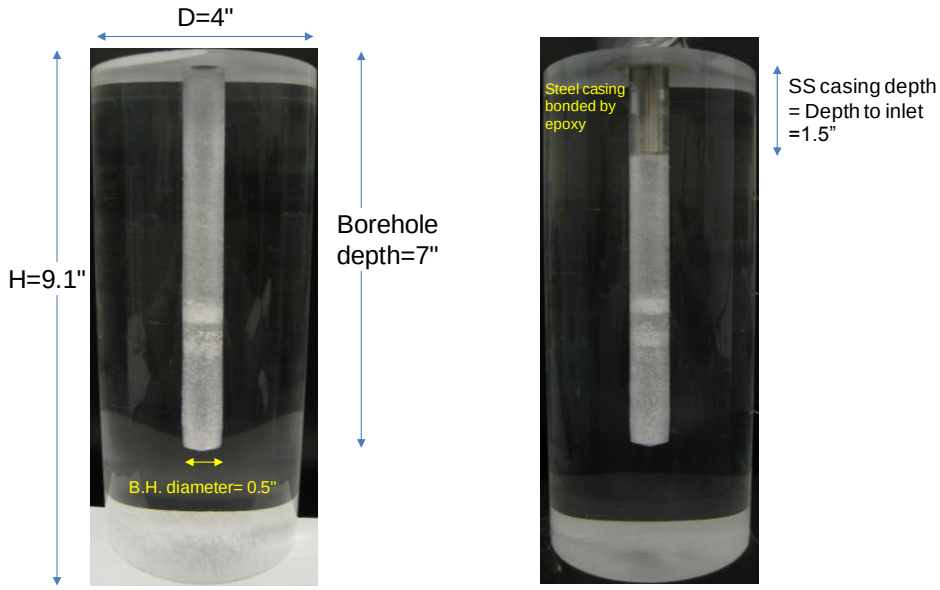

Figure 4.62 Acrylic specimen 2. (a) Dimension. (b) Description of stainless steel casing and inlet tube

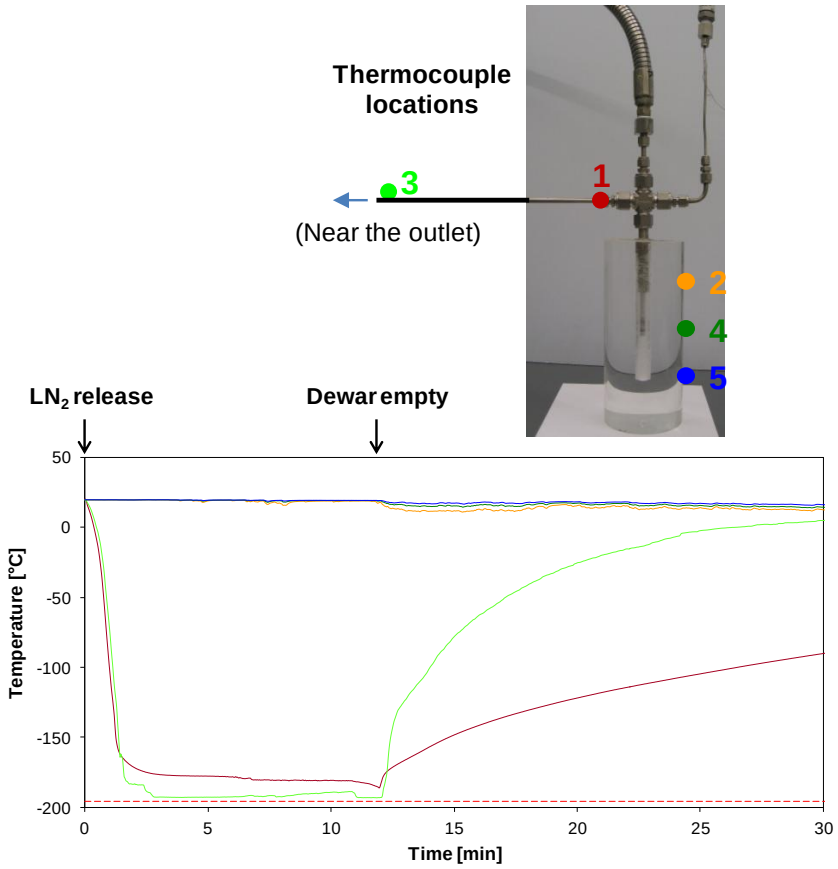

Figure 4.63 Temperature evolution during the testing.

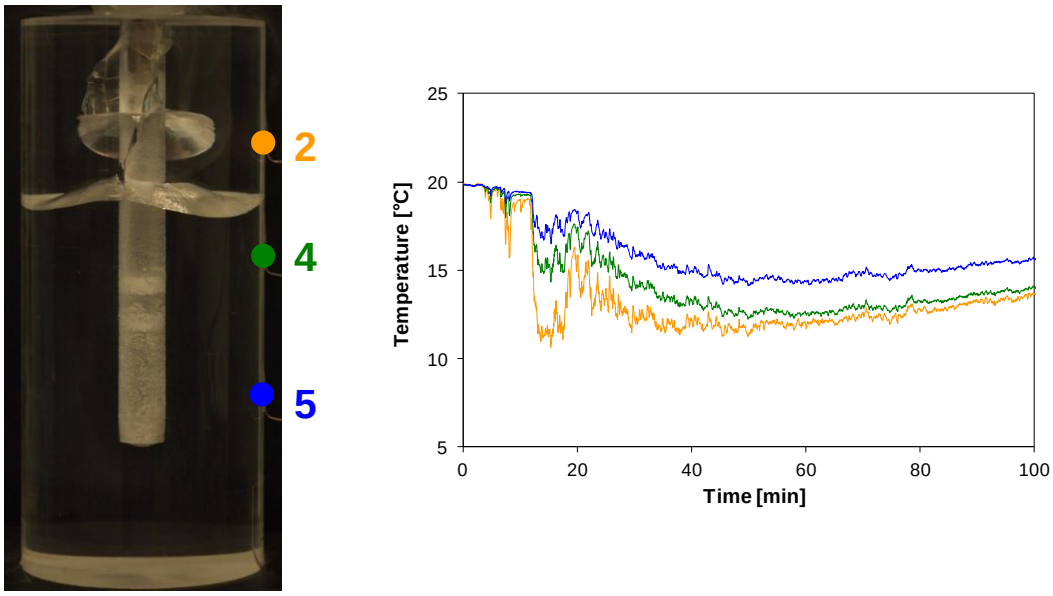

Figure 4.64 Effect of crack propagation on surface temperature.

Crack development

Two cracks are started as the horizontal radial pattern: one in the steel casing part and the other right in front of the inlet port (Figure 4.65). Later on, vertical cracks are created and bridges the radial cracks.

As observed and explained for the Acrylic 1 test, the cracks at the steel casing are aided by the efficient propagation of the cryogenic temperature from the casing, and the radial growth of the crack in the steel casing is limited by the lack of LN_2 supply to the generated crack (Figure 4.65 and Figure 4.66).

Similar to the Acrylic 1 test, the crack in the uncased part is located close to the inlet port. In this test; however, one big radial wing is created (compared to the three in the previous test), which means that there was not enough driving contraction to generate more cracks. The lack of thermal driving could be due to shorter stimulation time (thus smaller LN_2 applied) by the early depletion of the LN_2 tank.

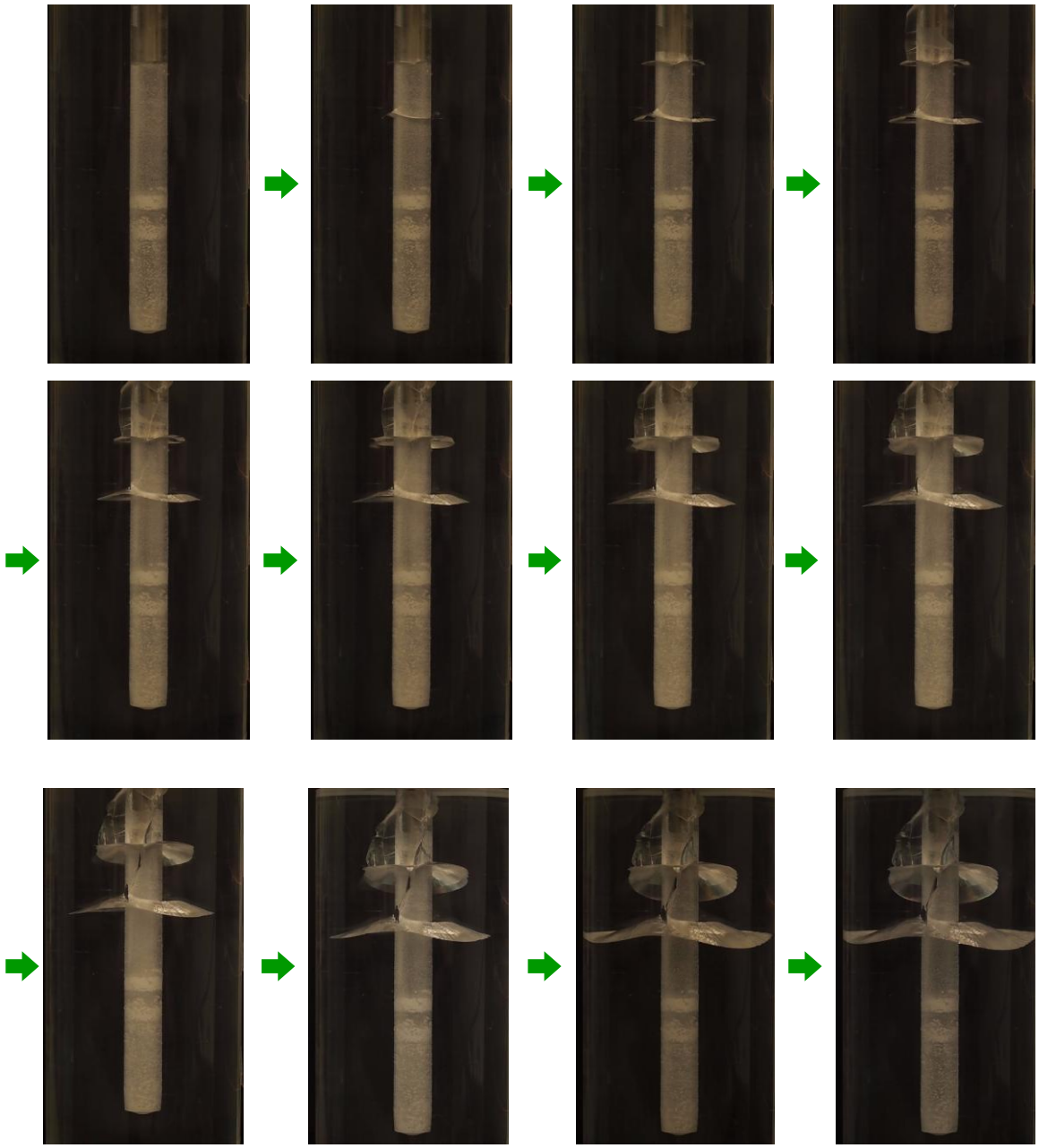

Figure 4.65 Crack development

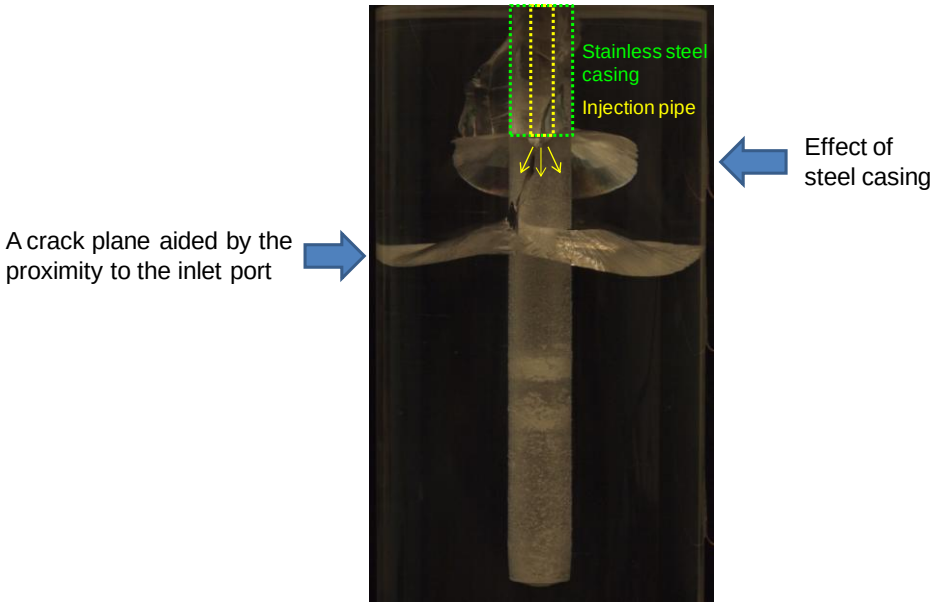

Figure 4.66 Effect of borehole condition.

5. Some Challenges and Issues

There are challenges to overcome such as reliable transportation to reservoirs, use of proppant with LN_2, and high heat flux and heat capacity of rocks. Here we discuss some identified issues from our experimental study.

5.1 Leidenfrost Effect – Slower Cooling Rate

The Leidenfrost effect happens anywhere when liquid is in near contact with a surface significantly hotter than the liquid's boiling point. It slows down heat transfer to the rock by making a vapor cushion, which has very low thermal conductivity, and thus may inhibit a sharp thermal gradient, which is a favorable condition for fracture propagation.

An experiment is performed to observe the Leidenfrost effect in the rock-LN_2 interface. Two Lyons sandstone blocks with roughly the same size dimensions (3"×3"×4") are prepared for the test. Two temperature sensors are attached to each block to monitor temperatures before and after submerging in LN_2. Another temperature sensor was subjected directly to the liquid nitrogen without touching any surfaces (Figure 5.1a). Before the submersion, the block 1 is heated to 120 °C, while the block 2 was in ambient temperature. Upon submersion, LN_2 violently boiled off at the interface of the blocks and liquid nitrogen. The rock block with the higher temperature takes longer time to reach the temperature of LN_2. In spite of the Leidenfrost effect, it is observed that the temperature dropped fairly rapidly to a certain temperature (120 °C in these tests). Although the temperatures recorded from the thermocouples at the block surface reached the temperature of liquid nitrogen in about 7 minutes, LN_2 continued to boil at the interfaces although the magnitude of boiling was decreasing gradually.

There may be potential methods to reduce the Leidenfrost phenomena. The use of slush nitrogen, which is a mixture of solid nitrogen and liquid nitrogen, is a relatively proven method to increase the cooling rate (Sansinena et al. 2012). Apparatuses for slush of nitrogen production has been patented (Kawamura et al. 2007, Machida et al. 2009). However, the managing and use of the slush nitrogen at a reservoir environment could be another challenge. Similarly, mixing proppants in liquid nitrogen as a solid suspension might help reduce the Leidenfrost effect, as we may need to use proppant anyway to keep fractures open. As pressure increases, the Leidenfrost effect occurs at a relatively higher temperature (Temple-Pediani 1969). Therefore, at higher pressure, the Leidenfrost effect will diminish earlier after LN_2 application. One disadvantage is that increasing pressure will increase temperature, which was observed during our experimental study. The Leidenfrost effect can be lessened by creating roughness at the surfaces; the Leidenfrost temperature increases as surface roughness increase (Bernardin and Mudawar 1999).

(a) (b)

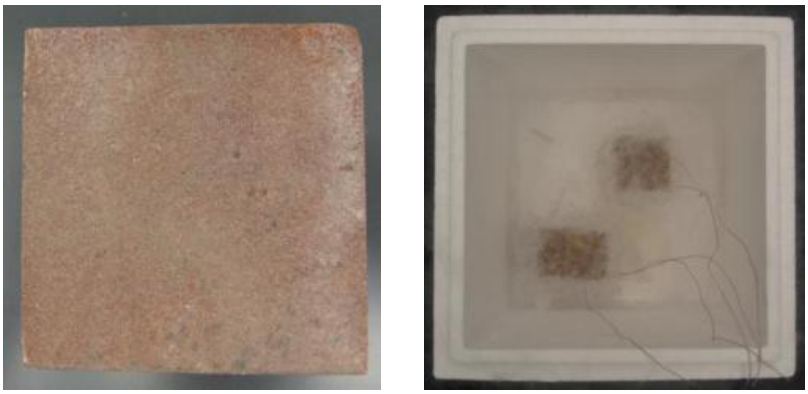

Figure 5.1 Lyons Sandstone block under LN_2.

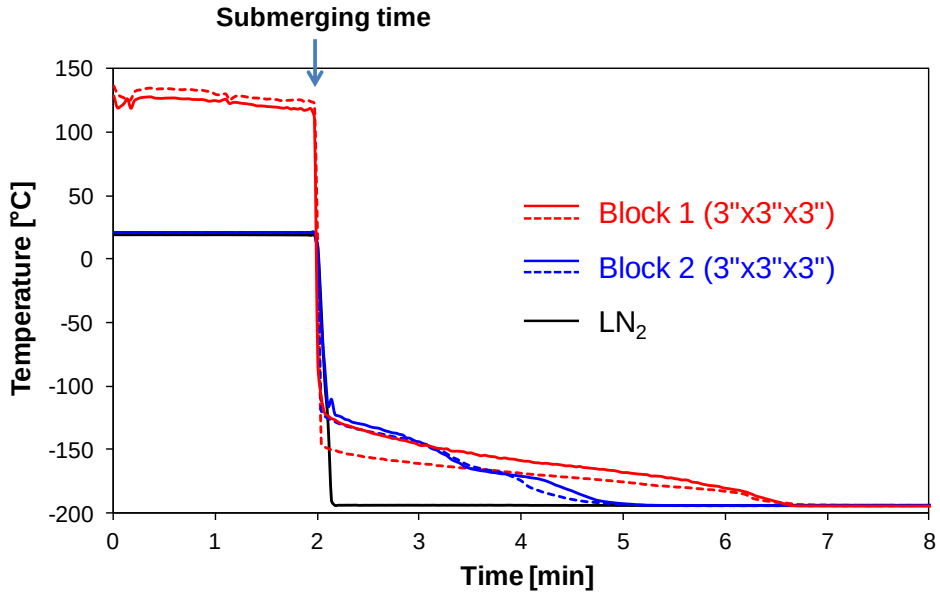

Figure 5.2 Rock submersion test with temperature measurements.

5.2 Presence of Water in Formation

When water becomes ice, the volume increase by 9%, which is much larger than any kind of thermally-induced expansion or shrinkage in geomaterials. To investigate potential consequences of this fact, the behavior of water-saturated rock under cryogenic temperature is investigated by conducting LN submersion test.

A fresh concrete sample with a water to cement ratio of 0.55, and sand to cement ratio of 2.5 was installed in the 8"×8"×8" mold and sealed in a plastic bag. After 24 hours, the seal and mold were removed and the concrete was cured under water for 8 weeks per ASTM C192, which will maximize hydration and render the concrete very strong. The 8"×8"×8" block was never removed from the water until testing. After 8 weeks, the specimen was subjected to full submersion to LN_2. The bottom surface was directly contacting the Styrofoam. The block had no visible cracks before the cryogenic stimulation.

(a) (b)

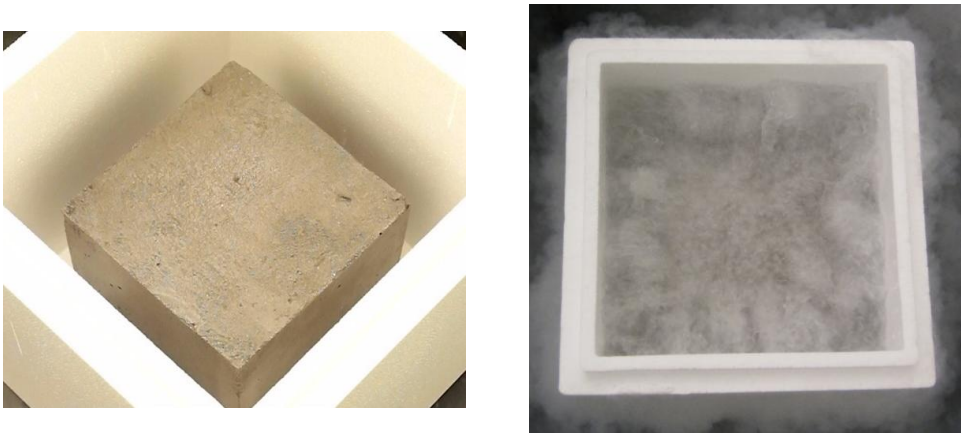

Figure 5.3 LN_2 submersion test (a) The water-saturated concrete cube placed inside the Styrofoam container (b) Violent LN_2 boiling at the interface between LN_2 and the block surfaces.

Cracks

All major cracks are created near edges after the cryogenic stimulation (Figure 5.4). This explains that ice matrix, which is heavily interconnected through pores, was trying to expand while mineral (cement and sand) matrix resisted it. The consequence is that the ice network was able to overcome concrete strength under tension near the edges, which is the weakest part to break off (Figure 5.5). If cracks were formed from rock contraction (without the effect of ice), more cracks should be located away from the edges. The

absence of crack lines near the bottom edges is probably because the bottom was directly touching the surface of the Styrofoam.

Simple calculation can be performed to help explain the competition between expansion of the ice matrix and contraction of the mineral (cement) network. Volumetric concrete thermal expansion coefficient γ (at 20°C) is 36×10^{-6}/K (linear coefficient $\alpha = 12\times10^{-6}$/K). Assuming α and γ is constant throughout the temperature range, the volume reduction due to cryogenic temperature would be:

$$\text{Volume reduction of minerals (\%)} = 200\text{K}\times36\times10^{-6}/\text{K}\times100\ (\%) = 0.72\%$$

H_2O has the property of becoming less dense when water is cooled to ice. Upon phase change to ice, the volume increase by 9%. Assuming the porosity of concrete is 20%, the overall resulting volume change becomes:

$$\text{Overall volume change (\%)} = (9\%)\times0.2 - (0.72\%)\times0.8 = 1.2\%\ \text{(expansion)}$$

There may be other complicating factors such as movement of water molecules within the block and outside during the freezing process. However, the movement of water to the outside will be negligible because the surface water will be immediately frozen upon LN_2 submersion.

Potential implication

Depending on the saturation level of water, the presence of water will weaken the driving force of cryogenically induced tensile fractures. In well-bore conditions at highly water-saturated porous formation, unlike the geometrical condition in the block test, volume expansion by freezing water will create circumferential compression. However, rocks in general are strong in compression. Therefore, a presence of water in the wellbore environment is likely to be unfavorable in cryogenic fracturing. Another important implication would be if water exists at borehole surfaces or near the borehole, upon LN_2 application, surface or near-surface water will be frozen and expand, which will inhibit nitrogen intrusion to the rock and thus prevent further cryogenic temperature propagation.

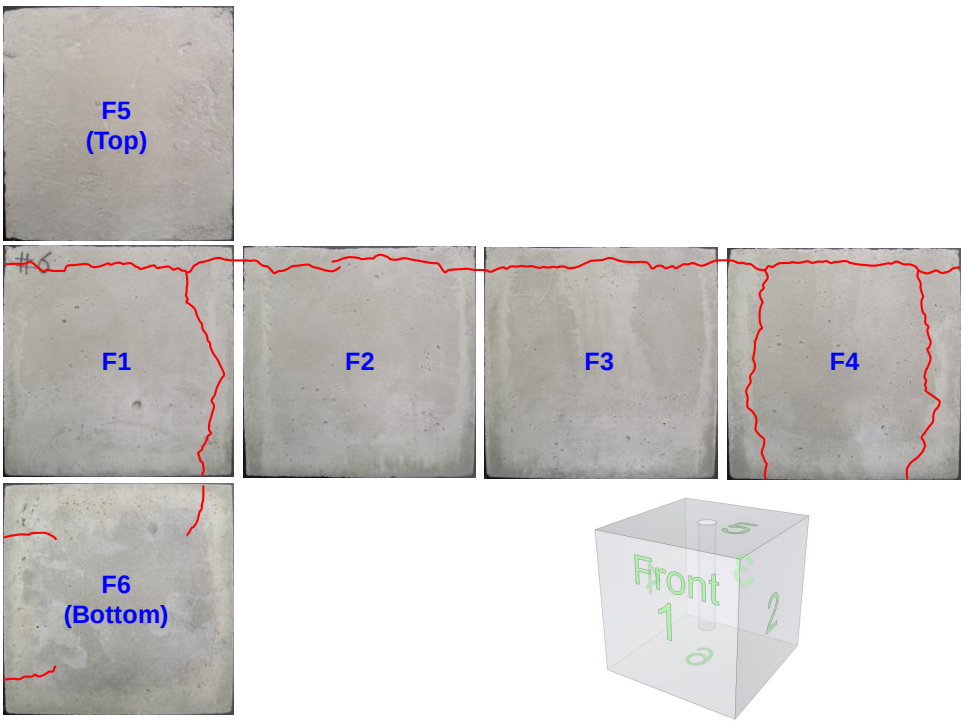

Figure 5.4 Specimen after thermal shock – red lines are superimposed along the cracks to improve visibility.

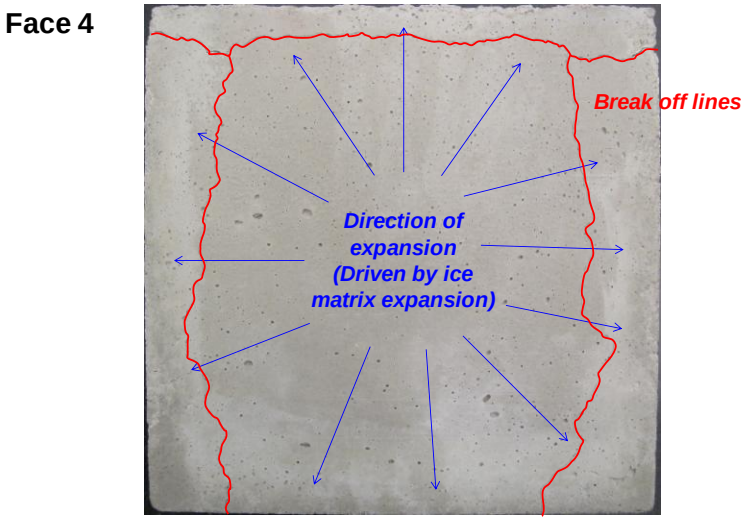

Figure 5.5 Cracks created by the expansion of ice matrix.

6. Conclusions and Future Work

We have designed our experimental apparatus for cryogenic stimulation, and made the laboratory procedure, which can equally be applied to the confined test with the triaxial loading equipment. Observations for crack assessment were made mainly by photographic inspection and acoustic signatures. The velocity and amplitude of acoustic signals are especially sensitive to rock properties, clearly differentiating changes in properties that are not visible to the naked eye. The bubble leakage tests confirm the existence of local permeation from the invisible cracks/defects. Macro-scale CT scanners were useful in identifying spatial distribution of major cracks. Having data for both temperature and pressure gave us reliability about the data as two data are always physically related.

The cryogenic stimulations conducted in our study were able to create cracks in the rock blocks and deteriorate rock properties. We observed that fractures were created along a line of the strongest thermal gradient in a concrete block half-submerged in LN_2. Increasing the number of cryogenic stimulations enhances the level of fracture by both creating new cracks as well as widening the existing cracks. On the other hand, by comparing the cryogenic fracturing results from weak concrete and sandstone specimens, it is found that the generation of fracture is dependent on material properties. For the weak concrete specimen used in our cryogenic fracturing study, more cracks were created near the surface than internally.

We have identified several issues relevant to the field conditions. To maximize the cooling rate, the means to alleviate the Leidenfrost effect needs to be sought. Immediate liquid nitrogen flooding is equally desired, which can be helped by efficient insulation and connection. Water saturated in the concrete can be a potentially unfavorable factor in cryogenic fracturing, especially at a wellbore geometry. Although target formations are typically waterless formation, the use of water may be minimized (e.g. from drilling and well completion and other operations that precede cryogenic stimulation). Borehole pressurization by LN_2 vaporization in the closed system does not generate significant pressure and destined to be temporal due to limited amount of LN_2 and permeation through rock pores. Therefore, for pressurization great enough to initiate fractures an external pressure source should be supplied.

Experiments with transparent specimens provide insight regarding the expected fracture propagation when sufficient thermal contraction/stress is achieved. It allows key observations in crack developments at the borehole geometry, such as exclusion distance, and crack morphologies driven by both longitudinal and circumferential thermal contraction.

In the near future, a true triaxial loading system will be installed in the department laboratory. The system will allow wide ranges of stress levels typically found at reservoir conditions, in which a borehole may be pressurized to the level relevant to fracture propagation during or following a thermal shock. The system also independently loads from three different axes. We will study characteristics of the crack propagation (e.g., magnitude and direction) as a function of stress levels and stress anisotropy under cryogenic stimulations. In addition, a heating instrument will be used to control the initial temperature of the specimen prior to cryogenic stimulation to simulate reservoir conditions.

We will investigate how material properties affect cryogenic fracturing behavior. As an example, the mechanical behavior of rocks, such as tensile strength and stiffness characteristics with strain level, under changing temperature needs to be considered as important characteristic of rock properties and for input for analytical study.

Full dimensional analysis will be performed considering all the relevant parameters. Reasonable guiding numbers will be obtained for dimensionless parameters by experimental, numerical, or analytical studies. An important aspect of dimensional analysis would be to guide scaling to the field condition and designing and preparing field-scale experiments.

If funding and time allows, acoustic emission experiments will allow some fundamental study related to the fracture process and source mechanism under cryogenic stimulation at reservoir condition.

REFERENCES

Fenghour, F., Wakeham, W.A., and Vesovic, V., *The Visocisty of Carbon Dioxide*, J. Phys. Chem. Ref. Data, Vol. 27, No. 1, 1998.

Grundmann, S.R., G.D. Rodvelt, G.A. Dials and R.E. Allen, *Cryogenic Nitrogen as a Hydraulic Fracturing Fluid in the Devonian Shale*, SPE 51067, 1998.

Gupta, D.V.S and D.M. Bobier, *The History and Success of Liquid CO_2 and CO_2/N_2 Fracturing System*, SPE 40016, 1998.

Kendrick, D.E., M.P. Puskar and S.T. Schlotterbeck, *Ultralightweight Proppants: A Field Study in the Big Sandy Field of Eastern Kentucky*, SPE 98006, 2005.

King, S.R., *Liquid CO2 for the Stimulation of Low-Permeability Reservoirs*, SPE 11616, 1983.

Mazza, R.L., *Liquid CO2 Improves Fracturing*. Hart's Oil and Gas World. February 1997, (22).

McDaniel, B.W., Grundmann, S.R., Kendrick, W.D., *Field Applications of Cryogenic Nitrogen as a Hydraulic Fracturing Fluid*, SPE 38623, 1997.

Rudenko, N.S., and Schubnikow, L.W., *The Viscosity of Liquid Nitrogen, Carbon Monoxide, Argon and Oxygen as a Function of Temperature*, NASA TT F-11, 86 8, 1968.

Bernardin, J. D., and Mudawar, I. (1999). "The Leidenfrost Point: Experimental Study and Assessment of Existing Models." *Journal of Heat Transfer*, 121(4), 894-903.

Kawamura, K., Machida, A., Ikeuchi, M., Hattori, K., Matsuo, K., and Yanagi, H. (2007). "Apparatus for producing slush nitrogen and method for producing the same." Google Patents.

Machida, A., Hattori, K., and Matsuo, K. (2009). "Method and apparatus for producing slush nitrogen." Google Patents.

Sansinena, M., Santos, M. V., Zaritzky, N., and Chirife, J. (2012). "Comparison of heat transfer in liquid and slush nitrogen by numerical simulation of cooling rates for French straws used for sperm cryopreservation." *Theriogenology*, 77(8), 1717-1721.

Temple-Pediani, R. W. (1969). "Fuel Drop Vaporization under Pressure on a Hot Surface." *Proceedings of the Institution of Mechanical Engineers*, 184(1), 677-696.